The Fragmentation of Massive Star-Forming Regions

Javier Adrián Rodón
Max-Planck-Institut für Astronomie

Heidelberg 2009

Dissertation in Astronomy
submitted to the
Combined Faculties of the Natural Sciences and Mathematics
of the Ruperto-Carola-University of Heidelberg, Germany,
for the degree of
Doctor of Natural Sciences

Put forward by
Lic. *Javier Adrián Rodón*
born in Córdoba, Argentina

Oral examination: 9.11.9

The Fragmentation of Massive Star-Forming Regions

Referees: **Prof. Dr. Thomas Henning**
Priv. Doz. Henrik Beuther

A mi abuela Corina Jaya,
aquí están los frutos de la distancia.

To my grandmother Corina Jaya,
distance has paid off.

Abstract

Since its discovery by E. Salpeter in 1955, the high-mass end of the Initial Mass Function (IMF) has been continuously tested, and its slope has not changed from the value -2.35 originally calculated by Salpeter, the "Salpeter value". Furthermore, it is found that this value is universal. It not only describes the mass distribution of stellar masses in the Milky Way but also in other galaxies.

Stars form individually or in systems within molecular clouds, from local condensations of sizes on the order of ~ 0.01 pc, the so-called "dense cores". In the case of low-mass star-forming regions, it is found that the Core Mass Function (CMF) resembles the Salpeter IMF. However, in the case of massive star-forming (MSF) regions, the answer is not that clear.

The first CMF for a MSF region was derived in 2004 by H. Beuther and P. Schilke for the MSF IRAS 19410+2336. They found that this CMF also resembled the Salpeter IMF. Since then, a few more CMFs for MSF regions have been derived, always with exponents comparable to Salpeter. This suggested that the CMF and the IMF are related in a one-to-one or nearly one-to-one relationship, and that the fragmentation processes within a molecular cloud would set the shape of the IMF at an early evolutionary stage

Attempting to test that scenario, in this thesis I present and analyse high angular resolution interferometric observations of several MSF regions at millimeter wavelengths, describing their protostellar content and deriving their CMF whenever is possible. We confirm the result of Beuther & Schilke (2004) and obtain a CMF with a power-law slope similar to the Salpeter IMF, however for other MSF regions we obtain a CMF with a power-law slope flatter than Salpeter. This difference suggests that the IMF might not be set at the moment of the fragmentation of the cloud, but insted would be a result of the evolution of the cloud, starting with a flatter mass distribution that becomes steeper at laterevolutionary stages. This result is not conclusive yet, and we suggest a series of observations that would be needed to fully test it.

Zusammenfassung

Seit seiner Entdeckung durch Edwin Salpeter im Jahre 1955 wurde das massereiche Ende der ursprünglichen Massenfunktion (IMF) immer wieder untersucht, und die Steigung hat sich vom ursprünglich bestimmten Wert Salpeters von -2.35, dem "Salpeter-Wert", nicht verändert. Vielmehr hat sich herausgestellt, daßdieser Wert universell ist, er beschreibt nicht nur die Massenverteilung stellarer Massen in der Milchstrasse sondern auch die in anderen Galaxien.

Sterne entstehen in Molekülwolken, einzeln oder in Systemen, aus lokalen Kondensationen in einer Grössenordnung von ~ 0.1 pc, den sogenannten "dense cores" ("dichten Kernen"). Im Falle von Regionen massearmer Sternentstehung wurde gefunden, daß die Kernmassenfunktion (CMF) der Salpeter IMF gleicht. Allerdings ist für Regionen massereicher Sternentstehung (MSF) diese Frage noch nicht geklärt.

Die erste CMF für eine MSF Region wurde 2004 von H. Beuther und P. Schilke abgeleitet für die MSF IRAS 19410+2336. Auch die von ihnen gefundene CMF gleicht der Salpeter IMF. Seitdem wurden einige wenige CMF für MSF Regionen bestimmt, alle mit einem Exponenten ähnlich dem von Salpeter bestimmten. Dies deutet auf eine eins-zu-eins-, oder beinahe eins-zu-eins-Beziehung der CMF und der IMF und daß der Fragmentierungsprozess innerhalb einer Molekülwolke die stellare IMF schon zu einer sehr frühen Entwicklungsphase festlegt.

Um dieses Szenario zu testen, präsentiere und analysiere Ich in dieser Doktorarbeit interferometrische Beobachtungen mit hoher räumlicher Auflösung im Millimeterbereich von mehreren MSF Regionen. Dabei beschreibe Ich deren protostellaren Inhalt und leite, sofern möglich, deren CMF ab. Wir bestätigen das Ergebnis von Beuther & Schilke (2004) und erhalten eine Steigung der CMF ähnlich der Salpeter IMF, für andere MSF Regionen jedoch erhalten wir eine CMF mit einer etwas flacheren Steigung als die Salpeter IMF. Der Unterschied deutet darauf hin, daß die IMF nicht zum Zeitpunkt der Fragmentation festgelegt wird, sondern vielmehr ein Ergebnis der Entwicklung der Molekularwolke ist. Diese beginnt mit einer flacheren Massenverteilung, die mit der Zeit steiler wird. Dieses ist jedoch noch kein endgültiges Ergebnis und wir empfehlen eine Serie von notwendigen Beobachtungen um dies vollständig zu testen.

Contents

Chapter 1

Introduction

1.1 The fragmentation of a cloud

It is known that stars form within Molecular Clouds. Among these clouds, the Giant Molecular Clouds (GMC) in particular have masses of $10^4 - 10^6$ $M_\odot$, average densities of $10^2 - 10^3$ cm^{-3} and temperatures on the order of $\sim$ 10 K, reaching sizes on the order of $\sim$ 10 pc. A molecular cloud will remain in hydrostatic equilibrium, until as a consequence of their low temperatures and high densities it exceeds its Jeans mass and starts to collapse. As it collapses, the cloud breaks into smaller and smaller fragments. During the collapse temperature and pressure increase and the fragments become optically thick, which makes them less efficient at radiating the potential energy as heat, thus inhibiting further fragmentation (e.g. Blitz 1993; Williams et al. 2000). Complicating this picture of a collapsing cloud are the effects of turbulence, macroscopic flows, rotation, magnetic fields and the cloud geometry. Both rotation and magnetic fields can hinder the collapse of a cloud (e.g. Hartmann 1998), while turbulence is instrumental in causing fragmentation of the cloud, and on the smallest scales it promotes collapse (e.g. Ballesteros-Paredes et al. 2007).

1.1.1 The Jeans scale of fragmentation

The fragmentation process of molecular clouds just mentioned produces the observed complex pattern of filaments, sheets, bubbles, and irregular clumps. The densest parts of the filaments and clumps are called molecular cores, and is within these dense cores that star formation takes place.

Perhaps a better way to understand the difference between molecular clouds, clumps and cores is by determining their Jeans scale. The Jeans scale or length is the minimum length-scale for gravitational fragmentation, based on the mass necessary for an object to be gravitationally bound against its thermal support. Such mass is the so-called Jeans mass, and can be estimated by comparing the gravitational and thermal energies. In the case of a uniform density sphere the Jeans length is given by

$$\lambda_J = 0.19\,\mathrm{pc}\left(\frac{\mathrm{T}}{10\mathrm{K}}\right)^{1/2}\left(\frac{\mathrm{n_{H_2}}}{10^4\,\mathrm{cm^{-3}}}\right)^{-1/2}, \qquad (1.1)$$

which also gives an estimate of the minimum initial separation for self-gravitating fragments.

As mentioned before, molecular clouds have average densities of $10^2 - 10^3$ cm^{-3} and temperatures of $\sim$ 10 K. Introducing this values in Eq. (1.1) we obtain $\lambda_J \sim 0.2 - 0.6$ pc. These resulting self-gravitating fragments are called clumps, and is within these structures where most likely a star cluster will form. As just shown, clumps have sizes on the order of $\sim$ 0.1 pc, and their densities are found to be on the order of a few 10^4 cm^{-3} to about 10^5 cm^{-3}.

If we now introduce those values in Eq. (1.1), we obtain Jeans scales on the order of $\lambda_J \sim 0.01$ pc. These structures are called molecular cores and are the densest parts of the clumps. The cores have densities of $10^4 - 10^7$ cm^{-3} and temperatures of $\sim 10 - 30$ K, and is within these dense cores that a star or a stellar system will form.

1.2 The formation of a star

1.2.1 Low-Mass Stars

Stars of different masses are thought to form by different mechanisms. In the case of stars with masses up to a few solar masses, it is fairly well known how a core evolves into a star. The dense cores in the molecular clouds will collapse, building a central protostar surrounded by an infalling envelope through which the protostar continues to accrete (Larson 1969; Shu et al. 1987). While contracting, the angular momentum excess in the core entails the formation of a rotationally supported circumstellar disk. At later stages this disk becomes the main source of infalling material onto the protostar, while molecular outflows and jets are produced via interactions with the protostar, most likely as an effect of the angular momentum of the infalling material (e.g., Richer et al. 2000). Once the protostar becomes optically visible, it moves through the Hertzprung-Russell diagram along evolutionary tracks, deriving its luminosity from gravitational contraction (Hayashi 1961; Stahler 1983; Palla & Stahler 1993). When the density and temperature in the protostar are high enough hydrogen fusion begins and the star reaches the ZAMS (e.g., Palla & Stahler 2000). For detailed reviews on different topics of low-mass star formation see, e.g., Andre et al. (2000); Lada (1999); Shu et al. (1999); Richer et al. (2000).

1.2.2 Massive Stars

In contrast, the picture for stars with masses above $\sim 8\,\mathrm{M}_\odot$ is not that clear. These stars do not have a visible pre-main sequence phase since they start the nuclear burning while still deeply embedded in the parental core, thus directly appearing in the ZAMS (Palla & Stahler 1993). The main problem in determining their formation mechanism arises from the radiative pressure that massive stars exert on the surrounding ambient cloud as soon as they ignite, pushing against infalling material. In the past decades studies demonstrated that in the classical star-formation scenario derived for low-mass stars the radiation pressure might be substantial enough to halt accretion onto the massive protostar, therefore the theory had to be adapted to account for the formation of massive stars (Kahn 1974; Wolfire & Cassinelli 1987; Bonnell et al. 1998; Stahler et al. 2000).

The proposed solutions are following mainly two paths. The most straightforward is the so-called monolithic collapse, that tries to adapt the mechanism of low-mass star formation by increasing accretion rates from $10^{-6} - 10^{-5}\,\mathrm{M}_\odot\,\mathrm{yr}^{-1}$ to $10^{-4} - 10^{-3}\,\mathrm{M}_\odot\,\mathrm{yr}^{-1}$ and letting the star accrete through circumstellar “disks”. Theoretical work has shown that the production of a jet and outflow clears a cavity through which much of the radiation from a massive protostar can escape without hindering accretion through the disk and onto the protostar (Wolfire & Cassinelli 1987; Jijina & Adams 1996; McKee & Tan 2003; Norberg & Maeder 2000; Tan & McKee 2002; Yorke & Sonnhalter 2002). Also there is mounting evidence that at least some massive protostars are indeed surrounded by accretion disks (e.g., Beuther et al. 2007a; Cesaroni et al. 2007; Fallscheer et al. 2009; Zinnecker & Yorke 2007). However, some authors caution that this scaled-up version of low-mass star formation can be feasible only up to early B stars (see Zinnecker & Yorke 2007).

The second approach to massive star-formation remains to be tested observationally. It is the theory of coalescence and competitive accretion, which suggests that massive protostars are “seeded” by low-mass protostars which compete with other protostars to draw in matter from the entire parent molecular clump instead of simply from a small local region, and that if the protostellar densities in the evolving cluster are high enough ($\sim 10^{6-8}\,\mathrm{pc}^{-3}$), then massive stars may form by the coalescence of two or more lower-mass stars (Bonnell 1997; Bonnell et al. 1998; Bonnell & Bate 2006; Davies et al. 2006; Stahler et al. 2000; Zinnecker & Bate 2002). However, recent studies in stellar rotation seem to rule out the coalescence scenario, at least for stars up to $\sim 50\,\mathrm{M}_\odot$ (e.g., Wolff et al. 2006).

1.3 To look for a Massive Star

When observing Massive Star-Forming (MSF) regions, one of the basic questions tried to be answered is: How is their mass distribution compared to the stellar Initial Mass Function (IMF)?

To answer this we have to observe MSF regions with increasing spatial resolution, probing the fragmentation of the dense cores, and trying to find the elusive high-mass pre-protostellar objects, the massive analogues to the low-mass Class 0 objects.

The problem is that observations of MSF regions are more difficult than for their low-mass counterparts, for several reasons. Most prominently, massive s tars are rare, and their evolutionary timescales are short. While a solar-type star can remain in the main sequence for $\sim 10^{10}$ years, stars with masses over $\sim 10\,\mathrm{M}_{\odot}$ will only last for a few $\sim 10^{6}$ years (Schaller et al. 1992). This in turn adds to its rarity. A direct estimate with the stellar IMF reveals that stars with masses above $\sim 8\,\mathrm{M}_{\odot}$ account for only $\sim 2\%$ of the stars born in the Galaxy in a single star-forming event. This makes the probability of finding a nearby MSF region very low. Whereas there do exist a number of low-mass star-forming (LMSF) regions within a few hundred parsecs from the Sun (e.g, Taurus-Auriga, Perseus), with a few exceptions like Orion at $\sim 420\,\mathrm{pc}$ and Cepheus at $\sim 750\,\mathrm{pc}$ (see e.g., Zinnecker & Yorke 2007), the large majority of known MSF regions are located beyond a few kiloparsecs from the Sun.

Also, unlike low-mass stars, massive stars do not form in isolated mode but seem to form exclusively in clustered mode (Stahler et al. 2000; see also Fig. 1.1). Together with their relatively large distances, this formation mode makes very difficult to disentangle single massive protostars within a protocluster. Furthermore, because they are extremely deeply embedded during all their formation phase, observations of massive protostars are challenging even in the near-infrared (e.g., Menten & Reid 1995 for the case of the BN/KL region in Orion). The most convenient regime to study the early phases of massive star formation is the sub-mm and mm range, where the continuum and molecular line emission of compact, massive cores are strong and easily detected by current single-dish antennas and interferometers.

In the last years improvements in sensitivity and angular resolution in (sub)mm interferometers are making possible to observe deeper into MSF regions and observe each time smaller cores. This has allowed us to study in more detail the physical and dynamical properties of massive protostars and cores, their small-scale outflow component and also derive the CMF of MSF regions, studying a possible link to the IMF.

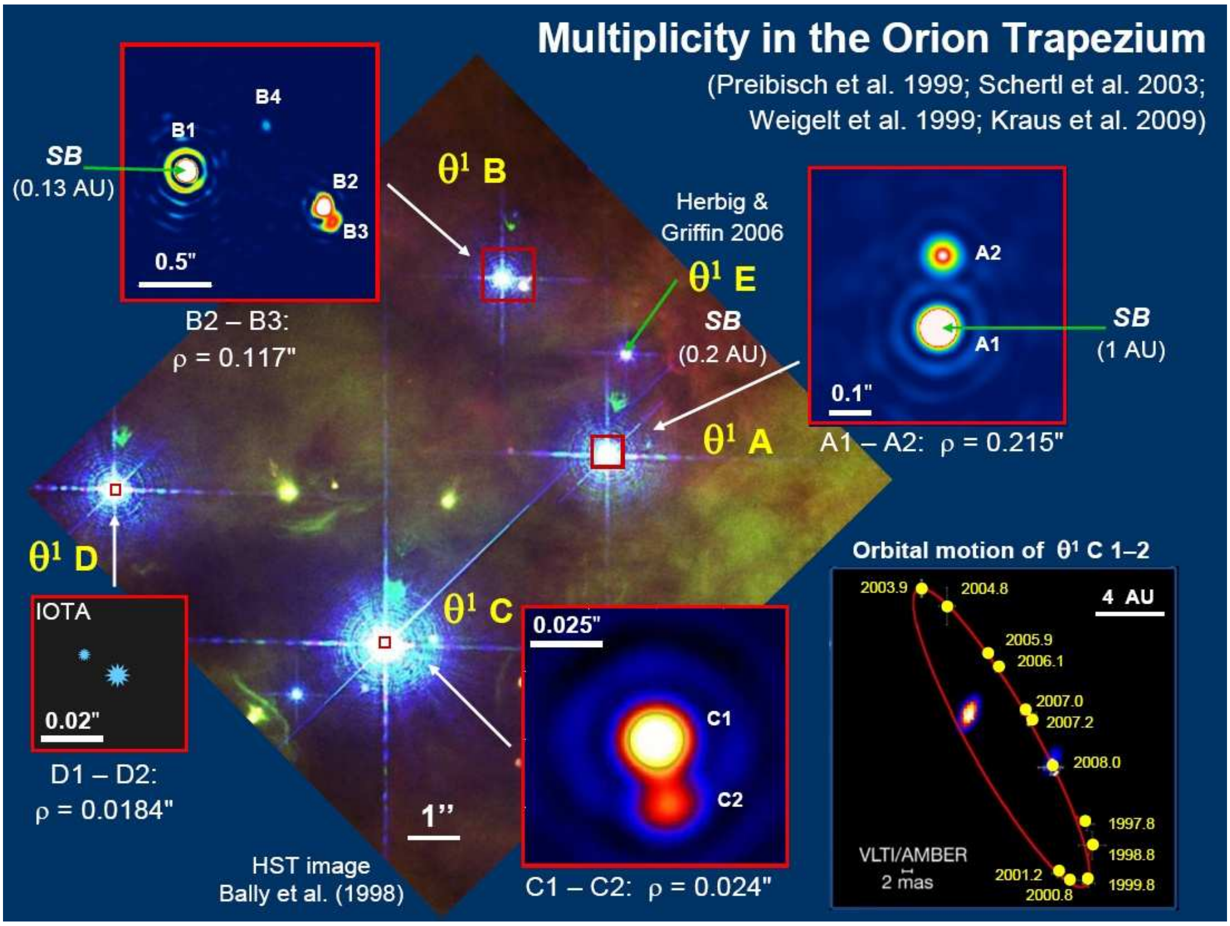

Figure 1.1: Summary of the multiplicity of the Orion Trapezium stars. The images in the figure are K-band speckle reconstructions of a few bright Orion Nebula cluster member stars of spectral type O or B. There are several visual companions of these stars, all of which seem to be low- or intermediate-mass stars (see Preibisch et al. 1999). Extrapolation with correction for the unresolved systems suggests that there are at least 1.5 companions per primary star on average. This number is clearly higher than the mean number of 0.5 companions per primary star found for the low-mass stars in the Orion Nebula cluster as well as in the field population. This suggests that a different mechanism is at work in the formation of high-mass multiple systems in the dense Orion Nebula cluster than for low-mass stars (see e.g., Bally et al. 1998; Herbig & Griffin 2006; Kraus et al. 2009; Preibisch et al. 1999; Schertl et al. 2003; Weigelt et al. 1999). Image produced by T. Preibisch, available at *http://www.usm.uni-muenchen.de/people/preibisch/*.

1.4 The IMF

The stellar IMF is the distribution function of the masses of stars formed in one event. Salpeter (1955) first suggested a power-law approximation to the mass function of stars with masses $0.4 < m/\,\mathrm{M}_\odot < 10$ of the form

$$\frac{dn}{dm} \propto m^{-\beta}, \tag{1.2}$$

with an exponent $\beta \sim 2.35$, the now so-called “Salpeter value”. More recently, Miller & Scalo (1979) studied the IMF for the mass range outside the Salpeter limits, and proposed a flattening of the IMF below $\sim 0.5\,\mathrm{M}_\odot$ and suggested the lognormal form

$$\frac{dn}{d\,(\log m)} = \frac{A}{\sqrt{2\pi}\sigma} \exp\left[-\frac{(\log m - \log m_c)^2}{2\sigma^2}\right], \tag{1.3}$$

where m_c is the mean mass and $\sigma^2 = \left\langle (\log m - \langle \log m \rangle)^2 \right\rangle$ is the variance in $\log m$.

At the present time the most widely used functional form is the power-law (1.2), but broken into three mass regimes, each one with a different value for the exponent (e.g., Chabrier 2003; Kroupa et al. 1993; Kroupa & Weidner 2005; Kroupa 2007, 2008; Pflamm-Altenburg & Kroupa 2006; Reid et al. 2002; see Fig. 1.2):

$$\frac{dn}{dm} \propto m^{-\beta_i}, \qquad i = 0, 1, 2$$

$$\begin{aligned}
\beta_0 &= 0.30 \pm 0.7, & 0.01\ m/\,\mathrm{M}_\odot &\leq 0.08 \\
\beta_1 &= 1.30 \pm 0.5, & 0.08 \leq m/\,\mathrm{M}_\odot &\leq 0.50 \\
\beta_2 &= 2.30 \pm 0.7, & 0.50 \leq m/\,\mathrm{M}_\odot &\lesssim 150
\end{aligned} \tag{1.4}$$

A substantial contribution to the determination of the uncertainties in the exponents of the IMF was made by Scalo (1998), who summarized a large part of the observational constraints on the IMF and demonstrated that the observed scatter in β can be understood as being due to Poisson uncertainties and dynamical effects, as well as arising from biases through unresolved multiple stars.

Garmany et al. (1980) studied the high-mass end of the IMF (β_2) in OB associations, and concluded that it is consistent with Salpeter. On the other hand, observational results give different values for β_2. For instance, Pflamm-Altenburg & Kroupa (2006) finds a steeper (than Salpeter) value in the Orion cluster, while Stolte et al. (2006) obtains a slope $\beta_2 \sim 1.9$ in the

NGC 3063 cluster. Nevertheless, Scalo (1998) had already noted that the high-mass slope of several young clusters and associations varies but the average slope remains similar to the Salpeter value $\beta = 2.35$.

Furthermore, the high-mass end of the IMF given by Eq. (1.4) is found to be universal despite environmental factors like metalicity or density that could change this distribution. Not only in the Galaxy, but also studies at moderate to high redshift are consistent with this Salpeter power-law (e.g., Baldry & Glazebrook (2003)). It is true, however, that in the Milky Way disk Scalo (1986) found a third slope $\beta_3 \sim 2.7$ ($m \geq 1$ M$_\odot$), a result later confirmed by several other authors as for example Reid et al. (2002) ($2.5 \leq \beta_3 \leq 2.8$), Portinari et al. (2004) and Romano et al. (2005) ($2.5 \leq \beta_3 \leq 2.7$). Nevertheless, Weidner & Kroupa (2005, 2006) showed that this third steeper slope follows naturally from the very universality of the IMF (see also Köppen et al. 2007; Kroupa 2008).

Attempts to explain the universality of the IMF follow basically two ways. One is via competitive accretion (see the review of Bonnell et al. 2007), and the second is via random sampling of fractal clouds (see e.g., Elmegreen 1997; Henriksen 1991). For a detailed discussion of these methods, see the review of Zinnecker & Yorke (2007). This universality of the IMF is the main motivation to study its assembly, and one of the drivers of this thesis.

1.5 The Core Mass Function

The life and death of a star is determined almost completely by its mass, marking the importance of knowing the distribution of masses of the newly formed stars, the IMF. But stars form in molecular clouds, and therefore the clouds' dynamical and physical properties determine the initial conditions for star formation.

In their large mm survey of the ρ Ophiuchi LMSF region Motte et al. (1998) derived a CMF with a power-law slope similar to the IMF. This led them to conclude that the cores were the direct precursors of individual stars or stellar systems. Furthermore, other star-forming regions have shown CMFs similar to the IMF (e.g., Testi & Sargent 1998; Johnstone et al. 2001; Reid & Wilson 2006; Enoch et al. 2007; Nutter & Ward-Thompson 2007; Alves et al. 2007). Several theoretical results supports a one-to-one or nearly one-to-one relationship between cores and stars (e.g., Padoan & Nordlund 2002; Scalo 1998; Matzner & McKee 2000), however the similarity between the CMF and the IMF is the only observational evidence supporting this relationship.

On the other hand, there is also evidence suggesting that this one-to-one relationship may not hold. Some cores must fragment to produce the large population of observed multiple systems, and that cores fragment is indeed found, as I show in Chapter 4. Also the fraction of cores that

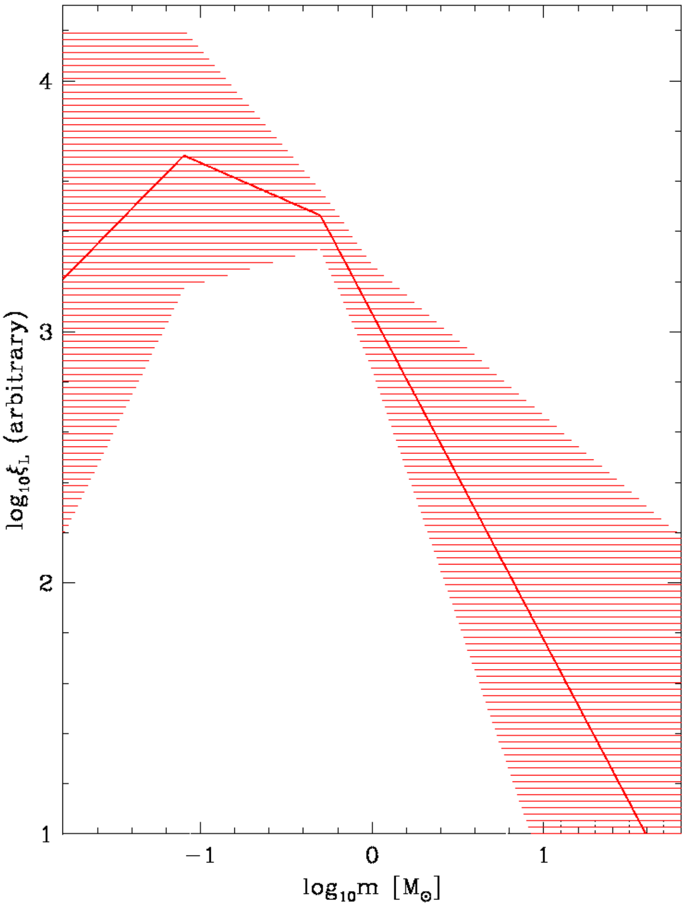

Figure 1.2: The average Galactic field IMF (Eq. 1.4) is shown as a solid line, with the associated uncertainty range. Adapted from Kroupa & Weidner (2005).

will evolve into stars is uncertain, as is for example found by Lada et al. (2008) that in the Pipe Nebula the large majority of cores are gravitationally unbound.

Different initial conditions at the moment of the fragmentation might result in different shapes of the CMF. Simulations of the evolution of molecular clouds show that if the dynamical evolution is dominated by gravity, then the slope of the mass spectrum becomes flatter than the Salpeter value (e.g., Klessen 2001). In the case of pure gravitational contraction (i.e., the cloud is gravitationally dominated), the slope is $\beta \sim -1.5$, while when the cloud is supported by turbulence the slope steepens.

In the case of gravitational fragmentation, the Jeans criterion would set a characteristic mass (the Jeans mass) and thus set the basis of the CMF. Simulations show that this kind of fragmentation produces a mass distribution extending to, and peaking at, about the Jeans mass ($\sim 0.5\,\mathrm{M}_\odot$ in the case of clumps). Subsequent processes like competitive accretion and ejection later define the shape of the high- and low-mass end of the IMF, respectively (e.g., Jappsen et al. 2006; Bonnell & Bate 2006; see the review by Bonnell et al. 2007). In contrast, feedback processes like heating from accretion can inhibit fragmentation (e.g., Krumholz 2007), thus allowing the existence of massive cores at the moment of fragmentation.

In the case of MSF regions the CMF at spatial scales of $\sim$ 0.01 pc was not determined until the work of Beuther & Schilke (2004) on IRAS 19410+2336. They found that also at those short spatial scales the CMF resembled the high-mass end of the IMF. For this thesis I have determined the CMF of MSF regions at similar spatial scales, and found contrasting results. While the result of Beuther & Schilke (2004) is confirmed taking into account the temperature structure of the cores, for other regions I find a flatter slope.

1.5.1 Cloud Mass Function

The mass functions of molecular clouds at spatial scales larger than $\sim$ 0.01 pc can also be described by a power-law in the form given by Eq. 1.2, but with slope values in the $\beta \sim 1.4 - 1.8$ range, shallower than Salpeter.

In their study of seven Galactic molecular clouds Kramer et al. (1998) showed that their mass functions have slopes in the $\beta \sim 1.6 - 1.8$ range. This was a confirmation of the results that had been found since the ’80s by several authors. Just to name a few, the studies of Brand & Wouterloot (1995); Carr (1987); Casoli et al. (1984); Dobashi et al. (1996); Kramer et al. (1996); Lada et al. (1991); Langer et al. (1993); Loren (1989); Sanders et al. (1985); Solomon et al. (1987); Solomon & Rivolo (1989); Tatematsu et al. (1993); and Williams et al. (1994, 1995) all found that the mass distribution of molecular clouds have power-law slopes between $\beta \sim 1.4$ and $\beta \sim 2.0$. Also studies in other galaxies yield values in the $\beta \sim 1.5 - 1.7$ range, as for example for the LMC, IC10 and M31 (see e.g., Blitz et al. 2007). This results suggest that also the mass function of molecular clouds is universal, and consistently shallower than the IMF.

It is not yet clear why the molecular cloud mass function and the CMF show different slopes or if there is a relationship between them, for example if the slope of the cloud mass function “evolves” into the steeper slope of the CMF. Trying to understand this difference is another of the motivations of this thesis.

1.6 Outline of this work

In this thesis I show a study of several MSF regions at high spatial resolution down to spatial scales on the order of $\sim$ 2000 AU and smaller, aimed to give insight into their fragmentation process and (proto)stellar content.

1.6.1 Observational approach

The low temperatures found in molecular clouds (see Sec. 1.1) imply that they are detected at radio wavelengths. To derive a CMF, we are interested in determine the masses of the cores within the clouds. For this we use the dust emission, that at the low temperatures of the clouds ($10 - 30$ K), is found to emit more prominently at (sub)millimeter wavelengths, since in general the dust optical depth increases with decreasing wavelength (see e.g., Ossenkopf & Henning 1994).

Therefore, the observations for this thesis were done at mm wavelengths. To calculate the mass of the cores we followed the approach of Hildebrand (1983) and assumed that the dust continuum emission is optically thin and of thermal origin, allowing us to determine the gas mass of the cores from the mm continuum emission after adopting a grain model and a gas-to-dust ratio.

To determine the mass of a core, we also need to know its temperature. In the mm regime the temperature can be determined using spectral lines of certain molecular species, as for example formaldehyde, methyl cyanide and ammonia (see e.g., Mangum & Wootten 1993; Watanabe & Mitchell 2008; Zhang et al. 1998). For our work, we observed in particular several formaldehyde transitions at $\sim$ 1.4 mm. The details of the observations will be given in the following chapters.

Since we are interested in describe the cores within the clouds we need to resolve them at distances of a few kiloparsecs. Core sizes are in the order of 0.01 pc or equivalently, about a few thousand AU, thus we require angular resolutions on the order of $\sim 1''$ and better to resolve them.

Currently, at mm wavelengths such resolution is only achievable with interferometers. At a wavelength of $\sim$ 1 mm it is possible to reach angular resolutions of some tenths of arcsecond with interferometers like the Plateau de Bure Interferometer (PdBI) or the Submillimeter Array (SMA), and at $\sim$ 7 mm and $\sim$ 13 mm the Very Large Array (VLA) can achieve resolutions even below $0.1''$ under good weather conditions. Regarding the sensitivity, at $\sim$ 1 mm is usual to reach r.m.s. noises of about 1 mJy when observing the continuum and a some 10 mJy in the case of line emission. The PdBI is currently the most sensitive array in the mm[1], and in particular is capable

---

[1] It has to be mentioned, however, that at the moment of writing this thesis the SMA has successfully upgraded

of achieve sensitivities of a few 0.1 mJy at $\sim$ 1 mm and as low as $\sim 80\,\mu$Jy at $\sim$ 3 mm.

Although in this work we rely on high-resolution interferometric observations, we often resort to larger-scale mappings with single-dish telescopes in the (sub)mm to, for example, determine the amount of flux that has been filtered by the interferometer for being emitted by large-scale structures. At this moment, antennas operating at the mm wavelength range can achieve angular resolutions in the order of $10''$. For example, the IRAM 30m Telescope has a resolution of $\sim 11''$ at $\sim$ 1.2 mm, the Effelsberg 100m Telescope achieves $\sim 10''$ at $\sim$ 3.5 mm and the James Clerk Maxwell Telescope (JCMT) reaches $\sim 14''$ at $\sim$ 0.85 mm.

Detailed technical specifications and capabilities of some state-of-the-art interferometer and single-dish antennas can be found at *http://www.vla.nrao.edu/astro/guides/vlas/current/* (VLA); *http://www.iram.fr/IRAMFR/GILDAS/doc/html/pdbi-intro-html/pdbi-intro.html* (PdBI); *http://www.jach.hawaii.edu/JCMT/* (JCMT); *http://sma1.sma.hawaii.edu/status.html* (SMA); *http://www.apex-telescope.org/* (APEX: Atacama Pathfinder Experiment); *http://www.iram.es/IRAMES/mainWiki/TelescopeSystemStatus* (IRAM 30 m).

1.6.2 Thesis Organization

This thesis is structured as follows. In Chapter 2[2] we revisit the region IRAS 19410+2336 to determine its temperature structure and thus derive better mass estimations for the cores and produce a more accurate CMF for the region. We confirm the results of Beuther & Schilke (2004), obtaining a CMF with a power-law slope similar to the Salpeter IMF, and discuss the implications this has for the theories of massive star-formation.

Continuing in Chapter 3[3] I present and analyse data on four more MSF regions observed at similar spatial resolutions as before. We take advantage of the similarities between two of those regions and derive a CMF using the cores detected in both of them. This time however, we obtain a CMF with a power-law slope flatter than the Salpeter IMF. We compare this with the results of the previous chapter, and discuss possible scenarios that might explain this difference and which observations would be needed to further investigate them. Also, we show NIR data on these MSF regions from a VLT-SINFONI survey within the framework of the FEMS project (P.I.: A. Bik, E. Puga), and highlight the importance that a multiwavelength has in the study of massive star-formation.

---

its bandwidth, improving its sensitivity in a factor $\sqrt{2}$ and now being capable of sensitivities similar to the PdBI at 1 mm, although the latter still remains as the most sensitive array in operation to date.

[2] Based on a paper submitted to *Astronomy & Astrophysics* by Rodón et al. (2009a).

[3] Based on a paper to be submitted to *Astronomy & Astrophysics* by Rodón et al. (2009b).

Then in Chapter 4[4] we go one step further in spatial resolution and I show our study of the MSF region W3 IRS5, resolved down to ~ 0.0036 pc (~ 750 AU). We are faced with the possible progenitor of a multiple stellar system similar to the Trapezium in Orion: a so-called prototrapezium system. The outflow component in the system is resolved into five small-scale outflows, and we analyse their physical properties.

Finally in Chapter 5 I present a summary of the work presented in this thesis and what can be learned from it, and potential and ongoing work in the framework of this thesis.

---

[4] Based on a paper published in *Astronomy & Astrophysics* by Rodón et al. (2008).

Chapter 2

The Core Mass Function of IRAS 19410+2336

Our understanding of the structure of the cold, dense interstellar medium (ISM) in star-forming regions has improved in the last years. In those regions the ISM exhibits a clumpy, often filamentary structure with density maxima at the sites of star formation. To represent this structure quantitatively we use the Core Mass Function (CMF). In this paper we will refer to “core” as the small (diameter D$\sim$ 0.01 pc), dense condensation that will form individual stars or small multiple systems, while with “clump” we denote structures that may form (proto)clusters and may therefore be more massive and larger than cores. In this sense, cores may be considered as a subset of clumps.

Submillimeter observations of low-mass star-forming regions such as Serpens (e.g., Testi & Sargent 1998), Orion B (e.g., Motte et al. 2001) and ρ Oph (e.g., Motte et al. 1998), as well as near-infrared extinction maps (e.g., Alves et al. 2007), show that their CMFs resemble the shape and intrinsic mass scale of the stellar Initial Mass Function (IMF; e.g., Salpeter 1955; Kroupa 2002). This suggests that these dense cores would be the immediate precursors of stars, and that by applying a more or less constant core-to-star mass conversion efficiency we can obtain the IMF from the CMF.

In the case of Massive Star-Forming (MSF) regions we have, for example, the analysis of Reid & Wilson (2006). They gathered the published masses of the MSF regions M8 (e.g, Tothill et al. 2002), M17 (e.g., Reid & Wilson 2006), NGC 7538 (e.g., Reid & Wilson 2005), W43 (e.g., Motte et al. 2003) and RCW 106 (e.g., Mookerjea et al. 2004), tracing spatial scales of clumps that correspond to (proto)clusters rather than to individual cores, and tested the fit of several functional forms for their clump mass functions. They found that in those cases, the best fit was obtained by a double power law, having a mean power-law exponent for the high-mass end consistent with the Salpeter IMF. This would again imply that by an almost one-to-one mass conversion efficiency the IMF could be obtained from the clump mass function, as in the case for low-mass star-forming regions. Similar analyses were conducted by e.g., Shirley et al. (2003); Beltrán et al. (2006).

However, this one-to-one relationship may not hold as, for example, some clumps must fragment to produce the observed quantity of multiple stellar systems (Goodwin et al. 2007). The relatively large distances ($\gtrsim 2\,\mathrm{kpc}$) of most of the known MSF regions require spatial resolution of about $1''$ to resolve the clumps into cores with sizes below $\sim 0.1\,\mathrm{pc}$. That resolution in the (sub)mm regime is only achievable with the interferometric technique. So far, only a few MSF regions have been observed in the (sub)mm with spatial resolutions good enough to resolve individual cores (e.g., Fontani et al. 2009, Rodón et al. 2008, Rathborne et al. 2008, Beuther et al. 2006), and only for one source, IRAS 19410+2336, has it been possible to determine a mass function (Beuther & Schilke 2004).

The young MSF region IRAS 19410+2336 is at a distance of 2.16 kpc (Xu et al. 2009) and has an integrated bolometric luminosity of about $10^4\,\mathrm{L}_\odot$. It is a very active star-forming site, with sources detected from X-rays down to radio wavelengths. It has H_2O and CH_3OH maser emission (Sridharan et al. 2002; Beuther et al. 2002d) and X-ray sources (Beuther et al. 2002a), denoting the ongoing formation of intermediate-to-high mass stars. The region is embedded within a cluster of over 800 components detected at NIR wavelengths (Martín-Hernández et al. 2008; Qiu et al. 2008), and it has a rich and energetic outflow component with multiple outflows detected in CO (Beuther et al. 2002c, 2003). Beuther et al. (2002b) found that the large-scale mm emission shows two massive gas clumps roughly aligned in a north-south direction that splits into several sub-sources with increasing spatial resolution (Beuther & Schilke 2004).

With their studies of the mm continuum at high spatial resolution, Beuther & Schilke (2004) were able to derive the mass function of IRAS 19410+2336, resulting in a Sapleter-like distribution. However, the strongest caveat in the derivation of that mass function was the fact that a uniform dust temperature was used in the calculation of the masses. Although they argue that the dust temperature distribution should not vary strongly, they also warn that changes in the temperature of the cores would result in a somewhat flattened slope.

We have revisited IRAS 19410+2336 observing the mm continuum at high-spatial resolution and obtaining molecular-line emission of known temperature tracers, to determine via several methods a temperature structure for it and in the end derive a more robust mass function.

2.1 Observations

2.1.1 Interferometric

We observed the two protostellar clusters of IRAS 19410+2336 with the PdBI in the *B*, *C* and *D* configurations, comprising baselines from 20m to 330m. This translates into projected baselines ranging from $\sim 7\,k\lambda$ to $\sim 120\,k\lambda$ at 3 mm and from $\sim 15\,k\lambda$ to $\sim 240\,k\lambda$ at 1.4 mm. The phase centers were set at RA(J2000) = $19^h43^m10.7^s$; Dec(J2000) = $23°44'58.4''$ ("Northern" (proto)cluster) and at RA(J2000) = $19^h43^m11.2^s$; Dec(J2000) = $23°44'03.2''$ ("Southern" (proto)cluster), and the continuum was mapped at 3 mm and 1.4 mm.

Table 2.1: Observed molecular transitions and rms of the respective maps.

Transition	ν (GHz)	Spect. Resol. (MHz)	E_{up} (K)	rms[a] (mJy beam^{-1}) North	South
$CH_3CN\,(6_0-5_0)$	110.383	0.18	18.5	10	17
$CH_3CN\,(6_1-5_1)$	110.381	0.18	25.7	10	17
$CH_3CN\,(6_2-5_2)$	110.375	0.18	47.1	10	14
$CH_3CN\,(6_3-5_3)$	110.364	0.18	82.9	10	14
$H_2CO\,(3_{0,3}-2_{0,2})$[b]	218.222	0.36	21.0	29	36
$H_2CO\,(3_{2,2}-2_{2,1})$[b]	218.476	0.36	68.1	19	30
$H_2CO\,(3_{2,1}-2_{2,0})$	218.760	0.36	68.1	23	34

[a] For a spectral resolution of 0.5 km s^{-1}

[b] rms values obtained after combining 30 m and PdBI data.

The 3 mm receiver was tuned in the upper sideband and the 1.4 mm receiver in the lower sideband. With this spectral setup we observed the H_2CO and CH_3CN transitions described in Table 2.1 with a maximum spectral resolution of 0.5 km s^{-1}, adopting a systemic velocity V_{LSR} = 22.4 km s^{-1} (Ridge & Moore 2001; Tieftrunk et al. 1998).

The phase and amplitude calibrators were 1923+210 and 2023+336 and the flux calibrators were 3C273, 2200+420, 1749+096 and 1741-038, adopting for the calibration the flux values from the SMA flux monitoring of these quasars. The data were calibrated with CLIC and then imaged with MAPPING, both part of the GILDAS package. The spectra were processed with CLASS90, also from the GILDAS package.

After imaging and deconvolution, the resulting synthesized beams for the continuum data are $1.2'' \times 0.8''$ at 1.4 mm and $2.2'' \times 1.6''$ at 3 mm. At the given distance of 2.2 kpc that means a spatial resolution of ~ 2200 and ~ 4200 AU, respectively. The continuum data for the Northern (proto)cluster have rms noise levels $\sigma \sim 0.8$ mJy beam^{-1} and $\sigma \sim 0.4$ mJy beam^{-1} at 1.4 mm and 3 mm respectively, while in the southern (proto)cluster the rms noise levels are $\sigma \sim 1.0$ mJy beam^{-1} and $\sigma \sim 0.4$ mJy beam^{-1} at 1.4 mm and 3 mm respectively. For the line data, the synthesized beams and noise levels are detailed in Table 2.1.

2.1.2 Short spacings

We obtained IRAM 30 m observations of $H_2CO\,(3_{0,3} - 2_{0,2})$ and $H_2CO\,(3_{2,2} - 2_{2,1})$ towards IRAS 19410+2336 in November 2007, taken in the on-the-fly mode with both HERA heterodyne receivers tuned at 218.222 GHz. For the backend we used the VESPA correlator, assigning 2 of its spectral bands to each HERA receiver, with a channel spacing of 320 kHz and a bandwidth of 80 MHz, resulting in a spectral resolution of 0.5 km/s at 218 GHz.

The data were processed with CLASS90. The single-dish uv-data were combined with the interferometric uv-data using MAPPING. After imaging and deconvolution we obtained a synthesized beam of $1.6'' \times 1.0''$ for the combined data. The rms levels of the combined data are shown in Table 2.1.

2.2 Results

2.2.1 Millimetric Continuum

We established a detection threshold of 4σ in our 1.4 mm continuum maps, corresponding to ~ 4 mJy beam^{-1}, M ~ 1 $M_\odot$[1] and $N(H_2) \sim 6 \times 10^{23}$cm^{-2} in the Southern (proto)cluster, and ~ 3.2 mJy beam^{-1}, M ~ 0.8 $M_\odot$[1] and $N(H_2) \sim 4.5 \times 10^{23}$cm^{-2} in the Northern (proto)cluster. In the latter we detect 7 sources, while in the former there are 19 detected sources. Fig. 2.1 shows the 1.4 mm and 3 mm continuum maps for both (proto)clusters, with the 26 sources detected at 1.4 mm marked with triangles and the two sources only detected at 3 mm marked with squares.

The properties of the sources are summarized in Table 2.2. Cols. 2 and 3 give their absolute positions, the measured peak flux intensity and integrated flux density are given in Cols. 4 and 5 respectively.

---

[1] For $T_{kin} \sim 40$ K (see Secs. 2.2.1 and 2.3.1 for more details).

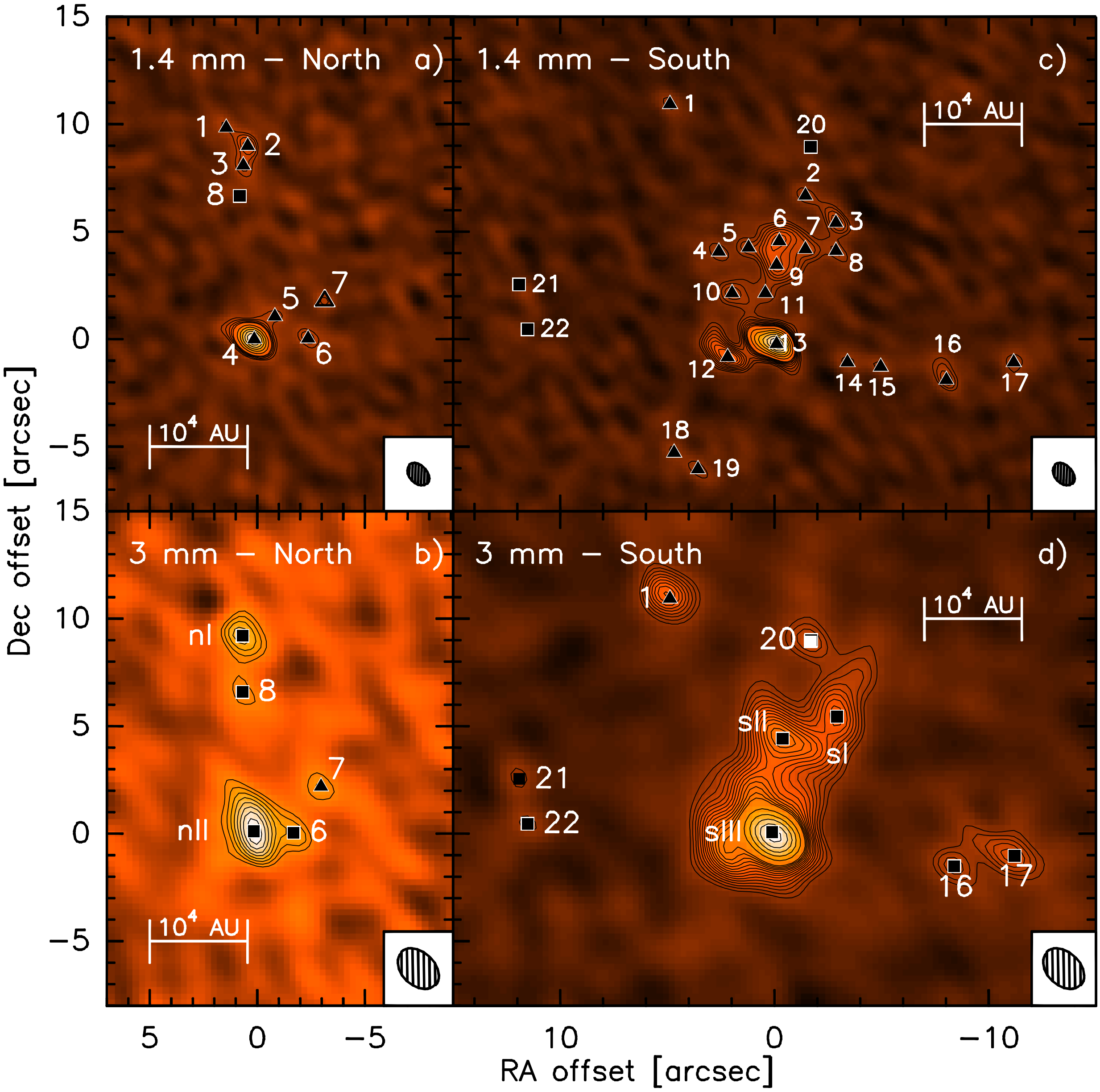

Figure 2.1: Continuum maps of IRAS 19410+2336 obtained with the PdBI. On the top row are the 1.4 mm maps of the Northern -panel a)- and Southern -panel c)- (proto)clusters. Similarly, on the bottom row are the 3 mm maps of the Northern and Southern (proto)clusters in panels b) and d) respectively. The contouring stars at the 4σ level in all the panels, increasing in 1σ steps first and in 4σ steps afterwards (see Table 2.2 for the σ values). The triangles mark the position of the sources detected at 1.4 mm while the squares are the sources detected at 3 mm. A square appearing in a 1.4 mm map indicates a source that is only detected at 3 mm. Similarly, a triangle in a 3 mm map signals a source detected at the same position in a 1.4 mm map.

Because the brightness temperature at 1.4 mm of the corresponding Planck function for the strongest source in the region is about 2 K, just ~ 2% of the typical hot core temperatures of ~100 K, we can assume that the emission comes from optically thin dust and thus calculate the masses and column densities with the approach outlined by Hildebrand (1983) and adapted by Beuther et al. (2002b, 2005). We adopted a distance of 2.2 kpc, and used a grain emissivity index $\beta = 2$, corresponding to a dust opacity per unit mass $\kappa_{1.4\,mm} \sim 0.3$ and $\kappa_{3\,mm} \sim 0.08\,\mathrm{cm}^2\,\mathrm{g}^{-1}$ for a median grain size $a = 0.1\,\mu$m, a grain mass density $\rho = 3\,\mathrm{g\,cm}^{-3}$, and a gas-to-dust ratio of 186 (Draine et al. 2007). The calculated masses and H_2 column densities are in Cols. 7 and 8 of Table 2.2, respectively. For their calculation we used the temperatures shown in Col. 7 of Table 2.4. Those temperatures were determined from the measured H_2CO line ratios, following the procedure explained and discussed in Sec. 2.3.2.

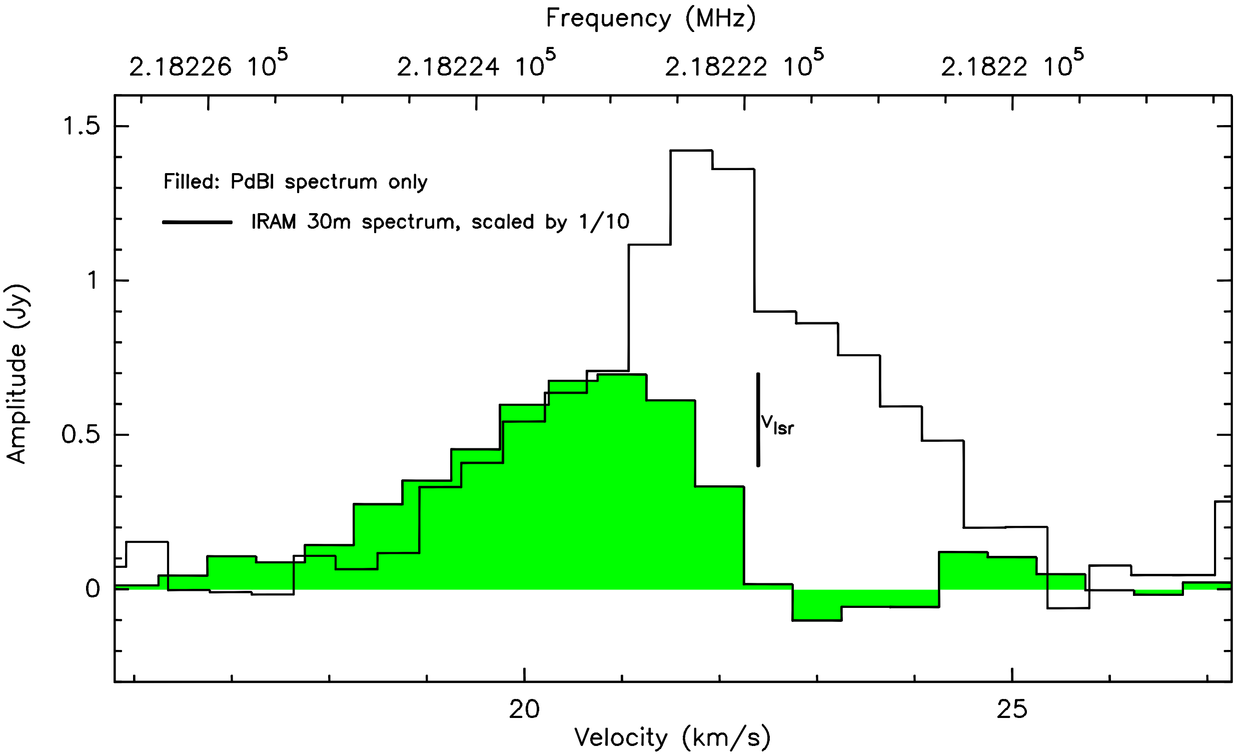

Figure 2.2: Comparison of the interferometer (PdBI, filled) and single-dish (IRAM 30m, solid line) $H_2CO\,(3_{0,3} - 2_{0,2})$ line emission towards IRAS 19410+2336. Clearly seen is the “self-absorption”-like feature in the PdBI emission, denoting the missing flux, coming from more extended spatial-scales and filtered out by the interferometer. The single-dish spectrum has been scaled down for comparison by a factor 10.

Table 2.2: Properties of the continuum millimetric sources in IRAS 19410+2336.

Source	R.A. (J2000)	Dec. (J2000)	I_ν (mJy beam^{-1})	S_ν (mJy)	T_{kin}[a] (K)	Mass ($M_\odot$)	$N(H_2)$ (10^{23}cm^{-2})	A_v (10^3 mag)	Flags[b]
1.4 mm with 1.2″ × 0.8″ beam									
1-s …	19 43 11.553	23 44 14.15	4.8	1.1	35	1.5	8.2	0.9	*u*
2-s …	19 43 11.093	23 44 09.90	5.7	2.4	35	1.7	9.6	1.0	*u*
3-s …	19 43 10.989	23 44 08.64	8.1	8.3	35	2.5	14	1.5	
4-s …	19 43 11.387	23 44 07.29	5.3	2.9	35	1.6	9.0	1.0	*u*
5-s …	19 43 11.286	23 44 07.49	6.2	3.7	35	1.9	10	1.1	*u*
6-s …	19 43 11.182	23 44 07.78	1.1	16	35	4.9	19	2.0	
7-s …	19 43 11.093	23 44 07.41	7.6	7.7	35	2.4	13	1.4	
8-s …	19 43 10.989	23 44 07.33	5.6	4.0	35	1.7	9.4	1.0	*u*
9-s …	19 43 11.191	23 44 06.68	1.0	14	35	4.3	17	1.8	
10-s …	19 43 11.342	23 44 05.37	7.2	11	35	3.4	12	1.3	
11-s …	19 43 11.229	23 44 05.37	5.6	4.5	35	1.7	9.5	1.0	*u*
12-s …	19 43 11.357	23 44 02.39	1.3	24	45	5.5	17	1.8	
13-s …	19 43 11.191	23 44 03.00	4.2	75	90	8.1	25	2.7	
14-s …	19 43 10.950	23 44 02.15	4.6	0.9	35	1.4	7.8	0.8	*u*
15-s …	19 43 10.837	23 44 01.94	4.8	0.9	35	1.5	8.1	0.9	*u*
16-s …	19 43 10.614	23 44 01.33	7.3	6.4	35	2.0	12	1.3	

Continued on next page…

Table 2.2 – Continued

Source	R.A. (J2000)	Dec. (J2000)	I_ν (mJy beam^{-1})	S_ν (mJy)	T_{kin}[a] (K)	Mass ($M_\odot$)	$N(H_2)$ (10^{23}cm^{-2})	A_v (10^3 mag)	Flags[b]
17-s …	19 43 10.385	23 44 02.15	5.1	2.5	35	1.6	8.7	1.0	*u*
18-s …	19 43 11.539	23 43 57.94	4.6	1.0	35	1.4	7.8	0.8	*u*
19-s …	19 43 11.458	23 44 57.17	5.3	2.5	35	1.6	9.0	1.0	*u*
1-n …	19 43 10.801	23 45 08.26	3.4	0.3	35	1.0	5.8	0.6	*u*
2-n …	19 43 10.728	23 45 07.41	6.1	4.0	35	1.2	10	1.0	
3-n …	19 43 10.743	23 45 06.51	4.5	2.4	35	1.4	7.6	0.8	*u*
4-n …	19 43 10.706	23 44 58.42	2.7	32	60	5.3	25	2.7	
5-n …	19 43 10.636	23 44 59.48	3.6	1.3	50	0.7	4.1	0.4	*u*
6-n …	19 43 10.524	23 44 58.45	4.7	2.4	35	1.4	7.9	0.8	*u*
7-n …	19 43 10.469	23 45 00.2	3.6	0.5	35	1.1	6.1	0.6	*u*
			3 mm with 2.2″ × 1.6″ beam						
1-s …	19 43 11.558	23 44 14.41	5.1	4.8	40	18.7	31	3.3	
20-s …	19 43 11.073	23 44 12.23	3.1	2.1	40	8.2	19	2.0	*n*
c3mm-sI …	19 43 10.986	23 44 08.67	4.8	6.7	40	26.2	29	3.1	c(2,3,8-s)
c3mm-sII …	19 43 11.170	23 44 07.64	6.6	13	40	50.8	40	4.2	c(5,6,7,9-s)
c3mm-sIII …	19 43 11.206	23 44 03.29	17.7	48	40	187.5	102	10.8	c(10,11,12,13-s)
16-s …	19 43 10.587	23 44 01.71	2.9	1.8	40	11.2	18	1.9	*u*
17-s …	19 43 10.382	23 44 02.20	3.5	3.9	40	15.2	22	2.3	
21-s …	19 43 12.066	23 44 05.76	2.0	0.2	40	7.9	12	1.3	*u*, *n*

Continued on next page…

Table 2.2 – Continued

Source	R.A. (J2000)	Dec. (J2000)	I_ν (mJy beam^{-1})	S_ν (mJy)	T_{kin}[a] (K)	Mass ($M_\odot$)	N(H_2) (10^{23}cm^{-2})	A_v (10^3 mag)	Flags[b]
22-s . . .	19 43 12.037	23 44 03.68	2.0	0.3	40	7.7	12	1.3	*u*, *n*
c3mm-nI . . .	19 43 10.746	23 45 07.63	3.2	2.3	40	12.7	20	2.1	*u*, c(1,2,3-n)
8-n . . .	19 43 10.746	23 45 05.01	1.9	0.5	40	7.5	12	1.2	*u*, *n*
c3mm-nII . . .	19 43 10.707	23 44 58.54	5.1	7.4	40	29.0	31	3.3	c(4,5-n)
6-n . . .	19 43 10.573	23 44 58.47	2.6	1.2	40	10.2	16	1.7	*u*
7-n . . .	19 43 10.480	23 45 00.61	2.2	0.6	40	8.5	13	1.4	*u*

[a] Derived from the H_2CO emission, the 3 mm temperatures are the average in the region (see Sec. 2.3.1 and Table 2.4).

[b] The last column indicates unresolved cores (*u*) and detections at 3 mm without counterpart at 1.4 mm (*n*). The c(X,Y,Z) flag indicates that the source is the unresolved combination of sources X, Y and Z. If the source is unresolved, its mass in Col. 6 is calculated with the peak intensity value of Col. 4.

The masses obtained are strongly affected by the spatial filtering inherent to interferometers. While varying dust properties may account for the discrepancy between the masses calculated at 1.4 mm and 3 mm, the spatial filtering is most likely the cause. Our shortest baseline of 20m at the given distance of 2.2 kpc corresponds to a spatial scale of ~ 38000 AU at 1.4 mm, therefore any structure larger than this was not detected. Comparison with single-dish data (Beuther et al. 2002b) indicate that only ~ 6% of the flux at 1.4 mm was recovered, the remaining flux being part of the filtered out large-scale common envelope (see Sec. 2.4.1 for further discussion).

The visual extinctions in Col. 9 were calculated assuming $A_v = N(H_2)/0.94 \times 10^{21}$ (Frerking et al. 1982).

2.2.2 Formaldehyde

With the purpose of estimating the kinetic temperature structure of IRAS 19410+2336, we observed three H_2CO transitions known to function as a gas thermometer (e.g., Mangum & Wootten 1993, see Sec. 2.3.2).

As mentioned before, the PdBI data are clearly affected by missing short spacings (an example of this is shown in Fig. 2.2), therefore the region was also observed with the IRAM 30m telescope. Fig. 2.3 shows the integrated intensity maps of the combined PdBI+IRAM 30m data.

Of the three detected H_2CO lines, $H_2CO\,(3_{0,3} - 2_{0,2})$ and $H_2CO\,(3_{2,2} - 2_{2,1})$ are the ones with the best signal-to-noise ratio. According to Mangum & Wootten (1993) those two transitions are enough to determine temperatures, therefore we did not use the third detected transition, $H_2CO\,(3_{2,1} - 2_{2,0})$, for the temperature analysis.

Both $H_2CO\,(3_{0,3} - 2_{0,2})$ and $H_2CO\,(3_{2,2} - 2_{2,1})$ have their strongest emission peak towards the brightest mm source detected in the continumm in both the north and south (proto)clusters. The secondary peaks in all the maps are in the same spatial region as the continuum emission, with the notable exception of an emission feature seen in the northern cluster at both $H_2CO\,(3_{0,3} - 2_{0,2})$ and $H_2CO\,(3_{2,2} - 2_{2,1})$ transitions ~ $4''$ southeast of the main peak, marked with a star in panels -a- and -b- of Fig. 2.3. The feature is at the rest velocity, and we detect continuum emission neither at 1.4 mm nor at 3 mm at that position.

The first-moment maps of the combined PdBI+30m data (see Fig. 2.4) show only a small velocity dispersion of ~ 1 kms^{-1} in both (proto)clusters for the observed H_2CO lines. Similarly, the second-moment maps show no strong variation over the (proto)clusters.

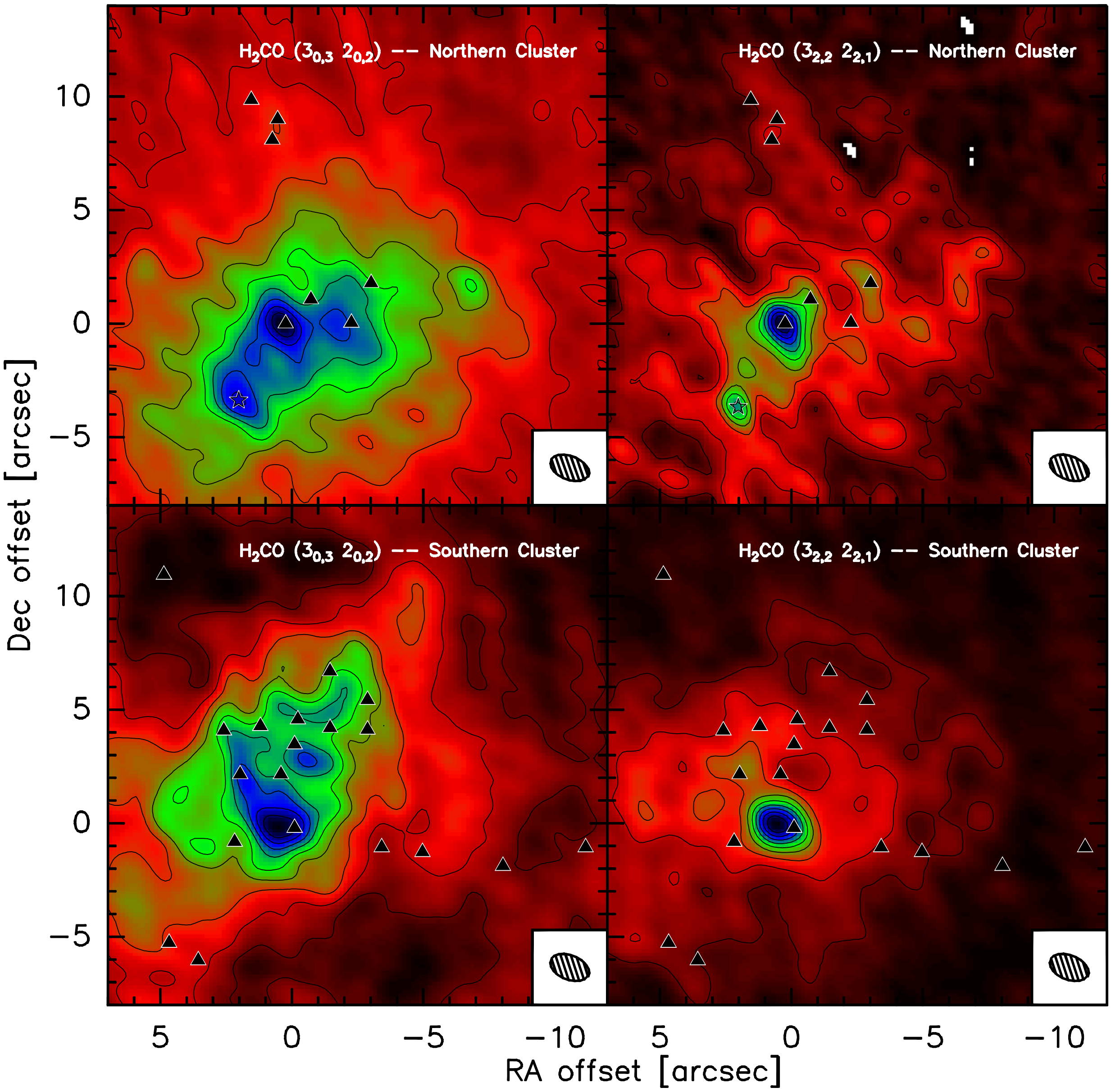

Figure 2.3: Combined PdBI and IRAM 30m integrated emission of H_2CO towards IRAS 19410+2336. In the left side is the $H_2CO\,(3_{0,3} - 2_{0,2})$ transition in the Northern (upper panel) and Southern (lower panel) (proto)clusters, and in the right side of the image is the $H_2CO\,(3_{2,2} - 2_{2,1})$ transition. The contour levels are in 10% steps of the peak integrated intensity for each map. The triangles mark the continuum sources detected, and the $1.6'' \times 1''$ beam appears in the lower-right corner of each panel.

2.2.3 Methyl Cyanide

We observed the $K = 0 - 3$ components of the $CH_3CN(J = 6 \rightarrow 5)$ K-ladder, which is useful to determine temperatures. We detected CH_3CN emission only towards sources 13-s, 6/7/9-s and 4-n. Fig. 2.5 shows the CH_3CN spectra toward those three positions.

The K=0 and K=1 components were detected at the three positions, however, we only detect the K=2 and K=3 components towards 13-s, implying that this source is the warmest in the region. Also there is a tentative detection of the K=2 component towards 4-n.

In this case, the data are barely affected by missing short-spacings, indicating the compact nature of the emitting sources.

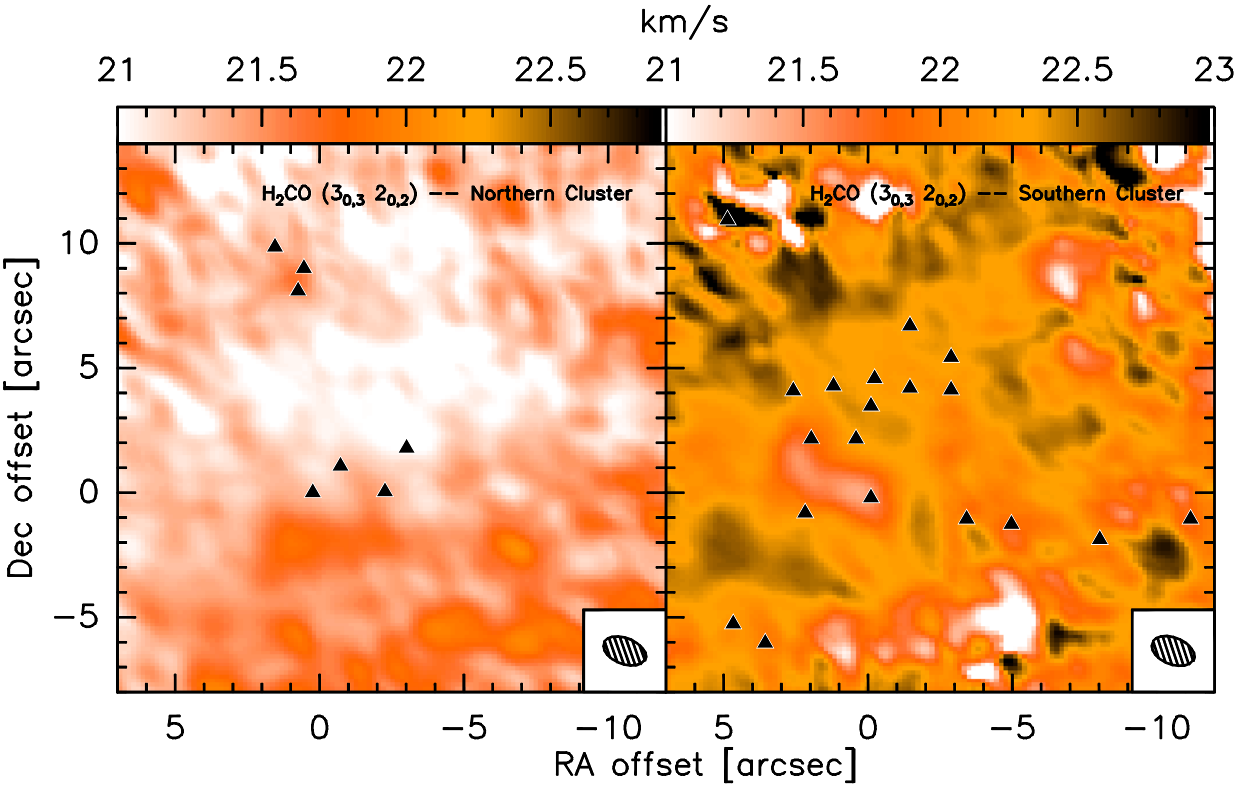

Figure 2.4: Combined PdBI and IRAM 30m first moment maps of $H_2CO\,(3_{0,3} - 2_{0,2})$ towards IRAS 19410+2336 for the Northern (upper panel) and Southern (lower panel) (proto)clusters. The triangles mark the continuum sources detected, and the beam appears in the lower-right corner of each panel. We can see how there is no signature of a strong velocity dispersion.

2.3 Deriving the Core Mass Function

2.3.1 Temperature determination

One of the major caveats of Beuther & Schilke (2004) in deriving a CMF for IRAS 19410+2336 was the assumption of a uniform kinetic temperature for both north and south (proto)clusters when deriving the masses of the cores. In this work, we were able to derive a temperature structure for each of the (proto)clusters, therefore obtaining a more accurate mass for the cores and a more reliable CMF.

Applying H_2CO line ratios

Formaldehyde (H_2CO), one of the first polyatomic molecules discovered in space, has proven its uselfulness to derive physical properties of the interstellar gas. In particular, H_2CO allows one to estimate the kinetic temperature and the spatial density in star-forming regions.

H_2CO is a well known kinetic temperature determinator (e.g., Mangum & Wootten 1993; Jansen et al. 1994, 1995; Mühle et al. 2007; Watanabe & Mitchell 2008). Because it is an asymetric rotor, transitions between energy levels with different K are only collisionally excited. Therefore the comparison between the level populations from different K components from the same $\Delta J = 1$ transition gives a measure of the kinetic temperature of the medium (Mangum & Wootten 1993).

In this work, we used the line intensity ratios of the $H_2CO\,(3_{0,3} - 2_{0,2})$ and $H_2CO\,(3_{2,2} - 2_{2,1})$ transitions, with energies $E_{up} \sim 21$ K and $E_{up} \sim 68$ K, respectively. These transitions meet the criteria previously mentioned and are only ~ 254 MHz apart, therefore they could be observed within the same spectral setup of the PdBI receivers and the HERA heterodyne. In this way, possible instrumental uncertainities such as telescope efficiency as a function of wavelength, or receiver and pointing instabilities, can be disregarded, thus obtaining a line ratio that is not affected by instrumental effects.

From the combined PdBI+30m H_2CO data we extracted spectra towards the positions of each of the 26 sources detected at 1.4 mm, and processed them with CLASS90. Some of the spectra are shown in Fig. 2.6, and the obtained line parameters in Tables 2.3 and 2.4.

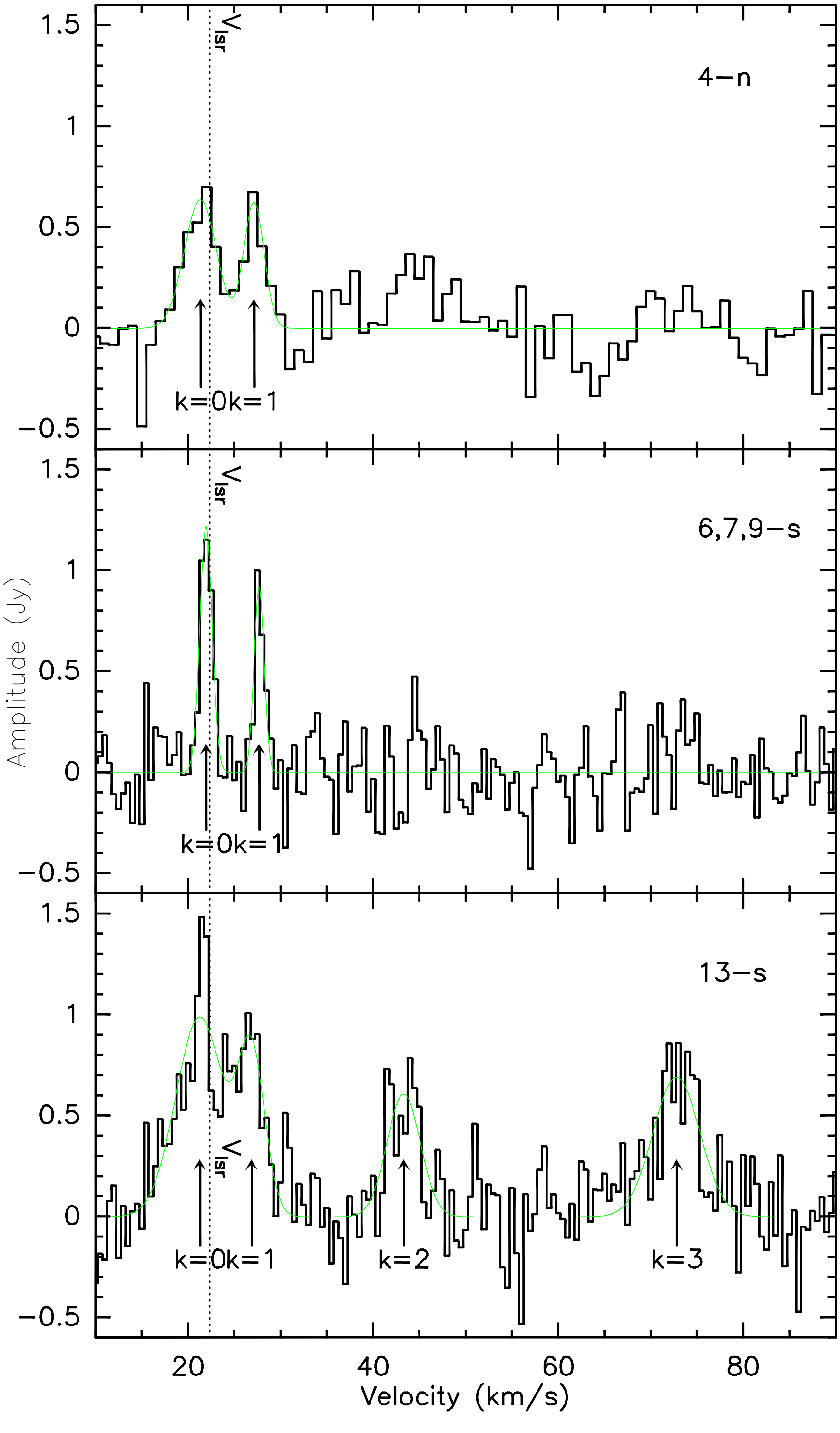

Figure 2.5: Observed CH_3CN spectra towards sources 13-s; 6,7,9-s and 4-n. Marked with arrows are the *K*-components detected in each case, and with a dotted line the rest velocity. The green solid line is the best gaussian fit for the lines, obtained with CLASS, the resulting line parameters are in Table 2.5. Only for 13-s were detected the four *K*-components, indicating a warmer environment.

LVG modeling

Once we obtained the $R = H_2CO\,(3_{0,3} - 2_{0,2})/H_2CO\,(3_{2,2} - 2_{2,1})$ line ratios, they were compared with LVG model predictions of the behaviour of R as a function of molecular hydrogen density (n_{H_2}), formaldehyde column density [$N\,(H_2CO)$] and kinetic temperature (T_{kin}). To constrain T_{kin} for the sources, either n_{H_2} or $N\,(H_2CO)$ in the region must be given.

The hydrogen number density could be estimated from our data. With the continuum emission measured towards the positions of the different sources detected, we estimate a molecular hydrogen column density [$N\,(H_2)$] ranging from $\sim 5 \times 10^{23}\,\mathrm{cm^{-2}}$ to $\sim 6 \times 10^{24}\,\mathrm{cm^{-2}}$ with a mean value of $\sim 10^{24}\,\mathrm{cm^{-2}}$. For this calculation we assumed a priori a uniform temperature $T_{kin} = 46\,\mathrm{K}$ (Beuther & Schilke 2004). However, after determining the temperature structure for the (proto)clusters, the mean $N\,(H_2)$ did not deviate significantly from the previous value despite the changes introduced by the different temperature values.

Considering spherical symmetry for the (proto)clusters, at the given distance of 2.2 kpc and if θ is the angular diameter of the (proto)cluster, the relationship

$$n_{H_2} = 1.5 \times 10^{-16} \left[\frac{N\,(H_2)}{\mathrm{cm^{-2}}}\right] \left(\frac{\mathrm{kpc}}{\mathrm{d}}\right) \left(\frac{\mathrm{arcsec}}{\theta}\right) \mathrm{cm^{-3}} \tag{2.1}$$

gives an average value $n_{H_2} \sim 10^{7}\,\mathrm{cm^{-3}}$ for each (proto)cluster addopting an approximate size $\theta \sim 9''$ for the (proto)clusters.

In contrast to n_{H_2}, we cannot directly measure the value of $N\,(H_2CO)$ from our data. Values for the H_2CO abundance relative to molecular hydrogen are reported in the range of $X\,(H_2CO) \sim 10^{-9} - 10^{-12}$, for $n_{H_2} \sim 10^{4-6}\,\mathrm{cm^{-3}}$ (e.g., Wootten et al. 1978; Mundy et al. 1987; Carey et al. 1998; van der Tak et al. 2000a), therefore calculations of an average $N\,(H_2CO)$ assuming an $X\,(H_2CO)$ value from the literature would introduce a high degree of uncertainity.

To constrain the value of $N\,(H_2CO)$ we performed a least-squares $\left(\chi^2\right)$ minimization of the $H_2CO\,(3_{0,3} - 2_{0,2})$ and $H_2CO\,(3_{2,2} - 2_{2,1})$ line intensities as a function of n_{H_2} and $N\,(H_2CO)$ for the strongest source in the region. In Fig. 2.7 we show the χ^2 surface plot at 100 K for source 13-s with the contours denoting the $1\sigma, 2\sigma$ and 3σ levels, and the star marking the minimum, corresponding to $N\,(H_2CO) \sim 10^{14.5\pm0.1}\mathrm{cm^{-2}}$. It can also be seen that the minimum χ^2 corresponds to a value $n_{H_2} \sim 10^{6.4\pm1.0}\,\mathrm{cm^{-3}}$. This agrees to within 1σ with the previously calculated $n_{H_2} \sim 10^{7}\,\mathrm{cm^{-3}}$.

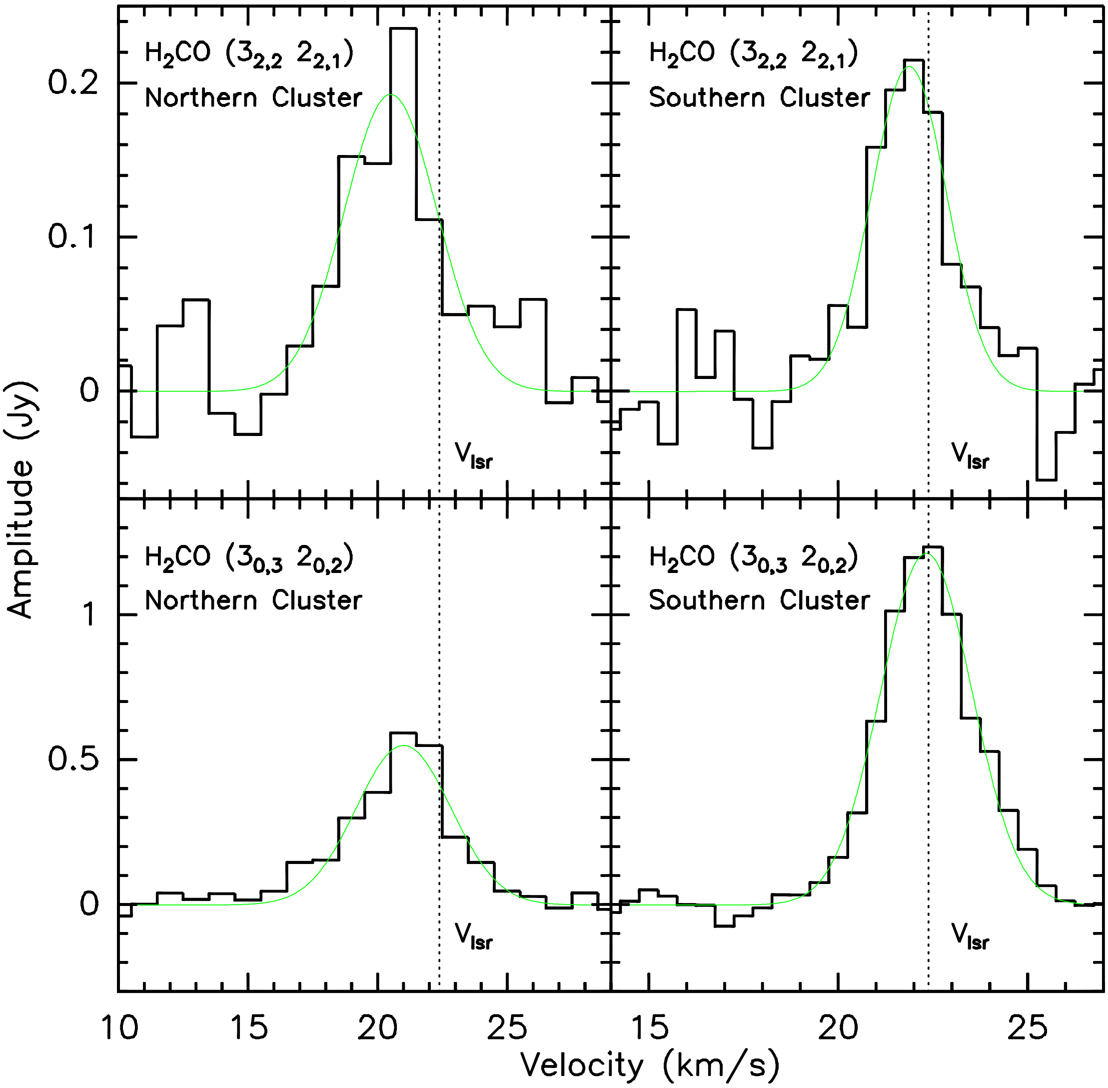

Figure 2.6: H_2CO spectra of the main sources in each (proto)cluster of IRAS 19410+2336. In the bottom row are the $H_2CO\,(3_{0,3} - 2_{0,2})$ spectra for sources 4-n (left panel) and 13-s (right panel), and similarly in the upper row are the $H_2CO\,(3_{2,2} - 2_{2,1})$ spectra for those two sources. To each spectrum was fitted a gaussian profile, shown with a green solid line. The dotted line marks the rest velocity adopted for the observations.

Table 2.3: H_2CO line parameters of the detected cores.

	$H_2CO\,(3_{0,3}-2_{0,2})$						$H_2CO\,(3_{2,2}-2_{2,1})$					
Source	$\int T_b\,dv$	σ	v_c	σ	Width	σ	$\int T_b\,dv$	σ	v_c	σ	Width	σ
	(K km s^{-1})		(km s^{-1})		(km s^{-1})		(K km s^{-1})		(km s^{-1})		(km s^{-1})	
1-s[a]	…	…	…	…	…	…	1.0	0.4	20.4	0.6	2.7	1.2
2-s	45.7	0.8	22.2	0.1	3.0	0.1	4.5	0.8	21.7	0.2	2.5	0.6
3-s	40.8	0.9	22.3	0.1	2.8	0.1	3.5	0.4	21.3	0.1	1.7	0.3
4-s	51.8	0.8	22.3	0.1	2.8	0.1	7.4	0.7	21.9	0.1	2.3	0.3
5-s	54.4	0.8	22.3	0.1	2.9	0.1	7.4	0.8	21.5	0.1	2.6	0.4
6-s	56.3	1.1	22.2	0.1	2.9	0.1	6.8	0.8	21.4	0.2	3.5	0.6
7-s	54.6	0.8	22.2	0.1	2.8	0.1	5.9	0.8	21.0	0.2	2.4	0.4
8-s	39.0	0.9	22.3	0.1	3.0	0.1	4.1	0.4	20.9	0.1	2.2	0.2
9-s	62.7	0.6	22.2	0.1	2.9	0.1	7.3	0.5	21.6	0.1	2.6	0.2
10-s	61.2	1.3	22.3	0.1	3.1	0.1	9.3	1.2	21.5	0.2	3.2	0.5
11-s	58.3	1.0	22.1	0.1	2.8	0.1	8.4	0.9	21.3	0.1	2.6	0.3
12-s	38.7	0.6	22.1	0.1	2.8	0.1	8.0	1.1	21.3	0.2	2.9	0.5
13-s	83.5	0.8	21.6	0.1	3.8	0.1	21.7	0.8	20.8	0.1	3.0	0.1
14-s	13.3	0.7	22.1	0.1	2.1	0.1	5.1	0.8	21.2	0.2	2.9	0.6
15-s	21.6	1.1	22.3	0.1	3.1	0.2	1.0	0.4	21.4	0.1	0.5	1.2
16-s	8.6	0.8	22.2	0.1	2.3	0.3	0.8	0.4	21.3	0.2	0.9	0.6
17-s	10.8	0.7	22.4	0.1	2.5	0.2	1.4	0.3	22.2	0.1	0.7	0.3
18-s	25.3	0.9	22.4	0.1	2.8	0.1	2.3	0.5	21.5	0.1	0.7	0.1
19-s	21.6	0.8	22.4	0.1	2.5	0.1	3.1	0.5	22.0	0.3	2.8	0.5
1-n	3.3	0.7	21.3	0.5	4.0	1.1	2.3	0.9	23.9	1.8	9.3	3.5
2-n	4.2	0.6	21.1	0.2	3.0	0.6	1.3	0.6	20.7	0.3	1.6	1.1
3-n	5.1	0.7	21.3	0.2	3.4	0.6	2.5	0.9	22.8	0.9	4.9	2.1
4-n	35.6	1.1	21.0	0.1	4.3	0.2	12.2	1.2	20.5	0.2	4.2	0.5
5-n	13.6	0.9	21.2	0.1	2.4	0.2	6.0	1.0	20.2	0.2	3.2	0.7
6-n	20.2	0.9	21.3	0.1	2.8	0.1	3.4	0.8	20.7	0.3	2.3	0.7
7-n	16.4	1.3	20.6	0.1	2.7	0.3	5.9	0.7	20.5	0.2	4.1	0.6

[a] No detection in $H_2CO\,(3_{0,3}-2_{0,2})$

Once the average N (H_2CO) value was determined, we compared the LVG model predictions of the behaviour of R as a function of N (H_2CO) and T_{kin} for $n_{H_2} \sim 10^7$ cm^{-3} with the observed R values. Fig. 2.8 shows the comparison. The dotted black contours are the modeled R values from 1 to 10 by $R = 1$ steps, while the solid red contours are the observed R for sources 3-s, 12-s, 13-s and 19-s (for viewing simplicity, we only plot a few sources here). The vertical dashed line and dotted lines mark the previosuly obtained value log N (H_2CO) ~ 14.5, which can be considered as an upper limit since it was derived for the brightest source, with the highest N (H_2).

For $n_{H_2} \sim 10^7$ cm^{-3}, the calculated upper limit N (H_2CO) puts the cores close to the optically thin/thick regime turnover. This turnover is hinted at in the behavior of the contour lines in Fig. 2.8, and is located at N (H_2CO) ~ 10^{15} cm^{-2}. At higher values the temperature is no longer sensitive to the column density, which indicates the onset of the optically thick regime. Another method to estimate the optical depth is by comparing the kinetic temperature T_{kin} with the bightness temperature T_b. We find that T_b is systematically lower than T_{kin} (see Table 2.4), therefore if we assume beam-filling the medium is optically thin.

Near to the turnover, the uncertainty in the temperature becomes larger, and in this case we see that it is approximately ~ 15 K. To derive this value we considered the uncertainty of $\sigma \sim 0.2$ dex in the derivation of N (H_2CO). Shifting our upper value for N (H_2CO) by that amount, the derived temperature varies by ~ 15 K for 13-s, the brightest source. This can be seen in Fig. 2.8, where it can also be noticed that this effect is smaller for the sources with lower column density.

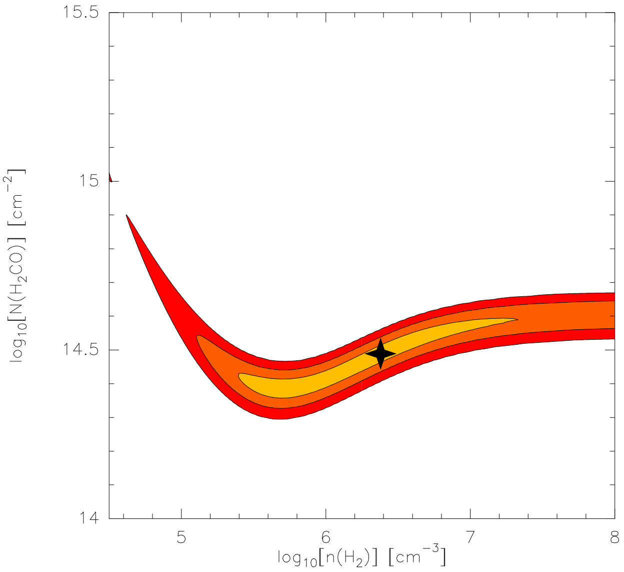

Figure 2.7: χ^2 surface plot for source 13-s. The contours mark the 1σ, 2σ and 3σ levels, and the star marks the minimum χ^2, corresponding to N (H_2CO) ~ $10^{14.5\pm0.1}$cm^{-2} and $n_{H_2} \sim 10^{6.4\pm1.0}$ cm^{-3}.

It was not possible to determine a T_{kin} value for all the cores due to either the absence of emission in one of the H_2CO lines used (e.g. source 1-s), or the low S/N ratio of one or both of the H_2CO lines (e.g., sources 1-n, 14-s). Therefore, based on its continuum flux and relative location in the (proto)cluster, we separated the cores into several groups. For each of these groups an average value of T_{kin} was determined based on the values obtained for each of the sources within the group. Col. 7 of Table 2.4 contains the kinetic temperature values assigned to each group which are used to determine the masses and N (H_2) of the cores shown in Table 2.2, and to build the mass distribution to fit the CMF.

The temperatures obtained range from $\sim$ 35 K to $\sim$ 90 K (see Table 2.4), with an average value of $\sim$ 40 ± 15 K for the whole region. This average is in agreement with the $T_{kin} \sim 46$ K derived based on IRAS far-infrared observations (Beuther & Schilke 2004).

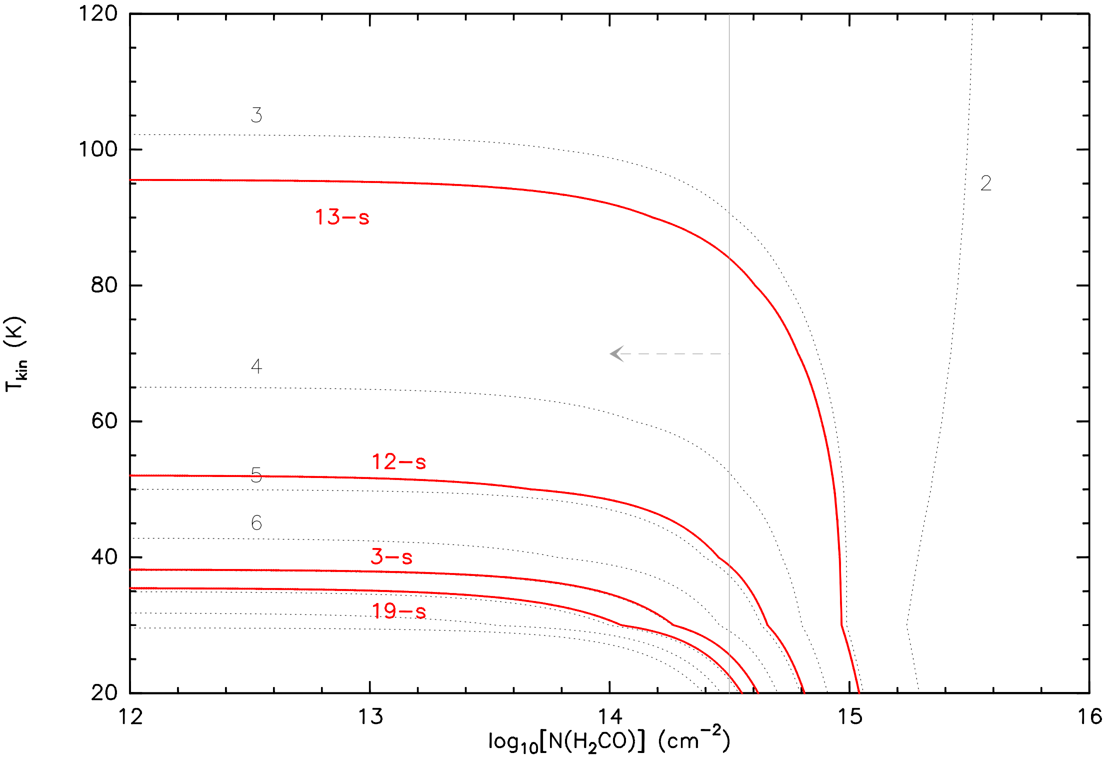

Figure 2.8: Behaviour of the $R = H_2CO\,(3_{0,3} - 2_{0,2})/H_2CO\,(3_{2,2} - 2_{2,1})$ ratio. The dotted contours represent the R values from the LVG model for $n_{H_2} \sim 10^7\,\mathrm{cm}^{-3}$ (see Sec. 2.3.1) and go from 2 to 10 in unit steps. The red solid contours are the observed R values, here we plot them for cores 3-s, 12-s, 13-s and 19-s for viewing simplicity. The vertical grey solid line is the N (H_2CO) upper limit value obtained with the LVG model. Also seen is the effect of the optically thin/thick turnover, which introduces the largest uncertainity in the T_{kin} estimation.

The CH_3CN k-ladder spectra

Methyl cyanide (CH_3CN) is a dense gas $\left(n \gtrsim 10^5\,cm^{-3}\right)$ tracer and can also be used as a temperature determinator. As described previosuly in Sec. 2.2.3 we only detect CH_3CN towards 3 positions for which we can use it to derive temperatures.

Two methods were used. First we compared the three CH_3CN spectra with LTE model spectra produced with XCLASS (Schilke et al. 1999), a superset of CLASS of the GILDAS package, obtaining a temperature of $\sim 80 \pm 40\,K$ (see Fig. 2.9). Second, for source 13-s we could also derive a rotational diagram to derive the gas temperature (see e.g., Loren & Mundy 1984; Zhang et al. 1998).

For the rotational diagram, we followed the method outlined in Appendix B of Zhang et al. (1998). Basically, we assume LTE and optically thin emission, then the level populations become directly proportional to the line intensities of the k components and are translated into a single temperature via the Boltzmann equation. With these assumptions, we have the following equation (adapted from Eq. (B6) of Zhang et al. 1998) for the relation between the level populations $N_{J,K}$ and the gas temperature T_{rot}

$$\ln \frac{N_{J,K}}{g_{J,K}} \propto -\frac{E_{J,K}}{k}\frac{1}{T_{rot}} \tag{2.2}$$

where $g_{J,K}$ and k are the statistical weight of the (J, K) level and the boltzmann constant, respectively. Studies by Wilner et al. (1994) show that T_{rot} derived with this formulation agrees with those obtained with LVG calculations.

The level population for the upper K-level can be obtained from the integrated intensity of the corresponding line. The line parameters obtained from the gaussian fit of the spectra shown in Fig. 2.5, and the calculated $N_{J,K}$ for each level are in Table 2.5. The resulting rotational diagram is shown in Fig. 2.10, along with the least-squares fit of all the K components using Eq. (2.2), obtaining the value $T_{rot} \sim 100 \pm 60\,K$. The fit does not represent the physical picture well, which may be related to the assumption of optically thin emission, and could also represent an optically thick, hot and small core with a colder extended envelope.

Despite the crude fit, this value agrees very well with the T_{kin} obtained from thevLVG model and also with the value obtained from the XCLASS model.

Table 2.4: H_2CO line intensities, ratios and LVG temperature of the detected cores.

Source	$H_2CO\,(3_{0,3}-2_{0,2})$ T_b (K)	σ (K)	$H_2CO\,(3_{2,2}-2_{2,1})$ T_b (K)	σ (K)	Ratio	T_{kin} (K)
1-s[a]	...	...	0.4	0.2	...	35
2-s	14.7	0.5	1.7	0.3	8.5	35
3-s	13.6	0.5	1.9	0.4	7.0	35
4-s	17.1	0.8	3.0	0.3	5.8	35
5-s	17.5	0.7	2.7	0.2	6.5	35
6-s	18.0	0.9	1.8	0.4	9.8	35
7-s	18.1	0.7	2.3	0.2	7.8	35
8-s	12.4	0.4	1.8	0.3	7.0	35
9-s	20.5	1.1	2.6	0.5	7.7	35
10-s	18.4	1.3	2.7	0.4	6.8	35
11-s	19.2	0.7	3.0	0.5	6.5	35
12-s	12.8	0.6	2.6	0.4	4.9	45
13-s[b]	14.9	1.0	4.8	0.5	3.1	90
14-s	5.8	0.2	1.7	0.5	3.5	35
15-s	6.5	0.7	1.8	0.0	3.6	35
16-s	3.5	0.2	0.8	0.1	4.2	35
17-s	4.1	0.3	1.8	0.1	2.3	35
18-s	8.4	0.7	3.1	0.0	2.7	35
19-s	8.0	0.6	1.0	0.3	7.9	35
1-n	0.8	0.3	0.2	0.1	3.4	35
2-n	1.4	0.2	0.8	0.0	1.7	35
3-n	1.4	0.1	0.5	0.3	2.9	35
4-n	7.8	0.7	2.7	0.4	2.9	60
5-n	5.4	0.2	1.8	0.3	3.0	50
6-n	6.8	0.2	1.4	0.1	4.9	35
7-n	5.6	0.7	1.4	0.3	4.2	35

[a] No detection in $H_2CO\,(3_{0,3}-2_{0,2})$

[b] Obtained with a 3″ beam to avoid the optically thick regime.

Table 2.5: CH_3CN line parameters and LTE column densities.

Source	Line	$\int T_b\,dv$ (K km s^{-1})	σ	v_c (km s^{-1})	σ	Width (km s^{-1})	σ	T_b (K)	σ	$\log N_k$ (cm^{-2})	σ
13-s	$k = 0$	6.4	1.0	21.3	0.4	6.1	1.1	1.0	0.2	12.1	0.2
	$k = 1$	2.9	0.9	20.0	0.3	3.4	0.9	0.8	0.2	11.8	0.3
	$k = 2$	2.7	0.4	20.2	0.3	4.2	0.7	0.6	0.2	11.8	0.1
	$k = 3$	4.4	0.6	19.8	0.3	6.0	1.2	0.7	0.2	12.1	0.1
6,7,9-s	$k = 0$	2.0	0.2	22.0	0.1	1.6	0.2	1.2	0.1	11.6	0.1
	$k = 1$	1.3	0.2	20.9	0.1	1.3	0.3	0.9	0.1	11.4	0.2
4-n	$k = 0$	2.78	0.02	21.4	0.4	4.1	0.8	0.6	0.1	11.77	0.01
	$k = 1$	1.71	0.01	20.3	0.3	2.6	0.7	0.6	0.1	11.57	0.01

2.3.2 The Differential Core Mass Function

Combining the data from both (proto)clusters we derive a differential CMF $\Delta N/\Delta M$, with the number of cores ΔN per mass bin ΔM.

The strongest caveat we faced when deriving the CMF was the relatively low number of cores detected. Because of that, a continuous linear binning in mass was not possible. Instead, we performed a logarithmic binning to better represent and analyze the data, meaning that the fixed-width mass bins are defined on a logarithmic axis,

$$\Delta M = \log M_k - \log M_{k-1} = B \tag{2.3}$$

where B is the constant bin width. Therefore, the k-th mass is defined as $M_k = 10^{kB}$. This binning scheme is further discussed in e.g., Maíz Apellániz & Úbeda (2005) and Rosolowsky (2005).

A priori we do not have a preferred value for B, thus we derive a mass spectrum for different bin widths, with B ranging from 0.001 to 1 in 0.001 steps. Not all the CMFs obtained with this method were fitted. To obtain meaningful results, we established the following criteria to be satisfied for a CMF to be fitted:

- At most only one bin may contain a single core.
- There must be at least four non-empty bins after the incompleteness threshold.

We fit a power-law of the form $\Delta N/\Delta M \propto M^{\beta}$ to the CMFs satisfying those two criteria, obtaining a β_B index value corresponding to a given B. The final value β is the weigthed mean of all the β_B indices with $\sigma \leq 0.4$ and coefficient of correlation[2], $r^2 \geq 0.9$. The different values of the power-law indices β_B satisfying these consitions are plotted in Fig. 2.11 as a function of the bin width B. The resulting weighted average and its formal error $\beta = -2.3 \pm 0.2$ are also marked. Some "local trends" can be seen in Fig. 2.11, for example between $B = 0.215$ and $B = 0.238$. That happens because of the method used to define the mass bins. For some values of B, the change in the bins' extrema is not enough to produce a change in ΔN for any of the ΔM intervals. The histogram, and therefore the fit of the resulting mass distribution changes only because (the arbitrary) ΔM change, i.e., this effect is artificial and gives us an estimation of the uncertainity in the fit of the mass distribution.

Aside from these "local trends" there is also an overall trend seen between β_B and B. This trend is again an effect of the binning method, but also of the shape of the mass distribution itself. In a similar way as before, with increasing B the ΔM intervals become larger, but because there is a finite number of data points (cores) the differential CMF starts to be contained in fewer ΔM intervals each time until the whole mass range is covered by 3 or fewer mass bins. This steepens the distribution until there is only one mass bin containing all the data points. Despite this, we see that the β_B values are consistently steeper than $\beta \sim -2$.

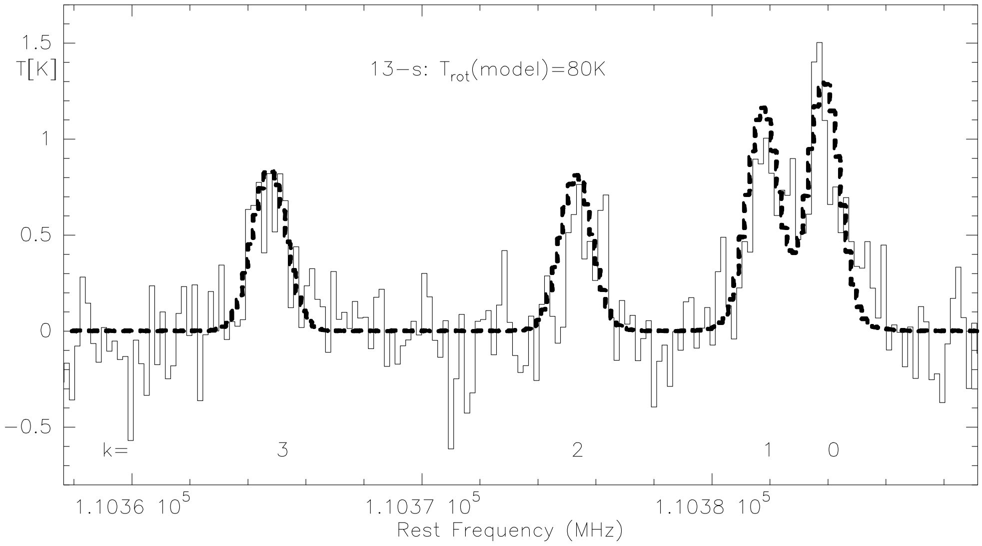

Figure 2.9: XCLASS (dashed line) fit to the observed CH_3CN spectrum towards source 13-s.

---

[2] This coefficient is defined as $r^2 = 1 - \frac{SS_{err}}{SS_{tot}}$, where SS_{err} is the sum of squared errors or residual sum of squares, and SS_{tot} is the total sum of squares. By this definition r^2 ranges between 0 and 1. A value of 1 means a perfect fit to the data (e.g, Draper 1998).

We see then that our results for the CMF slope are steeper than the ~ -1.6 found for the Clump Mass Functions (e.g. Kramer et al. 1998; Kerton et al. 2001; Muñoz et al. 2007), obtained with CO emission maps for structures of sizes on the order of ~ 0.1 pc. Going to at least one order of magnitude better in spatial resolution, we find that the slope of the Mass Function is consistently steeper, signaling further fragmentation at smaller spatial scales.

For reference, Fig. 2.12 shows an example of the CMFs we obtained in this case corresponding to $B = 0.214$ and having a power-law index $\beta = 2.3 \pm 0.2$. A turnover in the distribution at the bin centered at $\sim 1.4\,\mathrm{M}_\odot$can be seen, containing masses above $\sim 1\,\mathrm{M}_\odot$. It appears in all the derived CMFs at about the same position, and since it matches our detection threshold, we assume that it is likely caused by the low-mass incompleteness of our sample rather than being a physical feature. In all of the cases, we fit our mass distributions for masses higher than the turnover.

The Cumulative Mass Function

Using the differential CMF in a low-number sample has the disadvantage that it is sensitive to the arbitrariness of binning, as we have shown in the previous section and led to the analysis described there. On the other hand, a cumulative CMF is free from any problems associated with the binning, and is more suitable for low-number samples, as in our case.

With our treatment of the CMF described in the previous section, we have taken into account the arbitrainess of the binning. However, for comparison and further analysis we also derived a cumulative CMF for our sample. Since our differential CMF above $\sim 1\,\mathrm{M}_\odot$ can be fit by a single power-law of the form

$$\frac{\Delta N}{\Delta M} \propto M^{\beta} \tag{2.4}$$

then the cumulative CMF is

$$N(>M) \propto -\frac{1}{1+\beta} M^{1+\beta} \tag{2.5}$$

for $\beta < -1$. According to Reid & Wilson (2006), when using the cumulative CMF one should take into account the upper mass cutoff M_{max} of the sample, whether it is a real cutoff or a result of the finite sampling. In that case, the cumulative CMF takes the form

$$N(>M) \propto \begin{cases} \frac{1}{1+\beta}\left(M_{max}^{1+\beta} - M^{1+\beta}\right), & M < M_{max} \\ 0, & M \geq M_{max} \end{cases} \tag{2.6}$$

for $\beta < -1$. However, they also state that a “steep power law” ($\beta = -2.5$) will overwhelm the effect that the upper mass cutoff introduces in the fitting. From the differential CMF we see that

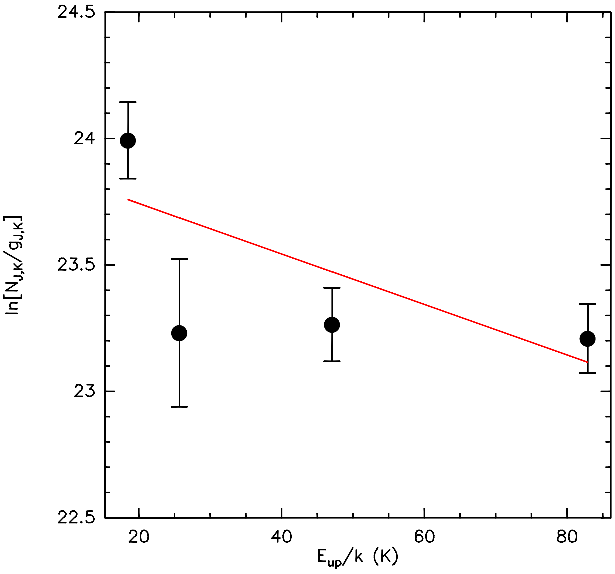

Figure 2.10: Rotational diagram of the observed K-levels of $CH_3CN(J = 6 \rightarrow 5)$ towards source 13-s. The solid line is the best fit of Eq. 2.2, corresponding to a rotational temperature 100 ± 60 K, in agreement with the kinetic temperature obtained with the LVG modeling of the H_2CO line emission.

we are close to that "steep power law" limit, so we adopt both analytical forms given in Eqs. (2.5) and (2.6) for the cumulative CMF.

Fig. 2.13 shows the cumulative CMF for masses above $1\,M_\odot$. As stated before we fit both the analytical expressions given in Eqs. (2.5) and (2.6). The results are $\beta = -2.4 \pm 0.1$ and $\beta = -2.2 \pm 0.1$, respectively, with the σ values resulting from the fitting algorithm. These results are comparable, showing that for a steep power law the inclusion of M_{max} in the definition of the cumulative CMF does not affect the result significantly (Reid & Wilson 2006). Since both results are similar, we adopt their average value $\beta = -2.3 \pm 0.2$.

The cumulative CMF shows that the lower-mass objects dominate the fit. This is already visible in the differential CMF, but is clearer in the cumulative CMF. This is because the lower-mass bins are more populated. We see that of the 25 cores with masses above $1\,M_\odot$only 6 are more massive than $2.5\,M_\odot$, therefore the lower-mass bins have more statistical weight in the fitting.

There is also a noticeable is a "bump" in the distribution starting at $\sim 4\,M_\odot$. It is not clear if it is a real physical feature of the distribution or a product of the uncertainty of its derivation. We discuss this in further detail in Sec. 2.4.3.

2.4 Discussion

2.4.1 Continuum Sources

Beuther & Schilke (2004) detected 24 millimetric sources at 1.3 mm, 12 in each northern and southern cluster, with a detection threshold of $3\sigma \sim 9\,\mathrm{mJy\,beam^{-1}}$. Having better sensitivity, we adopted a detection thershold of $4\sigma \sim 4\,\mathrm{mJy\,beam^{-1}}$ at 1.4 mm finding 26 cores, 19 in the Southern cluster and 7 in the Northern (proto)cluster. Despite the slight difference in the total number, the general 1.4 mm high-resolution cluster structure shown in Beuther & Schilke (2004) is recovered. The differences also highlight the general mapping difficulties with interferometers having only a small number of elements close to the detection limit. For example, contrary to expectations, formal 3σ limits in such maps are not as reliable as one may expect. Therefore, here we raised the threshold to 4σ. ALMA, with its many antennas, will overcome such problems.

In the Southern (proto)cluster, there are NIR and MIR counterparts detected for several of our mm sources. Martín-Hernández et al. (2008) and Qiu et al. (2008) detect in the position of 13-s a bright source in the K_s filter and the $3.6\mu m$, $4.5\mu m$, $5.8\mu m$ and $8.0\mu m$ Spitzer/IRAC bands. Martín-Hernández et al. (2008) suggest that the detected NIR and MIR emission is either leaking through an outflow-created cavity (see Beuther et al. 2003), or that the cavity itself is radiating the emission, based on their estimation that the visual extinction at that position should be very large and thus should not have any detectable NIR or even MIR emission. We confirm their estimation, finding that the visual extinction for 13-s is $A_v \sim 2700$ (see Table 2.2). Source 13-s is in an early stage of evolution, according to its NIR excess and the presence of H_2O and Class II CH_3OH masers (Beuther et al. 2002d), however the detection of a VLA 3.6 cm source at its position (Sridharan et al. 2002), suggest the presence of a recently ignited protostar that has already formed an Ultracompact or Hypercompact HII region, the detected radio emission being consistent with an ionizing B2 V star (Martín-Hernández et al. 2008; Qiu et al. 2008; Panagia 1973).

In Fig. 2 of Martín-Hernández et al. (2008), MIR emission is also seen at the position of the "subcluster" centered in sources 6-s, 7-s and 9-s (source mm2 in their work and in Beuther et al. 2003). There is no detected cm counterpart at that position, suggesting that either none of the sources have ignited or the ionized HII region is still too small so the free-free emission is confined and not detectable. Therefore these sources might be at an even earlier stage of evolution as 13-s, the equivalent of a Class 0 low-mass protostar, heating their circumstellar dust enough to be detected at MIR wavelenghts.

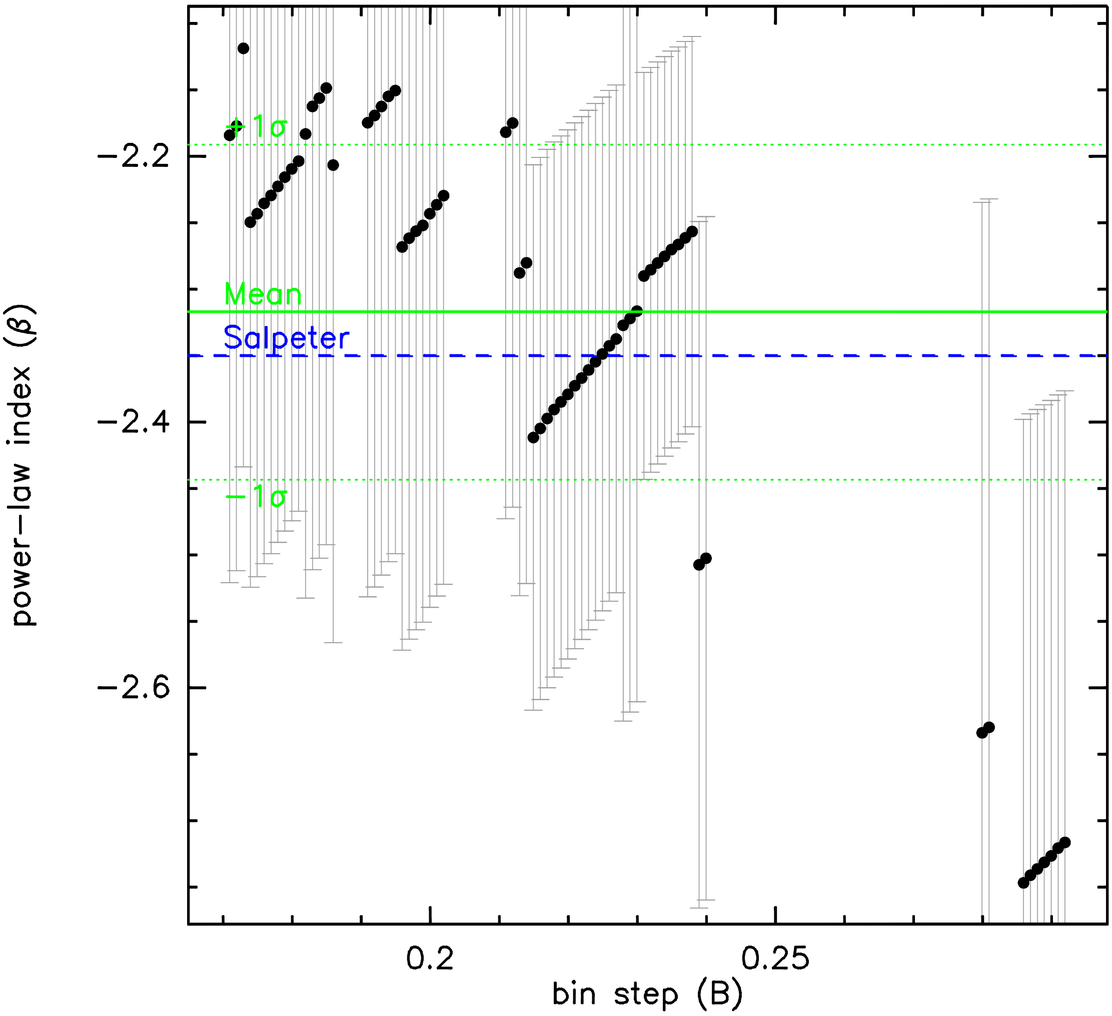

Figure 2.11: Obtained power-law index β for the different binnings B. Marked are the Salpeter value for the stellar IMF (blue dashed line) and the average β value obtained (green solid line) and its $\pm\sigma$ interval (green dotted lines).

Source nr76 of Martín-Hernández et al. (2008) is located less than 1.5" from source 1-s. However, nr76 is detected in the J, H and K_s bands and not in any of the Spitzer bands, while 1-s is marginally detected at 1.4 mm and is resolved at 3 mm. The lack of emission in the Spitzer bands while being well detected in the K_s band, and the fact that is a relatively strong source at 3 mm, make us believe that nr76 is not the counterpart of 1-s, but a separate source, appearing nearby due to a projection effect. The case is similar also for source nr71. It is located at $\sim 1.5''$ from 20-s, and although nr71 shows strong MIR emission, we only detect source 20-s at 3 mm and not at 1.4 mm. Therefore we believe that this is also a case of spatial projection.

This can be expected, since IRAS 19410+2336 is embedded in a cluster of Young Stellar Objects (YSOs). Martín-Hernández et al. (2008) detects 116 NIR/MIR sources in a $\sim 75'' \times 75''$ region

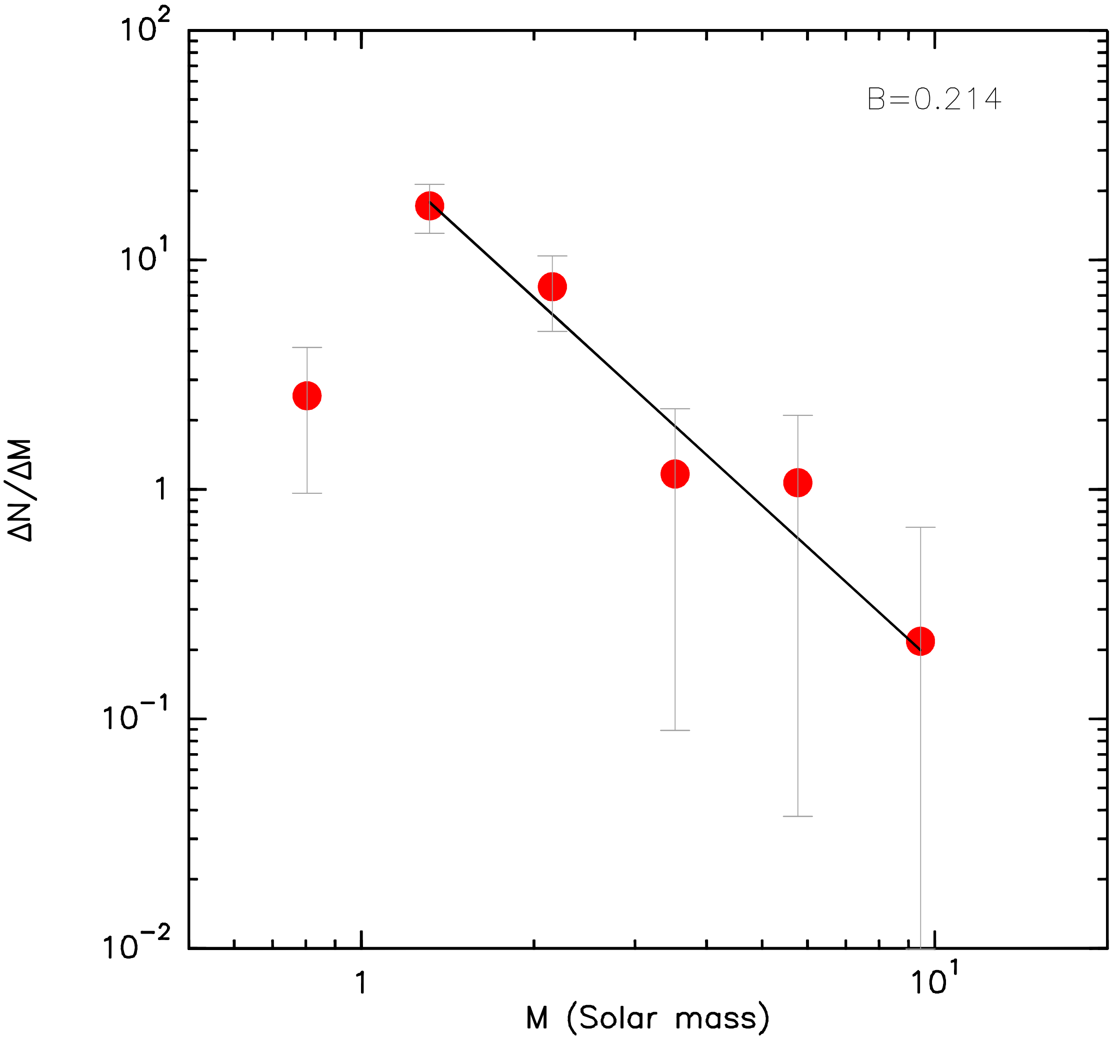

Figure 2.12: Example of the obtained CMFs, corresponding to $B = 0.214$, for core masses above 1.4 $M_\odot$. The solid line is the best fit of Eq. (2.4), with a power-law index $\beta = -2.3 \pm 0.2$.

centered on IRAS 19410+2336, while Qiu et al. (2008) detect 46 YSOs ranging from Class 0 to Class II protostars within a radius of ~ 2 pc, in addition to the detection of over 800 NIR sources in that region. The fact that there are already low-mass stars in the outskirts of IRAS 19410+2336 while high-mass stars are still forming in it supports the hypothesis that the low-mass stars form before their high-mass counterparts (e.g., Kumar et al. 2006).

Also in the Northern (proto)cluster there are identified NIR and MIR counterparts. Qiu et al. (2008) found 5-band Spitzer/IRAC and 2MASS H and K_s emission towards 4-n, as well as Spitzer/IRAC 3.6μm, 4.5μm, 5.8μm and 8.0μm emission towards 1/2/3-n. Source 4-n is likely at an early stage of evolution, however it is likely the most evolved source in the Northern (proto)cluster. It is not detected at cm wavelenghts, therefore it has either not yet ignited its protostar or the ionized region is still too small and the free-free emission is trapped and thus not yet detectable. The other NIR/MIR detection in the (proto)cluster is towards sources 1/2/3-n, and their NIR/MIR flux is lower than that of 4-n, while their respective 1.4 mm masses are similar. This would indicate that 4-n is in a more advanced evolutionary stage than 1/2/3-n.

With $L \sim 10^4\,L_\odot$, IRAS 19410+2336 is a high-mass star-forming region, but the (proto)stellar content in its core is unknown because of high obscuration. Since it shows cm emission, most likely it already has a (proto)stellar component, ionizing an Ultra- or even a Hypercompact Hɪɪ region. While it is not possible to directly measure the masses of the (proto)stars with millimeter data, it is possible to derive the masses of the circumstellar structure. The low masses that we calculate from the 1.4 mm data can be attributed to a circumstellar structure, while the surrounding envelope likely contributes to the larger masses derived from the 3 mm data. However, we must take into account the "short-spacing problem" when interpreting the calculated masses of the continuum sources. This caveat, inherent to interferometers, means that a high percentage of the flux is filtered out and lost. This effect is more severe in the extended configurations (long baselines), as in our case.

Single-dish continuum observations of IRAS 19410+2336 at 1.2 mm with the IRAM 30m Telescope indicate an integrated flux density[3] $S_{1.2\,\mathrm{mm}} \sim 6.3$ Jy for the southern (proto)cluster (Beuther et al. 2002b). Considering a dependence $S_\nu \propto \nu^4$, that value corresponds to $S_{1.4\,\mathrm{mm}} \sim 3.8$ Jy, and $S_{3\,\mathrm{mm}} \sim 240$ mJy. In our 1.4 mm continuum map of the southern (proto)cluster, the average flux density recovered within the PdBI primary beam is $S_{1.4\,\mathrm{mm}} \sim 210$ mJy, meaning that ~ 94% of the flux is lost. Therefore the calculated masses at 1.4 mm are actually a lower limit for the current mass of each source. On the other hand, at 3 mm we recover $S_{3\,\mathrm{mm}} \sim 85$ mJy within the PdBI primary beam, therefore we are losing ~ 63% of the flux. This shows how there is still a large fraction of the emission emitted by extended structures, that we are filtering out. Nevertheless, at 3 mm the obtained values for the masses are more representative of the mass of their envelopes.

The different percentage of flux filtered out in each wavelength band can be explained in the same way as the large (up to a factor ~ 10) difference between the calculated masses at 1.4 mm and 3 mm. As discussed previously (see Sec. 2.2.1), varying dust properties can account for this difference, however the interferometer flux filtering is likely the main reason. Both wavelengths were observed at the same time with the same interferometer configurations meaning that although the ground baselines are the same, the uv coverage measured in units of wavelength (kλ) at 3 mm is more compact than at 1.4 mm, therefore tracing more extended components in the region.

---

[3] Although bolometers have broad bandwidth, MAMBO has a bandwith of ~ 80 GHz centered at $\nu_{eff} \sim 240$ GHz, therefore we assume this as the flux at 1.2 mm.

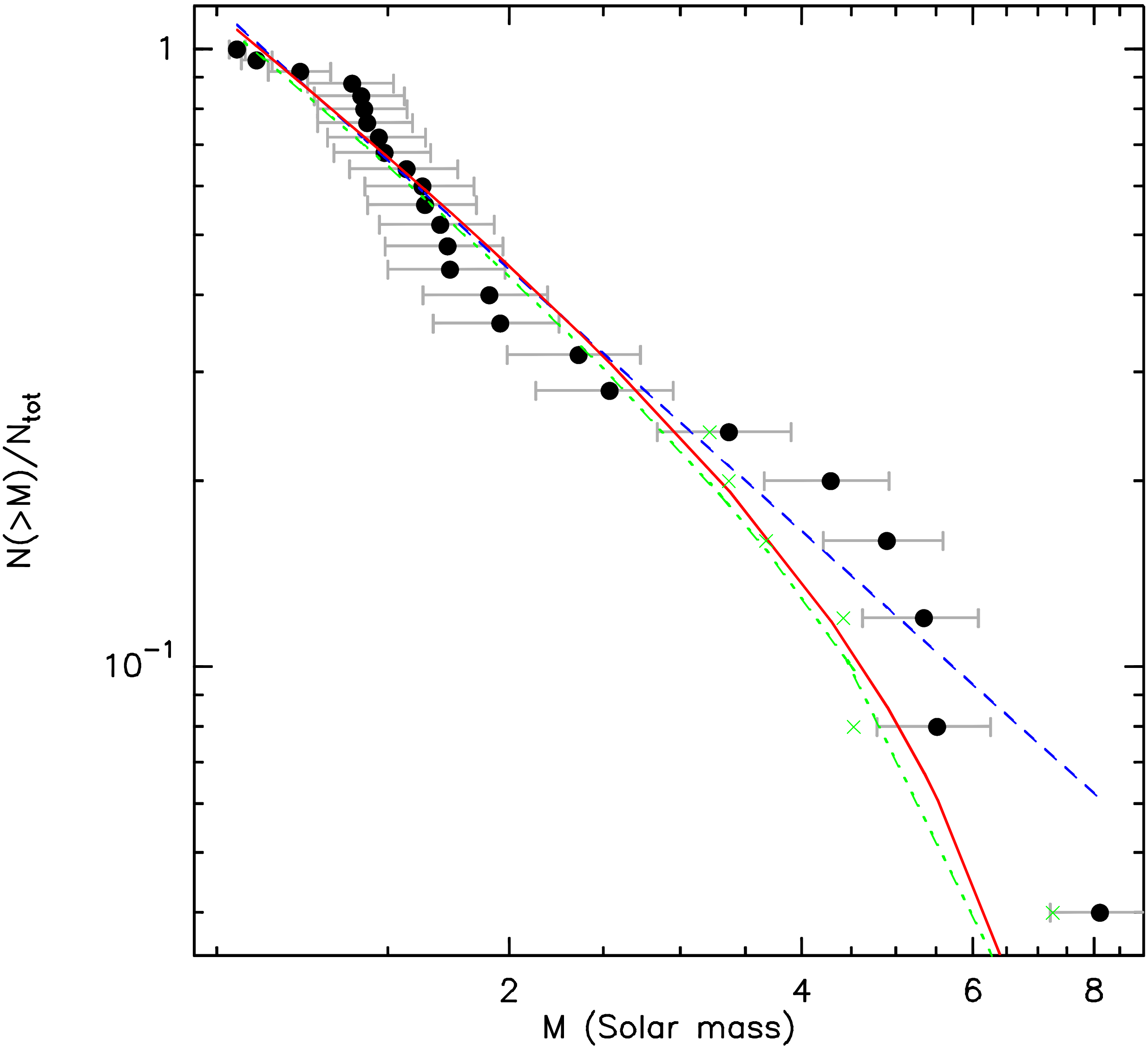

Figure 2.13: Cumulative CMF of IRAS 19410+2336 for core masses above 1 $M_\odot$. The solid red line and the dashed blue line represent the best fit of Eqs. (2.6) with a power-law index $\beta = -2.2 \pm 0.1$ and (2.5) with $\beta = -2.4 \pm 0.1$, respectively. The green crosses represent a slight increase of 10 K in the higher-mass end, and the green dash-dotted line is the new fit of Eq. (2.6) (see Sec. 2.3.2). Notice the flattening of the "bump" in the distribution, while the slope of the fit practically does not change. Note that we have normalized $N(> M)$ by the total number of cores N_{tot}.

2.4.2 Virial and Jeans analysis

The large uncertainity that the flux filtering introduces in the mass calculations can be seen when comparing the gas masses with the virial masses. The former are calculated from the interferometric continuum emission that is affected by the flux filtering, while the latter are calculated using the combined interferometric and single-dish H_2CO data, with the short-spacings correcting the effect introduced by the flux filtering. The virial and gas masses for the resolved cores in IRAS 19410+2336are compared in Fig. 2.14. At first glance, the cores do not appear to be collapsing, however the gas masses derived from the continuum are lower than the virial masses because of the missing flux discussed previously. If we shift the gas masses higher by a factor of 2, taking into account only $\sim$ 10% of the missing flux, we see that within the uncertainty on the virial masses now all the resolved cores are likely collapsing.

The relative distances between neighboring cores within each (proto)cluster range several thousands of AU. These are similar and below the (proto)cluster's Jeans length $\lambda_J \sim 25000\,\mathrm{AU}$, calculated from the equation

$$\lambda_J = 0.19\,\mathrm{pc}\left(\frac{\mathrm{T}}{10\mathrm{K}}\right)^{1/2}\left(\frac{\mathrm{n_{H_2}}}{10^4\,\mathrm{cm^{-3}}}\right)^{-1/2} \tag{2.7}$$

for an average $\mathrm{n_{H_2}} \sim 10^5\,\mathrm{cm^{-3}}$ and an average $\mathrm{T_{kin}} \sim 40\,\mathrm{K}$ (see Sec. 2.3.1; Stahler & Palla 2005). Our resolution of $\sim 1''$ at 1.4 mm corresponds to a spatial scale of $\sim$ 2200 AU, which clearly resolves the Jeans length of the region. We are thus resolving the fragmentation of the clump-scale (proto)clusters far below their Jeans length. This cannot be said in the case of the cores, for which our resolution is above the Jeans length of the individual cores, in the 700 – 1200 AU range.

We are resolving the Jeans length of the clumps by one order of magnitude, almost reaching the Jeans length of the individual cores, therefore we can safely assume that we are mapping the direct progenitors of single stars or multiple systems at most (similar to the Trapezium in Orion, see e.g., Rodón et al. 2008), and from the H_2CO data, we see that there is only a small signature of velocity dispersion (see Fig. 2.4), which would imply that the (proto)clusters are in a stage of weak dynamical evolution.

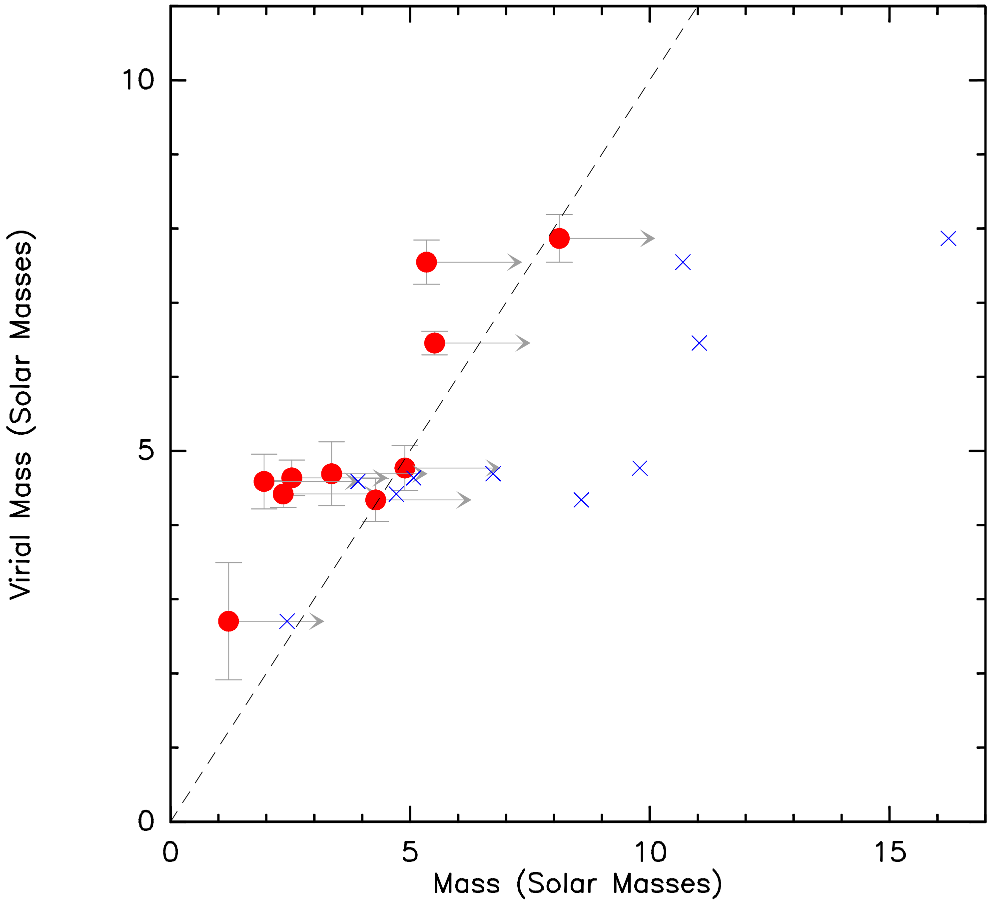

Figure 2.14: Comparison between the virial masses and gas masses of the resolved cores in IRAS 19410+2336. Virial masses are not affected by the interferometric flux filtering, which do affect the gas masses. The red dots are the actual values obtained, while the blue crosses represent the relationship if we take into account ∼ 10% of the flux filtered by the interferometer. This is a hint of the care that has to be taken when interpreting interferometric flux values.

2.4.3 The Core Mass Function of IRAS 19410+2336

From the analysis described in Sec. 2.3.2, we obtain a power-law differential CMF for IRAS 19410+2336 with an index $\beta = -2.3 \pm 0.2$, in agreement with the Salpeter value of $\beta = -2.35$ for the stellar IMF.

This result is also in agreement with the previous result of Beuther & Schilke (2004). However the new result is much more reliable as the previous one because we estimated a temperature structure for the (proto)clusters, thus getting a more accurate value for the core masses, avoiding the previous caveat of assigning a uniform temperature. The calculation of the power-law index was done taking into account the arbitrariness of the binning at the moment of deriving a differential CMF. Also, the cumulative CMF was taken into account in the analysis.

In the case of the cumulative CMF, the result obtained from it matches the result from the differential CMF. Although the cumulative CMF is better suited than the differential CMF for the analysis of a low-number sample, in this case we observe that the fit to the cumulative CMF represents the lower-mass end of the distribution well but not the higher-mass end. However, a slight 10 K increase in temperature in the higher-mass end flattens the “bump” seen starting at $\sim 4\,M_{\odot}$, obtaining also a better fitting for the distribution while not introducing substantial modifications to the fitted parameters. It should be noted that a 10 K difference is within the uncertainity in the temperature determination. Therefore is not certain whether the “bump” seen in the cumulative CMF is real or is just a product of the uncertainity in the temperature determination.

Observations of low-mass star-forming regions suggest that the IMF of low-mass stars is determined at early evolutionary stages (e.g., Testi & Sargent 1998; Motte et al. 1998, 2001; Alves et al. 2007; see varying suggestions e.g., Goodwin & Kouwenhoven 2009). This is not so clear in the case of MSF regions because dynamical processes like competitive accretion and merging of less massive protostars can shape the IMF at later evolutionary stages (e.g., Bonnell et al. 2004, 2007; Bonnell & Bate 2006).

Nevertheless, sinlge-dish sub-mm observations of MSF regions find that the shape of the CMF resembles the IMF (Johnstone et al. 2000, 2006; Nutter & Ward-Thompson 2007). We find that is the case also at higher-spatial resolution in massive star-forming regions, resolving collapsing structures on the order of $\sim$ 2200 AU.

The similarity found between the CMF and the IMF suggests that the structure and conditions within the molecular cloud determine the IMF. This would be the case if the relationship between the cores and the stars forming from them is one-to-one or nearly one-to-one. This kind of relationship is supported by theoretical models explaining the shape of the high-mass end of the IMF (e.g., Scalo et al. 1998; Padoan & Nordlund 2002), and by the apparently constant star formation efficiency suggested both by theory and observations (Matzner & McKee 2000; Alves et al. 2007).

Also, in the Clark et al. (2008) picture of competitive accretion, the shape of the IMF is independent of when competitive accretion is halted. This would suggest that the IMF is set early on in the evolution of the clump, and therefore having non-pre-stellar cores at the moment of deriving a CMF would not affect the final results, as in our case.

Our derived power-law index β could then be compared with the IMF. This would suggest that the IMF is indeed determined at the earliest stages of the cluster formation, providing support for the early fragmentation and disk-accretion scenario for the formation of stars of all masses.

However, caution must be taken when doing a direct comparison between the CMF and the IMF. Numerical simulations show that although the overall shape of the IMF in the low-mass to intermediate-mass regime is robust against different core evolution scenarios, further turbulent fragmentation of the cores may change the high-mass slope of the IMF (Swift & Williams 2008). The latter is hinted at in our data. The high-mass "bump" seen in the cumulative CMF can also be smoothed if further fragmentation of the cores take place, although we find that the power-law index does not vary significantly, given our degree of uncertainity in the calculations.

Remarkably, IRAS 19410+2336 is so far the only known high-mass star-forming region that shows more than 10 cores when resolved down to a spatial scale of several thousand AU. Similar high-spatial resolution (sub)mm observations of MSF regions resolve only a few cores. As an example, interferometric PdBI and SMA mm mappings of the MSF regions W3 IRS 5, IRAS 06058+2138, IRAS 06061+2151, IRAS 05345+3157 and AFGL961 resolve cores down to spatial scales between ~ 750 and ~ 5000 AU, recovering in all cases fewer than 10 cores in each region (Fontani et al. 2009; Williams et al. 2009; Rodón et al. 2008, 2009 *in preparation*). These regions are similar in distance and luminosity to IRAS 19410+2336, and although the gas mass varies, even the regions more massive than IRAS 19410+2336 show much less fragmentation at similar spatial scales.

In most cases, the PdBI has ~ 20% better sensitivity than the SMA, therefore lower mass sources can be detected with the PdBI that might escape detection with the SMA. Therefore the lack of detections of lower mass sources may be an observational artifact when using the SMA. However when using the PdBI the sensitivity levels are similar in all cases, and this lack of detections may indicate that the CMF in those regions are more "top-heavy", meaning then that they are intrinsically different from IRAS 19410+2336.

It is unclear where this apparent uniqueness of IRAS 19410+2336 comes from. It could be an effect of being at a different evolutionary stage, having a different chemical composition or even through perturbation and/or a different formation processes. Whichever the case, this apparent lack of fragmentation is preventing the derivation of a CMF for other individual MSF regions, highlighting the uniqueness of IRAS 19410+2336.

2.5 Conclusions

We resolve the two clumps of the MSF region IRAS 19410+2336 into 26 cores at 1.4 mm, with a spatial resolution of ~ 2200 AU. This resolves the Jeans length of the clumps, and the relative distances between the cores are similar or smaller than the Jeans length corresponding to individual cores. Also, the cores show only a marginal signature of velocity dispersion, implying that the (proto)clusters are not in a strong dynamical evolution.

The temperature structure of IRAS 19410+2336 was determined from its H_2CO and CH_3CN emission allowing the derivation of a reliable CMF. Taking into account the arbitrariness of the mass binning when deriving a mass function, we found a CMF index $\beta = -2.3 \pm 0.2$ for core masses above $\sim 1.4\,M_\odot$, consistent with Salpeter, and confirming the previous results of Beuther & Schilke (2004) with significantly increased confidence levels.

This similarity between the CMF and the IMF would imply that the latter is determined already at the early stages of fragmentation of the molecular cloud, supporting the early fragmentation and disk-accretion scenario for the formation of stars of all masses. However, we also discuss the caveats of this assessment.

Chapter 3

Fragmentation in the outer Galaxy

The results of the previous chapter on IRAS 19410+2336 gave indications for a Core Mass Function (CMF) similar to the stellar Initial Mass Function (IMF) which suggests that fragmentation of the initial massive cores may determine the stellar IMF. However, the sample of resolved fragmenting massive star-forming clumps has to be increased significantly to understand the fragmentation processes in a more general way and to reach solid conclusions.

Observationally, at the low-mass end a series of (sub)mm continuum studies have revealed that the low-mass core function resembles the IMF (e.g., Motte et al. 1998; Johnstone et al. 2001). These results indicate that at least at the low-mass end the IMF is really determined at the early evolutionary fragmentation stages. Bonnell and collaborators caution that it has not yet been conclusively shown that all cores in these studies are really bound, and they may be transient structures. Although this is not likely for the dense gas traced by the (sub)mm continuum, as for instance Belloche et al. (2001) have shown in the case of ρ Ophiuchi.

Even more problematic is the picture for the high-mass end of the CMF because of the clustered mode of massive star formation and the difficulty to resolve enough Massive Star-Forming (MSF) regions reasonably well at the given large distances. Single-dish studies of samples of high-mass star-forming regions at early evolutionary stages have shown that at high clump[1] masses, the cumulative mass distributions are consistent with the the slope of the high-mass stellar IMF (e.g., Williams et al. 2004; Reid & Wilson 2005; Beltrán et al. 2006). However, one has to keep in mind that these single-dish studies are sampling cluster-forming scales and hence rather resemble final cluster mass functions.

Furthermore, one has to study regions in different —albeit young— evolutionary stages in detail to discriminate whether the fragmentation processes may be different for differently sized original gas cores. Aside certain molecular tracers as DCN and methanol, to determine the rel-

---

[1] We keep the convention set in Chapter 2, and will refer to “core” as the small (diameter D~ 0.01 pc), dense condensation that will form individual stars or small multiple systems, while with “clump” we denote structures that may form (proto)clusters and may therefore be more massive and larger than cores.

ative age of a MSF region one can also take a multiwavelength (multi-λ) approach in response to the large range of densities the MSF regions are enshrouded by. For example, in an evolutionary sense MSF regions start as High-Mass Starless Cores and go through different evolutionary stages of the newborn protostar until they become Final Stars emerging from the parental cloud and dispersing them in this process (Beuther et al. 2006). The different stages are observationally distinguishable via the wavelengths in which they are detectable, ranging from radio to the near-infrared (NIR). Some of these evolutionary stages often occur simultaneously within an individual region.

A complete inventory of the high-mass stellar content in a region requires the coverage of the different evolutionary stages therein. In the NIR we trace the photospheric component of the more evolved protostars, while with (sub)mm interferometry we can observe the deeply embedded dust component of the younger protostars at a comparable spatial resolution, and both stages have already been seen occurring simultaneously (e.g, Kumar et al. 2006; Qiu et al. 2008).

Going in this direction we selected a sample of relatively close MSF regions at ~2 kpc as well as being suggested to be of different ages (e.g., Ghosh et al. 2000). The sample consist of the MSF regions IRAS 06056+2131, IRAS 06058+2138, IRAS 06061+2151 and IRAS 06063+2040. These regions have been previously mapped at (sub)mm wavelengths with single-dish telescopes by Klein et al. (2005), with their best beam size of about 14″, thus only mapping the large scale dust structures. Nevertheless, they already show fragmentation of the cores in an arc-minute scale.

Also, the regions in our sample have been observed within the framework of the project Formation and Early Evolution of Massive Stars (FEMS, P.I.: A. Bik). The project is aimed to classify the stellar content and derive the distribution of OB stars, massive young stellar objects (YSOs) and the lower-mass pre-main sequence stars, as well as derive the stellar parameters of OB stars by fitting stellar atmospheric models. In the observational side, FEMS comprises observations with the SINFONI integral field spectrograph at the VLT (see Puga et al. 2008), covering the spectral range from 1.5 to 2.4 μm and obtaining NIR K-band continuum data and in particular the [FeII], H_2 and Br_γ spectra.

3.1 The Sample

3.1.1 IRAS 06056+2131

This region, adjacent to the S247 Hɪɪ region, is closely related to the IRAS 06058+2138 region, and comprises two sites of massive star formation. Each one contains a bright IRAS source and they are connected by a bridge of material seen at 850 μm (see Fig. 3.1). Multiline, molecular line and NIR studies, together with detailed FIR studies characterizes this region as an active star forming region (Carpenter et al. 1995a,b; Ghosh et al. 2000). The presence of molecular outflows and H_2O and $CH_3OH\,(4_{2,2} - 3_{1,2})$ maser emission (Xu et al. 2006) indicates that the (sub)mm continuum peaks may contain a very young protostellar object. Klein et al. (2005) already detect indications of substructures in their single-dish large-scale maps. Its estimated distance and luminosity are 2.0 kpc and $10^{4.3}$ $L_\odot$, respectively (Klein et al. 2005).

3.1.2 IRAS 06058+2138

This region is part of a sample of young high-mass star-forming regions in the outer Galaxy first compiled by Henning et al. (1992) and studied in detail later by Schreyer et al. (1996) and Klein et al. (2005). Especially the (sub)mm continuum mapping study by Klein et al. (2005) revealed a strong and peaked (sub)mm continuum source approximately 10″ offset from any near-/mid-infrared emission (see Fig. 1 in Klein et al. 2005). Hence Klein et al. (2005) classified this region as a "pre-protocluster" candidate. The elongation of the submm single-dish core and the presence of a nearby near-/mid-infrared cluster are indicative of substructure and fragmentation at smaller angular scales. Since the whole region is known to drive a molecular outflow and H_2O and $CH_3OH\,(4_{2,2} - 3_{1,2})$ maser emission (e.g., Wu et al. 2004; Henning et al. 1992; Szymczak et al. 2000), the (sub)mm continuum peak may contain already a very young embedded source of protostellar nature. Nevertheless, the non-detections in the near- and mid-infrared bands definitely classify this source as being in the earliest evolutionary stages of high-mass star formation. Its estimated distance and luminosity are 2.0 kpc and 10^4 $L_\odot$, respectively (Klein et al. 2005).

3.1.3 IRAS 06061+2151

Within this region lies one of the brightest IRAS sources surrounding S247, however the mm continuum peak detected is slightly westwards of it, which indicates the possible presence of a deeply embedded protostar. IRAS 06061+2151, together with IRAS 06056+2131 and IRAS 06058+2138, are surrounding the S247 Hɪɪ, part of the Gemini OB1 molecular complex (see e.g., Carpenter et al. 1995a). Anandarao et al. (2004) have detected H_2 emission knots in the region, indicating a jet. This will be corroborated with the SINFONI survey. The slightly southward elongated mm core emission may indicate substructure at smaller angular scales. Its estimated distance and luminosity are 2.0 kpc and 10^4 $L_\odot$, respectively (Klein et al. 2005).

3.1.4 IRAS 06063+2040

This region is associated with the ultracompact Hɪɪ region S252-C. The detected extended mm emission covers a NIR cluster, and a radio and a bright NIR object coincide with the IRAS source (Klein et al. 2005). The clearly elongated shape of the single-dish mm emission and the presence of a NIR cluster are strong indicators of substructure and fragmentation at small angular scales. Its estimated distance and luminosity are 2.0 kpc and $10^{4.1}$ $L_\odot$, respectively (Klein et al. 2005).

3.2 Observations

We observed the four MSF regions IRAS 06056+2131, IRAS 06058+2138, IRAS 06061+2151, and IRAS 06063+2040 with the SMA in the *compact*, *compact-north* and *extended* configurations. IRAS 06058+2138 was observed during the Winter 2006/2007 semester, the other three sources were observed during the Winter 2007/2008 semester. In all cases the baselines ranged from ~ 16 m to ~ 230 m, that translate into projected baselines from ~ 11 $k\lambda$ to ~ 161 $k\lambda$. Sources IRAS 06061+2151 and IRAS 06063+2040 were observed in the track-sharing mode, as well as the two pointings (North and South) on source IRAS 06056+2131 (see Table 3.1).

Table 3.1: SMA pointings and configurations.

Region	R.A. (J2000)	Dec (J2000)	L_{IRAS} ($\log L_\odot$)	V_{lsr} ($\mathrm{km\,s^{-1}}$)	Conf.[a]	Obs. Dates yy-mm-dd
IRAS 06056+2131-N	06:08:46.2	21:31:48.2	4.3	2.5	C-N,E	07-12-27 & 08-01-13
IRAS 06056+2131-S	06:08:40.3	21:31:04.0	4.3	2.5	C-N,E	
IRAS 06058+2138	06:08:53.0	21:38:08.7	4.0	3.2	C,E	06-11-29 & 07-02-25
IRAS 06061+2151	06:09:06.5	21:50:36.8	4.0	-0.9	C,E	08-01-27 & 08-03-05
IRAS 06063+2040	06:09:21.3	20:38:45.6	4.1	8.9	C,E	

[a] SMA configurations: C → compact, C-N → compact-north, E → extended.

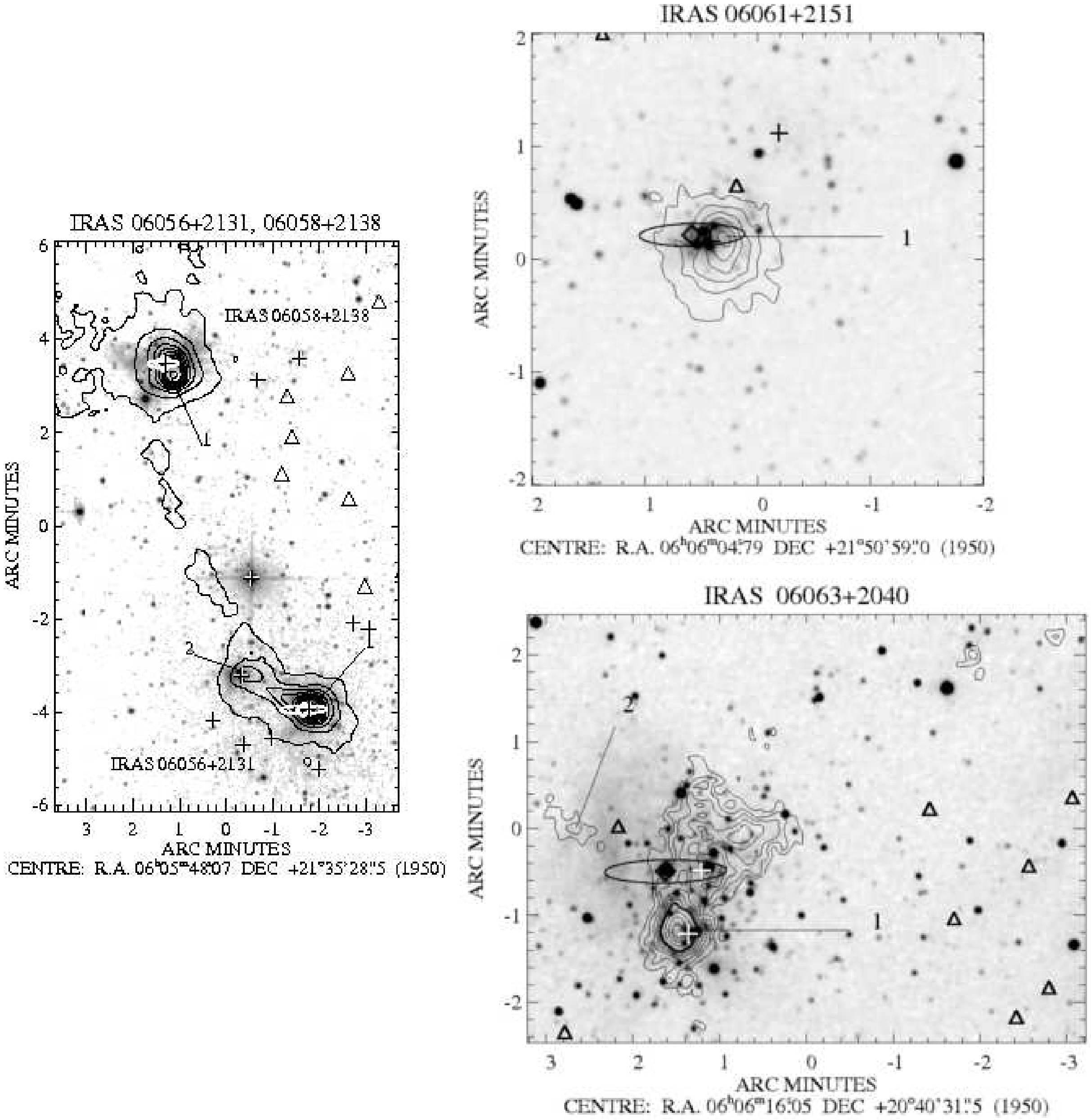

Figure 3.1: Single-dish maps of the four regions in the sample. In all panels the gray-scale represents the *K*-band 2MASS image and the contours represent the (sub)mm map. For IRAS 06061+2151 the IRAM 30 m 1.3 mm contour map is presented, for the other 3 regions the contours are the JCMT 850 μm emission. The IRAS sources plus positional errors are denoted by a diamond together with an error ellipse. Entries in the MSX point source catalog are denoted by a plus sign (resolution 18″, positional uncertainty 2″). NVSS radio point sources are indicated by triangles (resolution 45″, positional uncertainty < 7″). Adapted from Klein et al. (2005)

In all cases the 2 GHz receiver was tuned to the $H_2CO\,(3_{0,3}-2_{0,2})$ line in the lower sideband, chunk #9. With this spectral setup we mapped the continuum at 1.4 mm and observed the transitions described in Table 3.2 with a spectral resolution of $\sim 0.6\,\mathrm{km\,s^{-1}}$, adopting for each source the systemic velocities shown in Col. 5 of Table 3.1.

The phase and amplitude calibrators were the quasars 0510+180 and 0530+135, and the flux calibrators were 3C279, 3C273, Uranus and Titan, adopting for the calibration the flux values from the SMA flux monitoring for the quasars and the SMA Planetary Visibility Function Calculator for the planets. The data were calibrated with the IDL superset MIR[2] (Scoville et al. 1993) and then imaged with MIRIAD (Sault et al. 1995). The spectra were exported to, and processed with, CLASS90, from the GILDAS[3] package (Pety 2005).

After imaging and deconvolution, the resulting synthesized beams for the continuum data are $1.6''\times1.4''$ for IRAS 06056+2131-N and IRAS 06061+2151, $1.3''\times1.2''$ for IRAS 06056+2131-S and IRAS 06063+2040, and $1.2''\times0.9''$ for IRAS 06058+2138. At the given distances of 2 kpc of all the regions, this translates into spacial resolutions between ~ 2200 and ~ 3000 AU. The obtained noise levels for the continuum and line data of each pointing are detailed in Tables 3.3 and 3.2, respectively.

Table 3.2: Observed molecular transitions and rms of the respective maps.

Transition	ν	Sp.Res.	E_{up}	rms[a] (mJy beam^{-1})				
	(GHz)	(MHz)	(K)	i56n	i56s	i58	i61	i63
SiO (5 − 4)	217.105	0.36	31.2	···	68.9	99.0	···	···
DCN (3 − 2)	217.239	0.36	20.9	81.6	66.3	76.6	···	···
$H_2CO\,(3_{0,3}-2_{0,2})$	218.222	0.36	21.0	85.1	88.9	76.6	62.7	62.3
$CH_3OH\,(4_{2,2}-3_{1,2})$	218.440	0.36	45.5	···	···	126	52.3	···
$H_2CO\,(3_{2,2}-2_{2,1})$	218.476	0.36	68.1	···	65.1	58.1	50.4	···
$H_2CO\,(3_{2,1}-2_{2,0})$	218.760	0.36	68.1	···	···	55.2	54.2	···

[a] The rms reported here is the average of the rms of all the channels.

Notes – The abbreviations are as follow: i56n → IRAS 06056+2131-N; i56s → IRAS 06056+2131-S; i58 → IRAS 06058+2138; i61 → IRAS 06061+2151; i63 → IRAS 06063+2040.

---

[2] The MIR cookbook by Charlie Qi can be found at http://cfa-www.harvard.edu/~cqi/mircook.html

[3] http://www.iram.fr/IRAMFR/GILDAS

3.3 Results

3.3.1 Millimetric Continuum

In our continuum maps we established a detection threshold of 4σ for regions IRAS 06056+2131 and IRAS 06058+2138, while for IRAS 06061+2151 and IRAS 06063+2040 a 3σ threshold was considered safe to adopt. These thresholds are sufficient to rule out any possible contribution from sidelobes in the maps, i.e., there are no negative contours above those values. The adopted thresholds correspond to the mass and column density values shown in Table 3.3. Figs. 3.2 to 3.5 show the 1.4 mm continuum maps obtained, with the detected sources marked with triangles. In IRAS 06056+2131-N and IRAS 06056+2131-S we detect 8 and 13 sources respectively, 15 are detected in IRAS 06058+2138and 4 in both IRAS 06061+2151 and IRAS 06063+2040. The properties of these sources are summarized in Table 3.4. Cols. 2 and 3 give their absolute positions. The measured peak flux intensity and integrated flux density are given in Cols. 4 and 5 respectively.

Table 3.3: Properties of the continuum emission.

IRAS Region	Sources [a]	SMA S_ν [c] (Jy)	SD S_ν [d] (Jy)	Rec. S_ν [e] (%)	rms (mJy beam^{-1})	Detection Thresholds [b] I_ν (mJy beam^{-1})	Mass ($M_\odot$)	$N(H_2)$ (10^{24} cm^{-2})
06056+2131-N	8	0.12	0.16	73	1.55	6.2	1.6	0.5
06056+2131-S	13	0.46	0.74	62	2.26	9.0	2.4	1.1
06058+2138	15	0.86	3.91	22	2.28	9.1	2.4	1.4
06061+2151	4	0.29	0.45	64	2.62	7.9	1.8	0.5
06063+2040	4	0.02	0.22	11	1.1	3.2	0.8	0.4

[a] Detections above the flux threshold in Col. 7.

[b] Masses and column densities calculated assuming $T_{ex} \sim 35$ K (Klein et al. 2005), and grain emissivity index $\beta = 2$ (see text).

[c] Total flux recovered within the primary beam of the SMA

[d] Single-dish flux reported by Klein et al. (2005) at 1.3 mm or 850 μm, see Sec. 3.5.1 for details.

[e] Percentage of recovered single-dish flux based on the fluxes in Col. 4.

Because the brightness temperature at 1.4 mm of the corresponding Planck function for the strongest source in all regions is less than about 2 K, just $\sim$ 2% of the typical hot core temperatures of $\sim$100 K, we can assume that the emission comes from optically thin dust and thus calculate the masses and column densities with the approach outlined by Hildebrand (1983) and adapted by Beuther et al. (2002b, 2005). We adopted a distance of 2 kpc, a gas-to-dust ratio of

186 (Draine et al. 2007), and used a grain emissivity index $\beta = 2$ for all regions, corresponding to a dust opacity per unit mass $\kappa_{1.4\,\mathrm{mm}} \sim 0.3\,\mathrm{cm^2\,g^{-1}}$ for a median grain size $a = 0.1\,\mu$m, a grain mass density $\rho = 3\,\mathrm{g\,cm^{-3}}$. The calculated masses and H_2 column densities are in Cols. 6 and 7 of Table 3.4, respectively. For their calculation we used an average IRAS temperature T ~ 35 K, according to the values in Klein et al. (2005). The visual extinctions in Col. 8 were calculated assuming $A_v = N(H_2)/0.94 \times 10^{21}$ (Frerking et al. 1982).

The fluxes obtained and by extension the masses calculated are affected by the spatial filtering inherent to interferometers. Our shortest baseline of 16m at the given distance of 2 kpc corresponds to a spatial scale of ~ 28000 AU at 1.4 mm, therefore any structure larger than this was not detected. Comparison with single-dish data (Klein et al. 2005) indicate that while only about ~ 10% to ~ 20% of the flux was recovered in the case of IRAS 06058+2138 and IRAS 06063+2040, for the other regions the recovered flux is about ~ 60% to ~ 70% (see Table 3.3). In all cases, the remaining flux is part of the filtered out large-scale common envelope (see Sec. 3.5.1 for further discussion).

The continuum emission and the SINFONI NIR data for each region are discussed in detail in Sec. 3.5.1.

3.3.2 Formaldehyde

In a similar approach taken in Chapter 2 for the source IRAS 19410+2336 we aimed to do an estimation of the kinetic temperature structure of the MSF regions. In that direction we observed the $H_2CO\,(3_{0,3} - 2_{0,2})$, $H_2CO\,(3_{2,2} - 2_{2,1})$ and $H_2CO\,(3_{2,1} - 2_{2,0})$ transitions, known to function as a gas thermometer (e.g., Mangum & Wootten 1993).

At least one of the targeted formaldehyde transitions are detected in the regions of our sample. According to Mangum & Wootten (1993) and as I have shown previously in Chapter 2, the detection of $H_2CO\,(3_{0,3} - 2_{0,2})$ and $H_2CO\,(3_{2,2} - 2_{2,1})$ would be enough to determine the temperature of the cores. This would be the case for all the regions, with the exceptions of IRAS 06056+2131-N and IRAS 06063+2040. However the obtained SMA data is affected by missing short spacings in a similar way as shown previously for IRAS 19410+2336. In this case however, we do not have yet single-dish observations at this moment. Such observations will be proposed to be carried out with the IRAM 30m telescope for the Winter 2010 semester. Because of this it is not yet possible to use the H_2CO emission to derive the core temperatures. However, one of the surprising results from Chapter 2 was that the knowing the temperature structure of IRAS 19410+2336 did not change its CMF significantly.

Table 3.4: Properties of the continuum millimetric sources in the observed regions.

Source	R.A. (J2000)	Dec. (J2000)	I_ν (mJy beam^{-1})	S_ν (mJy)	Mass ($M_\odot$)	N (H_2) (10^{23} cm^{-2})	A_v (10^3 mag)
IRAS 06056+2131-N							
i56n-1	06 08 46.24	21 31 54.85	6.6	1.6	1.7	0.5	0.5
…-2	06 08 46.91	21 31 45.32	7.7	3.1	2.0	0.6	0.6
…-3	06 08 46.82	21 31 46.73	8.4	3.6	2.2	0.6	0.7
…-4	06 08 46.72	21 31 44.26	38.7	69.3	18.1	2.9	3.1
…-5	06 08 46.54	21 31 45.70	9.8	4.9	2.6	0.7	0.8
…-6	06 08 46.26	21 31 45.77	8.9	6.9	2.3	0.7	0.7
…-7	06 08 46.14	21 31 45.43	10.3	12.7	3.3	0.8	0.8
…-8	06 08 45.93	21 31 46.32	12.7	16.2	4.2	1.0	1.0
IRAS 06056+2131-S							
i56s-1	06 08 40.76	21 31 06.43	13.3	4.1	3.5	1.5	1.6
…-2	06 08 40.66	21 31 06.94	32.2	37.0	9.7	3.8	4.0
…-3	06 08 40.60	21 31 06.35	28.5	38.2	10.0	3.3	3.5
…-4	06 08 40.61	21 31 05.03	15.2	7.7	4.0	1.8	1.9
…-5	06 08 41.11	21 31 01.12	10.9	6.0	2.8	1.3	1.4
…-6	06 08 40.40	21 31 01.10	41.3	27.4	10.8	4.8	5.1
…-7	06 08 40.33	21 31 01.40	61.2	89.9	23.5	7.2	7.6
…-8	06 08 40.28	21 31 00.62	41.3	41.1	10.7	4.8	5.1
…-9	06 08 40.14	21 31 02.16	10.7	5.0	2.8	1.3	1.3
…-10	06 08 40.13	21 30 58.27	24.4	27.4	7.1	2.9	3.0
…-11	06 08 39.95	21 30 58.97	11.0	10.3	2.9	1.3	1.4
…-12	06 08 40.10	21 30 57.33	11.0	73.7	19.2	1.3	1.4
…-13	06 08 39.97	21 30 52.59	14.5	15.8	4.1	1.7	1.8
IRAS 06058+2138							
i58-1	06 08 53.46	21 38 30.19	12.4	11.1	3.2	1.9	2.0
…-2	06 08 53.33	21 38 28.92	38.9	51.7	13.5	6.0	6.3

Continued on next page…

Table 3.4 – Continued

Source	R.A. (J2000)	Dec. (J2000)	I_ν (mJy beam^{-1})	S_ν (mJy)	Mass ($M_\odot$)	N (H_2) (10^{23} cm^{-2})	A_v (10^3 mag)
...-3	06 08 53.32	21 38 13.68	17.5	19.6	5.1	2.7	2.9
...-4	06 08 53.41	21 38 13.18	22.8	29.0	7.6	3.5	3.7
...-5	06 08 53.35	21 38 11.57	56.3	128.5	33.5	8.6	9.2
...-6	06 08 53.38	21 38 10.37	41.9	55.5	14.5	6.4	6.8
...-7	06 08 53.24	21 38 09.84	64.1	123.5	32.3	9.8	10.5
...-8	06 08 53.38	21 38 09.03	27.6	54.6	14.2	4.2	4.5
...-9	06 08 53.44	21 38 07.30	13.4	14.9	3.9	2.1	2.2
...-10	06 08 52.98	21 38 11.07	25.5	20.4	6.7	3.9	4.2
...-11	06 08 52.93	21 38 05.56	19.9	17.3	5.2	3.0	3.2
...-12	06 08 52.79	21 38 02.41	25.3	23.5	6.6	3.9	4.1
...-13	06 08 53.52	21 38 08.90	18.8	31.4	8.2	2.9	3.2
...-14	06 08 53.55	21 38 10.30	17.8	30.2	7.9	2.7	2.9
...- 15	06 08 53.56	21 38 11.30	17.3	26.1	6.8	2.7	2.8
IRAS 06061+2151							
i61-1	06 09 06.99	21 50 41.36	110.3	224.5	50.0	7.2	7.7
...-2	06 09 06.84	21 50 43.44	8.8	3.8	2.0	0.6	0.6
...-3	06 09 06.81	21 50 41.63	10.3	6.1	2.3	0.7	0.7
...-4	06 09 06.82	21 50 29.47	9.7	9.7	2.2	0.6	0.7
IRAS 06063+2040							
i63-1	06 09 21.28	20 38 51.02	6.4	6.0	1.4	0.7	0.8
...-2	06 09 21.18	20 38 55.70	5.4	9.6	2.5	0.6	0.6
...-3	06 09 20.85	20 38 53.85	3.9	4.7	1.2	0.4	0.5
...-4	06 09 20.97	20 38 46.43	11.5	15.1	3.9	1.3	1.4

IRAS 06056+2131

The $H_2CO\,(3_{0,3}-2_{0,2})$ emission peaks in the Northern clump match in all cases continuum sources. The strongest peak is located at the position of source i56n-7, while the secondary peaks are associated with sources i56n-2 to i56n-5. This in particular strengthens the identification of sources i56n-2,3 and -5 as individual cores. From the first-moment map no clear velocity gradient can be determined, although there is a velocity differential of about $\sim 2\,\mathrm{km\,s^{-1}}$ in the east-west direction along the main continuum source i56n-4 (see Fig. 3.6). We did not detect any of the other two formaldehyde transitions targeted.

In the Southern clump the $H_2CO\,(3_{0,3}-2_{0,2})$ emission has its strongest peak towards the proto-system i56s-A, with secondary peaks not matching any of the other detected sources, but instead bordering the continuum emission. The first-moment map show a velocity gradient running in the north-south direction along the continuum emission, with the northern tip redshifted and the southern tip blueshifted a few $\mathrm{km\,s^{-1}}$ respect to the rest velocity of $\sim 2.5\,\mathrm{km\,s^{-1}}$ (see Fig. 3.6). $H_2CO\,(3_{2,2}-2_{2,1})$ is detected towards similar positions as $H_2CO\,(3_{0,3}-2_{0,2})$. In particular, the strongest emission peak, as well as the second brightest, are located at the same positions as before. The first-moment map also shows the velocity gradient described before (see Fig. 3.6). No $H_2CO\,(3_{2,1}-2_{2,0})$ emission was detected.

IRAS 06058+2138

For this region the $H_2CO\,(3_{0,3}-2_{0,2})$ emission present its brightest peaks offset from any continuum source. Nevertheless a secondary peak can be associated with one the bright continuum source i58-7, and the other emission peaks are located in the same spatial region as the main continuum emission. The intensity-weighted velocity map does not show any clear velocity gradient or structure (see Fig. 3.7).

The $H_2CO\,(3_{2,2}-2_{2,1})$ transition has a similar emission structure as the previous line, with its emission peaks at approximately the same positions. However, it is noted that the emission feature located south-east of the continuum source i58-9 is relatively brighter for this molecular transition than for $H_2CO\,(3_{0,3}-2_{0,2})$. In the same way as before, there is no strong variation or defined structure in the velocity field (see Fig. 3.7).

This region is one of the only two towards which we detected the $H_2CO\,(3_{2,1}-2_{2,0})$ transition. Its integrated emission has a spatial structure more similar to $H_2CO\,(3_{2,2}-2_{2,1})$ than to $H_2CO\,(3_{0,3}-2_{0,2})$, and again the first-moment shows a small velocity dispersion of $\sim 2\,\mathrm{km\,s^{-1}}$ (see Fig. 3.7).

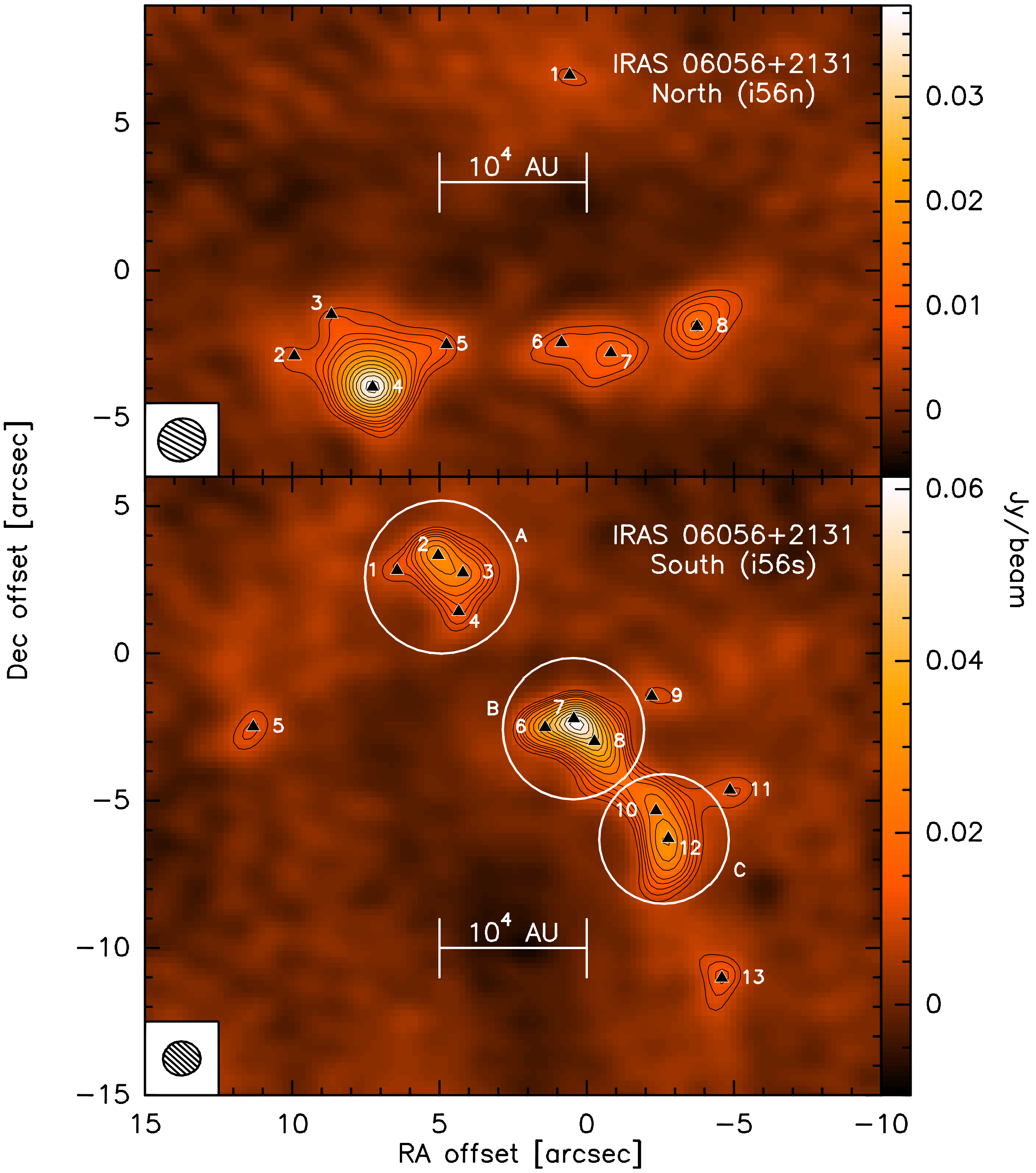

Figure 3.2: Continuum maps of IRAS 06056+2131 obtained with the SMA at 1.4 mm. On the top and bottom panels are the maps of the Northern and Southern protoclusters, respectively. The contours start at the 4σ level in both panels, increasing in 1σ steps up to the 8σ contour and in 2σ steps afterwards (see Table 3.3 for the σ values). The triangles mark the position of the detected sources. In the lower panel are circled the three "protosystems" described in the text. The synthesized beam is in the lower-left corner of each map, and the scalebar in each map represent a projected length of 10000 AU.

IRAS 06061+2151 and IRAS 06063+2040

Region IRAS 06061+2151 is the second one where $H_2CO\,(3_{2,1} - 2_{2,0})$ is detected. Together with the other two H_2CO molecular transitions targeted, the only detected emission comes from the main continuum source i61-1 (see Fig. 3.8).

In the case of IRAS 06063+2040 only $H_2CO\,(3_{0,3} - 2_{0,2})$ is detected. The emission is associated to the continuum emission, however none of its emission peaks matches a continuum source. The strongest emission features are located in the bow-shaped continuum feature formed by sources i63-1 to i63-3, and there is also $H_2CO\,(3_{0,3} - 2_{0,2})$ emission towards the main continuum source i63-4 (see Fig. 3.9).

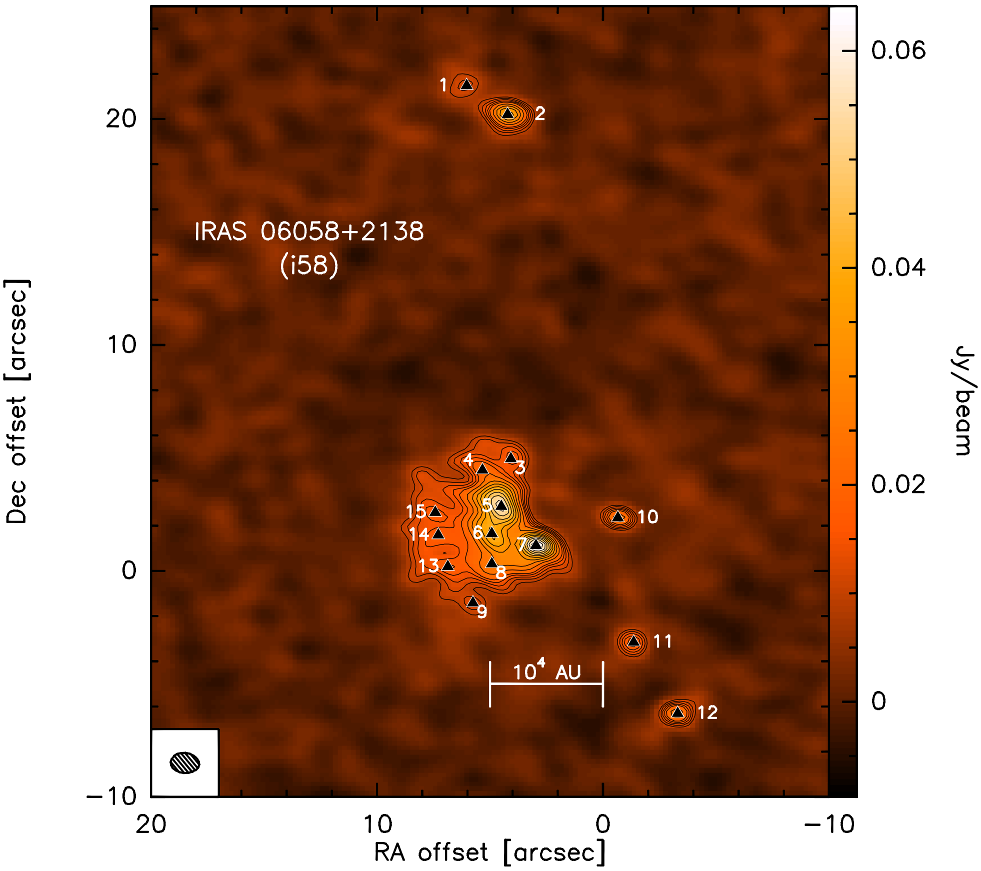

Figure 3.3: Continuum maps of IRAS 06058+2138 obtained with the SMA at 1.4 mm. The contours start at the 4σ level increasing in 1σ steps up to the 8σ contour and in 2σ steps afterwards (see Table 3.3 for the σ values). The triangles mark the position of the detected sources. The synthesized beam is in the lower-left corner, and the scalebar represent a projected length of 10000 AU.

3.3.3 Deuterated hydrogen cyanide

Deuterium has a low abundance ratio, of about D/H $\sim 10^{-5}$ in the local interstellar medium (ISM) and as low as $\sim 8 \times 10^{-8}$ outside the standard 100 pc of the Local Bubble (Linsky 2003). Despite that, high abundances of deuterated molecules are observed in dark clouds and star-forming regions (e.g., Parise et al. 2007). Deuterated species are associated to cold environments such as prestellar cores, but they are also observed in the gas phase of hot cores because they are believed to have been evaporated from icy mantles of dust grains (e.g. Caselli & Dore 2005; Cyganowski et al. 2007; Parise et al. 2007).

In our case, we detect the DCN $(3-2)$ transition in regions IRAS 06056+2131 and IRAS 06058+2138. Figs. 3.10 and 3.11 show the observed DCN integrated emission. It can be seen that the emission features are located at the border of the brighter continuum peaks. Noticeably, in regions IRAS 06056+2131-S and IRAS 06058+2138 a DCN feature is located peaking *between* the main continuum peaks. Also in IRAS 06058+2138, the first-moment map shows a velocity gradient of $\sim 4\,\mathrm{km\,s^{-1}}$ in the S-N direction. Since it encompasses the continuum emission, it is likely an indicator of the overall rotation of the cloud.

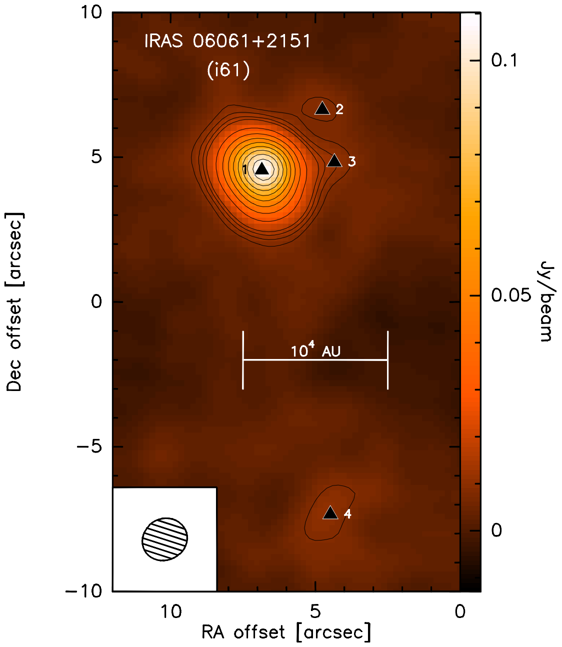

Figure 3.4: Continuum map of IRAS 06061+2151 obtained with the SMA at 1.4 mm. The contours start at the 3σ level, increasing in 1σ steps up to the 6σ contour and in 4σ steps afterwards (see Table 3.3 for the σ values). The triangles mark the position of the detected sources. The synthesized beam is in the lower-left corner, and the scalebar represent a projected length of 10000 AU.

3.3.4 Methanol

This molecular species is believed to form more efficiently in grain surfaces than in the gas-phase medium. High abundances of CH_3OH are achieved by the evaporation of the grain mantles either by the passing of a shock or by the radiation field of a young protostellar object (e.g., Bacmann et al. 2007; Charnley et al. 1992; Charnley 1997; Garrod & Herbst 2006). Its presence usually indicates ongoing star formation and/or the presence of a strong radiation field.

We detect the $CH_3OH\,(4_{2,2} - 3_{1,2})$ transition in regions IRAS 06058+2138 and IRAS 06061+2151. In the latter the only emission feature matches the position of the main mm source (see Fig. 3.12) and presents a gradient of about $\sim 3\,\mathrm{km\,s^{-1}}$in the E-W direction more likely tracing the overall rotation of the cloud, while in the former the emission extends over the same spatial region as the continuum emission, but the main emission peak is located about $\sim 5''$ to the south of the main continuum sources (see Fig. 3.13).

Since methanol is not important in the current context, we omit further discussion.

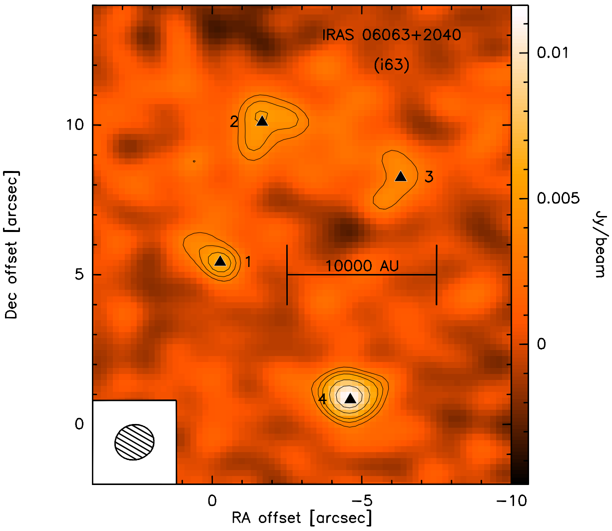

Figure 3.5: Continuum map of IRAS 06063+2040 obtained with the SMA at 1.4 mm. The contours start at the 3σ, with increments of 1σ up to the 7σ level continuing in 2σ steps (see Table 3.3 for the σ values). The triangles mark the position of the detected sources. The synthesized beam is in the lower-left corner, and the scalebar represent a projected length of 10000 AU.

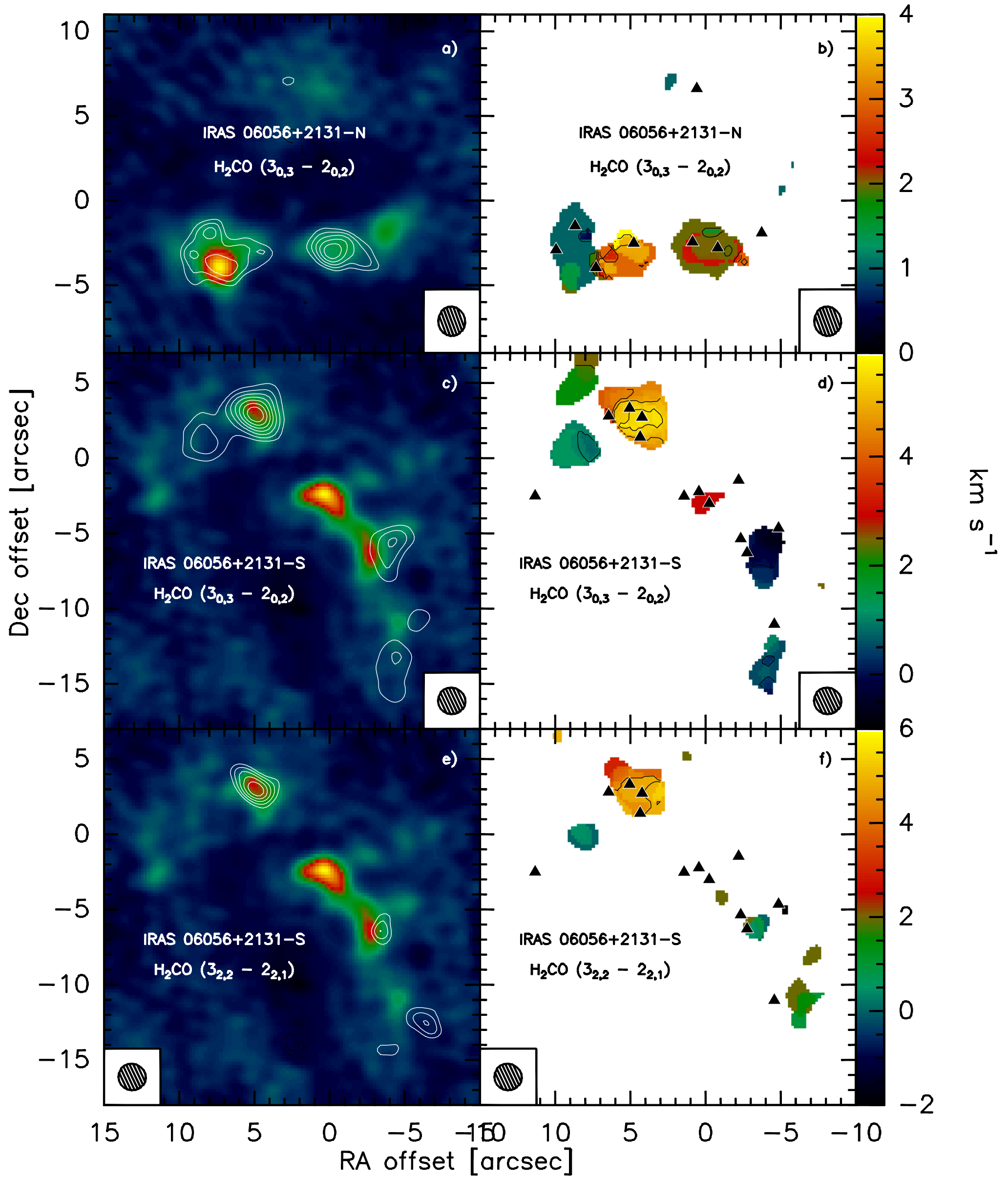

Figure 3.6: Formaldehyde maps of IRAS 06056+2131. The left column shows the zeroth-moment maps and the right column the first-moment maps of $H_2CO\,(3_{0,3}-2_{0,2})$ for IRAS 06056+2131-N (upper row), and $H_2CO\,(3_{0,3}-2_{0,2})$ (middle row) and $H_2CO\,(3_{2,2}-2_{2,1})$ for IRAS 06056+2131-S (lower row). The background in the left column is the continuum emission (see Fig. 3.3), and the contours is the integrated emission of the line in steps of 10% of the peak intensity. In the left column the background shows the intensity-weighted velocity, with contours in 0.5 km s^{-1} steps. The triangles mark the continuum sources detected, and the beam appears at the bottom of each panel. The rest velocity is $V_{\rm lsr} \sim 2.5$ km s^{-1}.

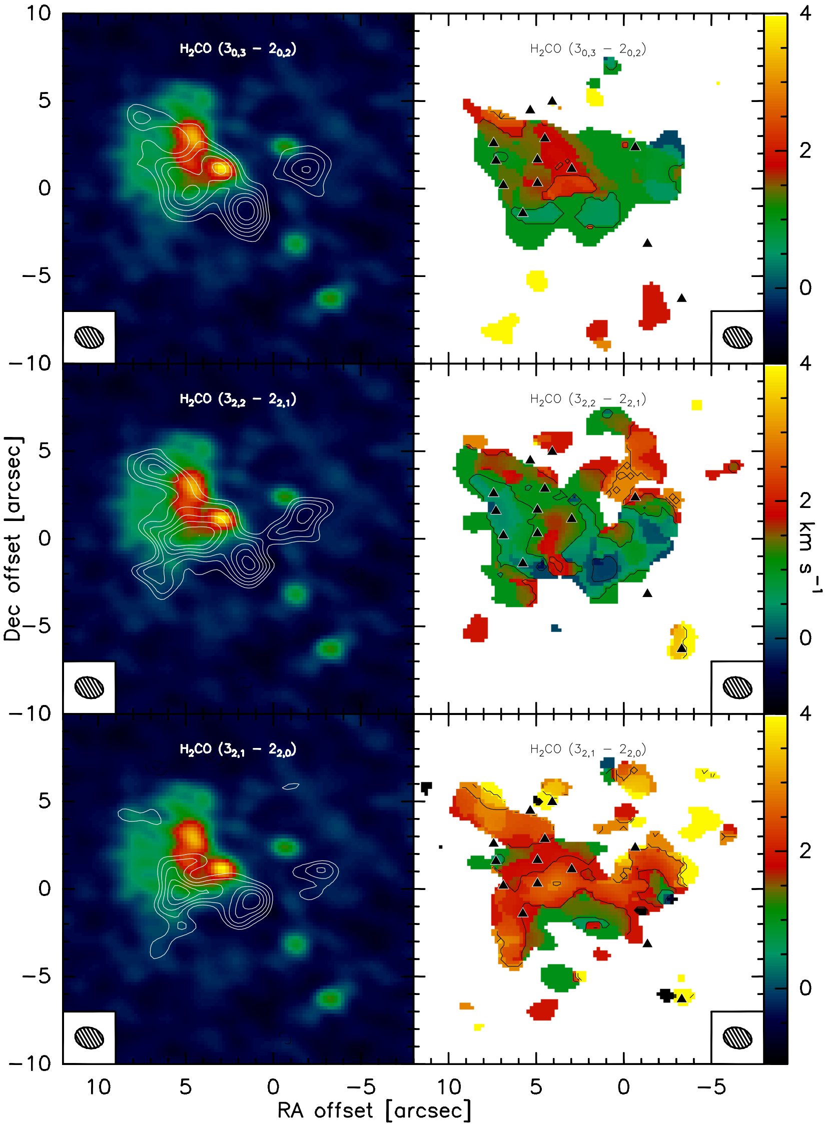

Figure 3.7: Formaldehyde maps of IRAS 06058+2138. The left column shows the zeroth-moment maps and the right column the first-moment maps of $H_2CO\,(3_{0,3} - 2_{0,2})$ (upper row), $H_2CO\,(3_{2,2} - 2_{2,1})$ (middle row) and $H_2CO\,(3_{2,1} - 2_{2,0})$ (lower row). The background in the left column is the continuum emission (see Fig. 3.3), and the contours are the integrated emission of the line in steps of 10% of the peak intensity, starting at 40%. In the left column the background shows the intensity-weighted velocity, with contours in 1 km s^{-1} steps. The triangles mark the continuum sources detected, and the beam appears in the lower-right corner of each panel. We can see in the left column how the emission peaks of the three H_2CO lines are located in similar positions. The right column shows that there is no signature of a strong velocity dispersion. The rest velocity is $V_{\rm lsr} \sim 3$ km s^{-1}.

3.3.5 Silicon monoxide

We detect the SiO (5 – 4) transition of this shock and outflow tracer in regions IRAS 06056+2131-S and IRAS 06058+2138. In Fig. 3.14 is shown how the integrated SiO (5 – 4) emission towards IRAS 06056+2131-S is located in two features. The northernmost feature appears to trace the compact component of an outflow in the SE-NW direction, likely driven by one of the sources i56s-1 to -4. The southern SiO (5 – 4) feature would be tracing an outflow almost perpendicular to the other one. It has no clear driving source, but since i56s-7 is the strongest mm source it is a likely candidate to be the driving source. In this region the SiO (5 – 4) emission is very weak, and to map it we had to degrade the spectral resolution of the data to $5\,\mathrm{km\,s^{-1}}$. The recovered emission is centered at the rest velocity of $\sim 2.5\,\mathrm{km\,s^{-1}}$ and therefore comprises gas velocities from $0\,\mathrm{km\,s^{-1}}$ to $\sim 5\,\mathrm{km\,s^{-1}}$.

Fig. 3.15 shows that the case of IRAS 06058+2138 is slightly different. In this region SiO (5 – 4) emission is detected in the $\sim 1 - 9\,\mathrm{km\,s^{-1}}$ velocity range. It is mainly distributed in a SE-NW direction, and would appear to be tracing an outflow probably driven by any of the main mm sources. If that is the case, we would be detecting mostly its redshifted lobe, since most of the SiO (5 – 4) emission is detected at the rest velocity of $\sim 3\,\mathrm{km\,s^{-1}}$ and higher. There is also an emission feature associated with source i58-1, centered at the rest velocity and with a width of $\sim 2\,\mathrm{km\,s^{-1}}$.

3.4 Deriving the Core Mass Function

3.4.1 The Differential CMF

As stated before, we observed H_2CO transitions with the purpose of determine a temperature structure for each region. However, the H_2CO data is affected by missing flux, and therefore we cannot get meaningful results from them until the data is complemented with short-spacing observations, proposed at the IRAM 30 m Telescope for the Winter 2009/2010 semester.

Because of this, we calculated the masses and column densities of each region using an average value of the kinetic temperature (T_{kin}) throughout each region. In a similar approach to Beuther & Schilke (2004), we adopted the IRAS temperature of each region. According to Klein et al. (2005), all the regions in our sample have similar temperatures, therefore we adopted an average value $T_{\mathrm{kin}} \sim 35\,\mathrm{K}$ for all the regions, obtaining the masses and column densities shown in Col. 6 of Table 3.4. Furthermore, we have already seen in Chapter 2 that the difference introduced in the slope of the CMF of IRAS 19410+2336 by using or not the H_2CO temperatures is marginal.

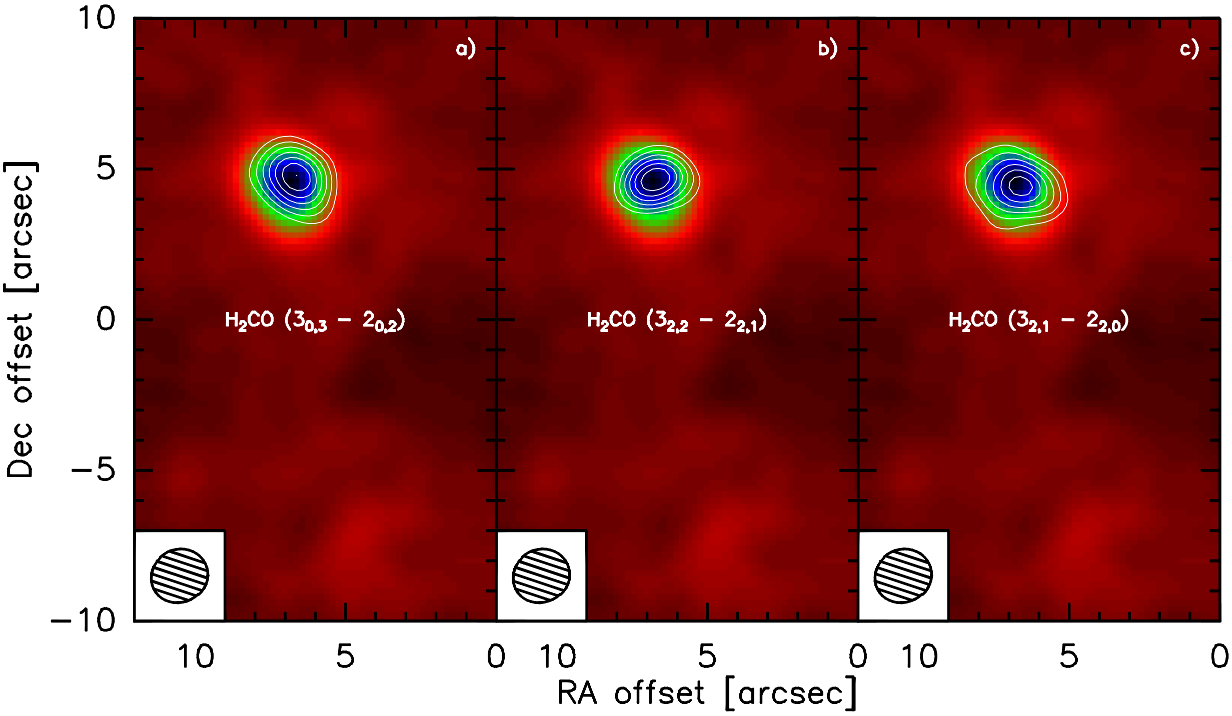

Figure 3.8: Formaldehyde maps of IRAS 06061+2151. The left, central and right panels show the integrated emission of the $H_2CO\,(3_{0,3} - 2_{0,2})$, $H_2CO\,(3_{2,2} - 2_{2,1})$ and $H_2CO\,(3_{2,1} - 2_{2,0})$ transitions, respectively. The background in all panels is the continuum emission (see Fig. 3.4), and the contours are the integrated emission of the line in steps of 10% of the peak intensity. The beam appears in the lower-left corner of each panel. The only detection for the 3 transitions is towards the main continuum source. The rest velocity is $V_{lsr} \sim 0\,km\,s^{-1}$.

Against our expectactions the regions IRAS 06061+2151 and IRAS 06063+2040 show too few cores as to derive a mass function. The same can be said for regions IRAS 06056+2131 and IRAS 06058+2138, however these two regions have similar properties. Their luminosities are on the order of $\sim 10^4\,L_\odot$, and their masses are $M \sim 570\,M_\odot$ for IRAS 06056+2131 and $M \sim 510\,M_\odot$ for IRAS 06058+2138 (Klein et al. 2005). They are located about $\sim 7'$ apart in the sky, and not only they are at the same distance of ~ 2 kpc but they are also connected by a bridge of material seen at 850 μm (see Fig. 3.1). Klein et al. (2005) proposed that this bridge may be caused either by tidal forces between the regions or perhaps a remnant of the fragmentation process, in which case both regions would come from the same molecular cloud. The mentioned properties of IRAS 06056+2131 and IRAS 06058+2138 encouraged us to combine their data and derive a common differential CMF $\Delta N/\Delta M$, with the number of cores ΔN per mass bin ΔM.

Combining the two regions we detect 36 cores. Although this is 40% more than for IRAS 19410+2336, it is still a relatively low number when compared to studies of stellar clusters with hundreds or thousands of stars. Because of that, we applied the same analysis detailed in

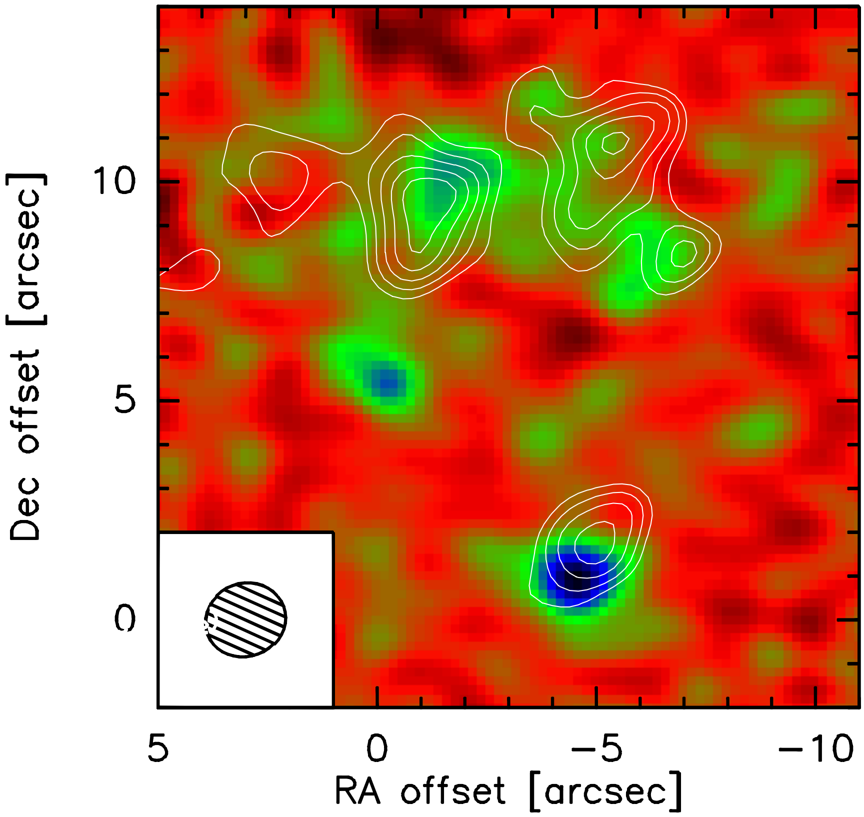

Figure 3.9: Integrated emission map of the $H_2CO\,(3_{0,3} - 2_{0,2})$ transition towards IRAS 06063+2040. The background is the continuum emission (see Fig. 3.5), and the contours are the integrated emission of the line in steps of 10% of the peak intensity. The beam appears in the lower-left corner. This is the only H_2CO transition detected of the 3 targeted. There is an emission peak associated with the main source, and a second emission feature associated with the arch formed by continuum sources i61-1,2 and -3. The rest velocity is $V_{lsr} \sim 9\,km\,s^{-1}$.

Sec. 2.3.2. In short, we performed a logarithmic binning, meaning that the mass bins have a fixed width B on a logarithmic axis. We derive a mass spectrum for different bin widths with B ranging from 0.001 to 1 in 0.001 steps. We do not fit all the mass spectra obtained but those satisfying the same two criteria established in Sec. 2.3.2, namely that at most only one bin may contain a single core, and that there must be at least four non-empty bins after the incompleteness threshold.

We fit a power-law of the form given by Eq. 2.4 to the CMFs satisfying those two criteria, obtaining a β_B index value corresponding to a given B. The final value β is the weighted mean of all the β_B indices. The different values of the power-law indices β_B are plotted in Fig. 3.16 as a function of the bin width B. The resulting weighted average and its formal error $\beta = -1.5 \pm 0.1$

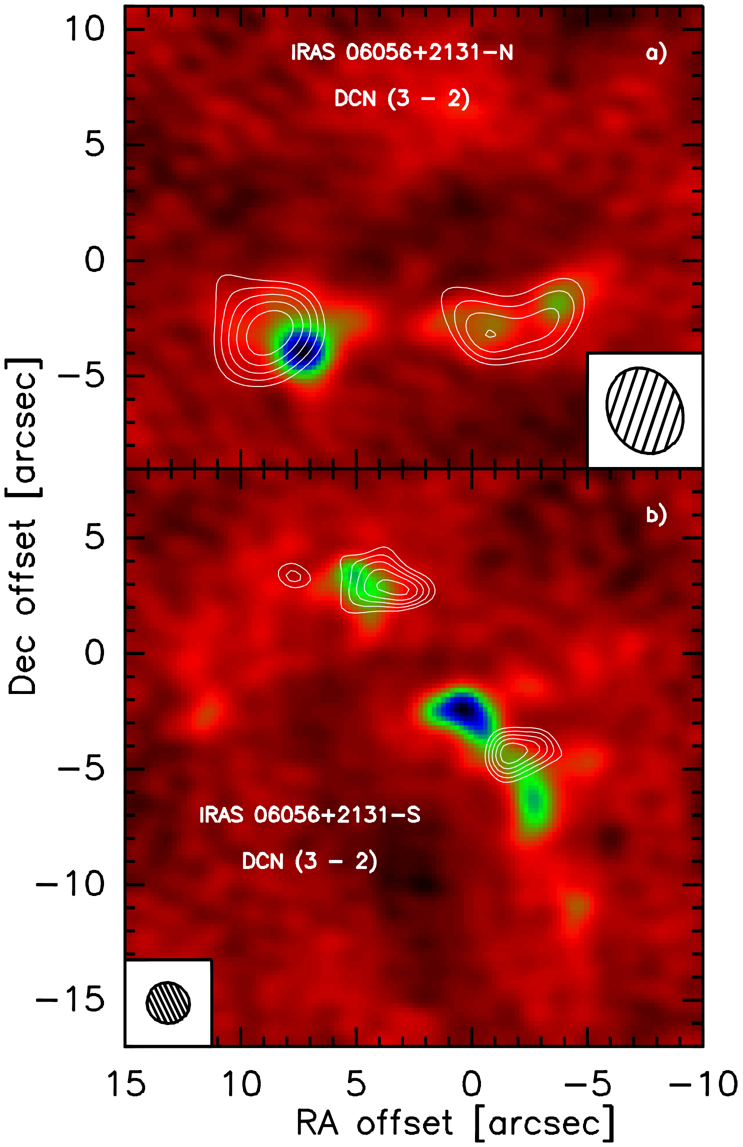

Figure 3.10: DCN integrated emission maps of IRAS 06056+2131-N (upper panel) and IRAS 06056+2131-S (lower panel). The background is the continuum emission (see Fig. 3.2), and the contours are the integrated emission of the line in steps of 10% of the peak intensity. The beam appears at the bottom of each panel. We can see how the main emission peak in all cases is offset from any continuum source, and in the case of IRAS 06056+2131-S an emission feature is located between two continuum peaks. The rest velocity is $V_{\rm lsr} \sim 2.5\,{\rm km\,s^{-1}}$.

are also marked. Unlike for IRAS 19410+2336, this time only one "local trend" can be seen in Fig. 3.16, starting at $B = 0.26$. This feature is explained in detail in Sec. 2.3.2. Aside from this "local trend" there no overall trend seen between β_B and B. It can be seen that the data points are homogeneously distributed between $\beta \sim -1.7$ and $\beta \sim -1.2$.

We see then that our results for the CMF slope are similar to the $\beta \sim -1.6$ found for the Clump Mass Functions (e.g. Kramer et al. 1998; Kerton et al. 2001; Muñoz et al. 2007), obtained with CO emission maps for structures of sizes on the order of ~ 0.1 pc, one order of magnitude larger than the cores we are tracing now. This is surprising, more taking into account our results for IRAS 19410+2336 shown in the previous chapter, where we find a CMF slope comparable to the Salpeter IMF slope.

For reference, Fig. 3.17 shows an example of the CMFs we obtained in this case corresponding to $B = 0.206$ and having a power-law index $\beta = -1.5 \pm 0.1$. A turnover in the distribution for masses below $\sim 2.4\,\mathrm{M}_{\odot}$can be seen. It appears in all the derived CMFs at about the same position, and since it matches our detection threshold, we assume that it is likely caused by the low-mass incompleteness of our sample rather than being a physical feature. In all of the cases, we fit our mass distributions for masses higher than the turnover.

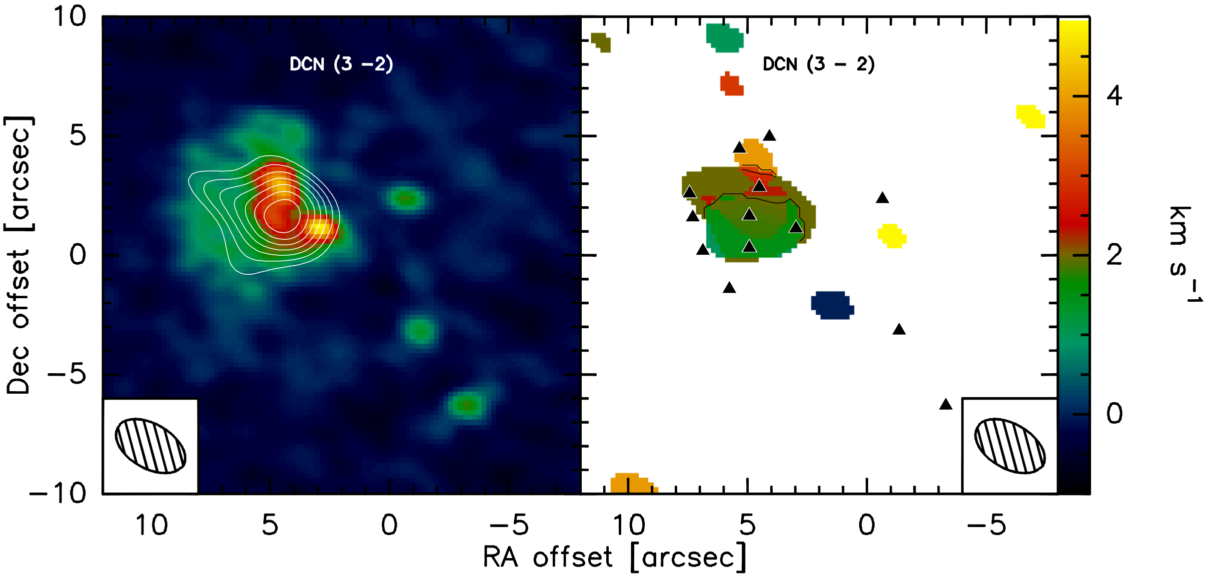

Figure 3.11: DCN maps of IRAS 06058+2138. The left panel shows the zeroth-moment map and the right panel the first-moment map of the DCN (3 – 2) transition. The background in the left panel is the continuum emission (see Fig. 3.3), and the contours are the integrated emission of the line in steps of 10% of the peak intensity, starting at 30%. In the left panel the background shows the intensity-weighted velocity, with contours in 1 km s^{-1} steps. The triangles mark the continuum sources detected, and the beam appears at the bottom of each panel. We can see in the left column how the emission peak is located between the two main continuum sources, and in the right panel we see a velocity gradient of ~ 4 km s^{-1} in the S-N direction. The rest velocity is $V_{\mathrm{lsr}} \sim 3$ km s^{-1}.

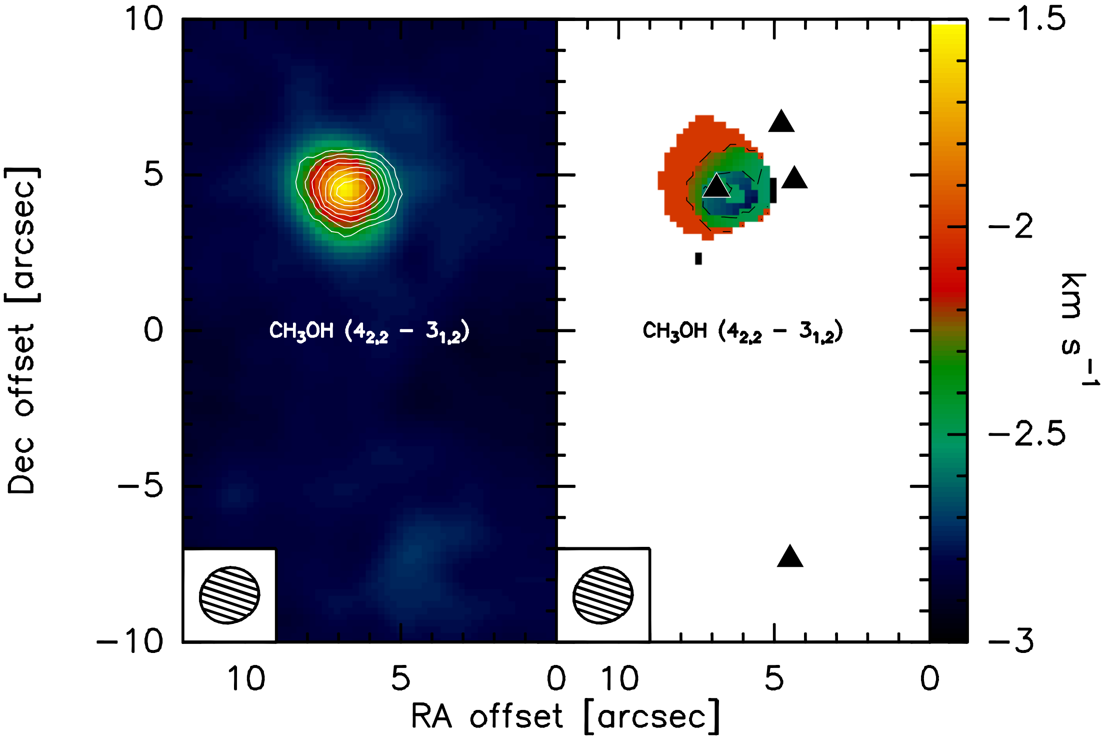

Figure 3.12: Methanol emission towards IRAS 06061+2151. The left panel shows the integrated emission and the right panel the first-moment map of the $CH_3OH\,(4_{2,2} - 3_{1,2})$ transition, with contours in 1 km s^{-1} steps. The background in the left panel is the continuum emission (see Fig. 3.4), and the contours are the integrated emission of the line in steps of 10% of the peak intensity. The triangles mark the continuum sources detected, and the beam appears in the lower-left corner of each panel.The only emission detected matches the position of the main continuum source, and is slightly blueshifted respect to the rest velocity $V_{lsr} \sim 0$ km s^{-1}.

3.4.2 The Cumulative CMF

In the previous section we have taken into account the arbitrariness of the binning of the CMF, however, to avoid the problems arisen by this a arbitrariness we also analyze the cumulative CMF of our sample.

We follow the reasoning detailed in Sec. 2.3.2, and we adopt the expressions for the cumulative CMF described by Eqs. (2.5) and (2.6). The former is derived from the differential CMF described by Eq. (2.4). The latter is also derived from Eq. (2.4), but taking into account the upper-mass cutoff of the distribution, which for our sample is at about $\sim 34\,M_\odot$, corresponding to the core i58-5 (see Table 3.4).

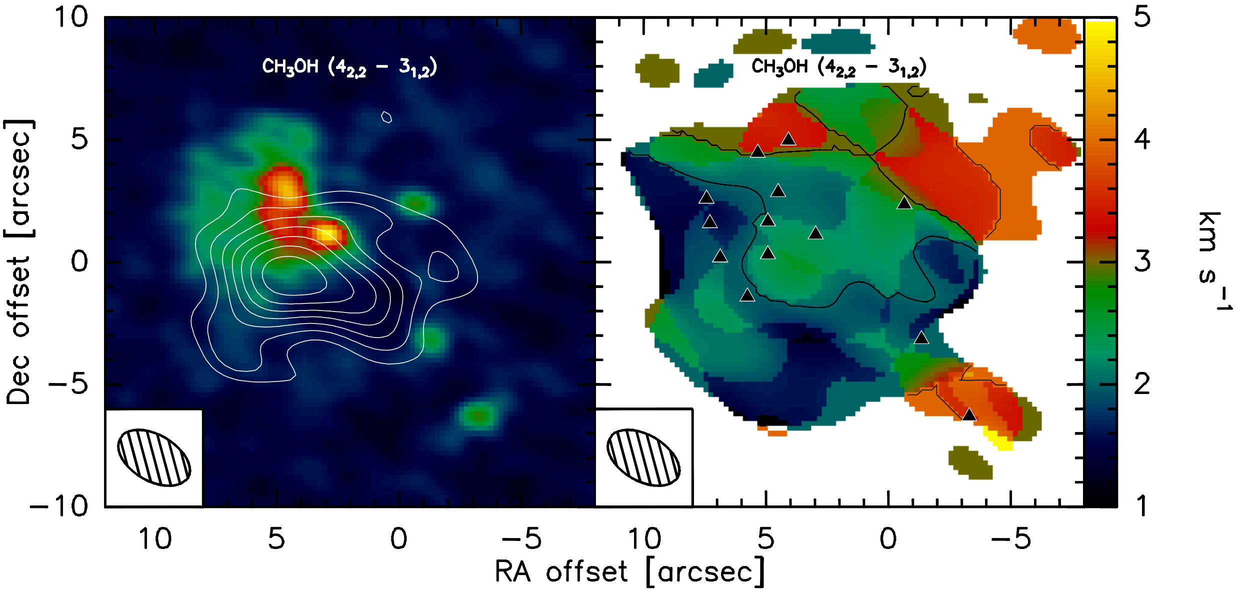

Figure 3.13: Methanol maps of IRAS 06058+2138. The left panel shows the zeroth-moment map and the right panel the first-moment map of the $CH_3OH\,(4_{2,2} - 3_{1,2})$ transition. The background in the left panel is the continuum emission (see Fig. 3.3), and the contours are the integrated emission of the line in steps of 10% of the peak intensity. In the left panel the background shows the intensity-weighted velocity, with contours in 1 km s^{-1} steps. The triangles mark the continuum sources detected, and the beam appears in the lower-right corner of each panel. We can see in the left panel how the main emission peak is located ~ 5″ to the south of the main continuum sources. The first-moment map do not show a strong velocity gradient or structure. The rest velocity is $V_{lsr} \sim 3$ km s^{-1}.

Fig. 3.18 shows the cumulative CMF for masses above ~ 2.5 $M_\odot$. As stated before we fit both the analytical expressions given in Eqs. (2.5) and (2.6). The results are $\beta = -1.8 \pm 0.1$ and $\beta = -1.4 \pm 0.1$, respectively, with the σ values resulting from the fitting algorithm. Although the fitting error on the fitting parameter β are similar in both cases, the fit of Eq. (2.6) is better than the fit of Eq. (2.5). The chi-square value of the former is $\chi^2 \sim 0.16$ while for the latter it is $\chi^2 \sim 0.29$, with χ^2 defined as:

$$\chi^2 = \sum_i \frac{(F_i - O_i)^2}{F_i} \qquad (3.1)$$

where F_i is the value of $N(> M)$ given by the fit for mass M_i, and O_i is the calculated value of $N(> M)$ for mass M_i.

This result shows that the inclusion of M_{max} in the definition of the cumulative CMF affects the result significantly, corroborating the results of Reid & Wilson (2006). Since its χ^2 is better, we adopt the value $\beta = -1.4 \pm 0.1$ given by the fit of Eq. (2.6).

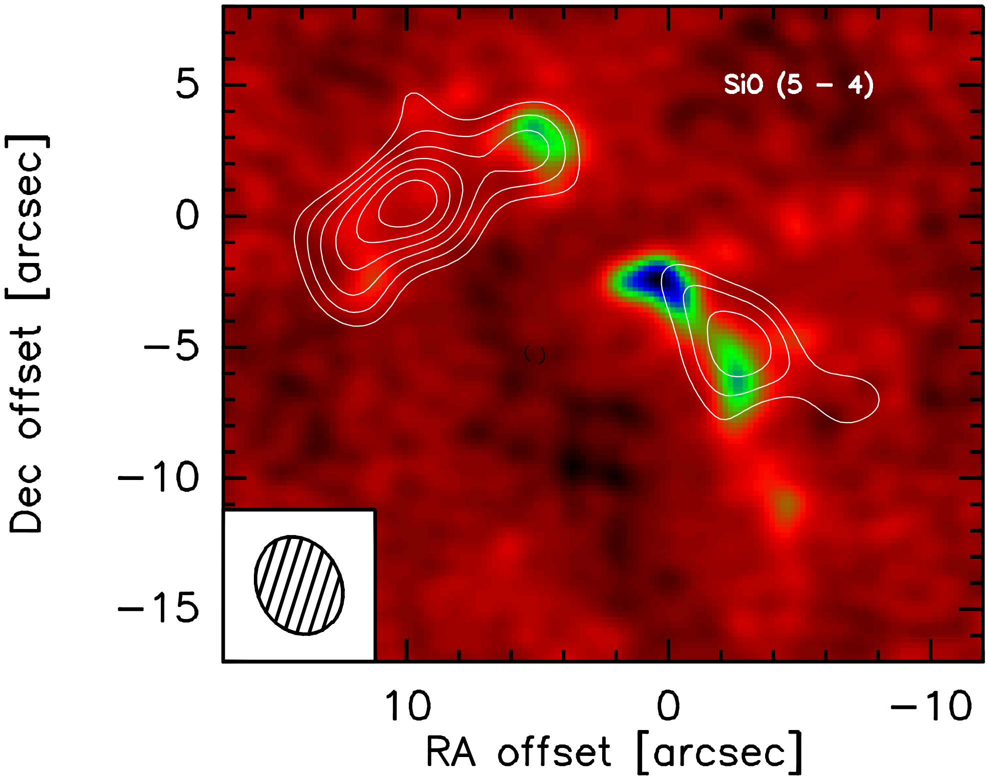

Figure 3.14: SiO integrated emission map of IRAS 06056+2131-S. The background is the continuum emission (see Fig. 3.2), and the contours are the integrated emission of the line in steps of 10% of the peak intensity, starting at 40%. The beam appears in the lower-right corner of each panel. There are two possible outflows, one in the SE-NW direction and the second in the NE-SW direction. The rest velocity is $V_{lsr} \sim 2.5\,km\,s^{-1}$.

3.5 Discussion

3.5.1 (Proto)stellar content

With mm data it is possible to derive the masses of the circumstellar structure of the (proto)stars, but not the masses of the (proto)stars themselves. The masses that we calculate from the 1.4 mm continuum data can be attributed to a circumstellar structure, However, we must take into account the “short-spacing problem” when interpreting the calculated masses of the continuum sources. This caveat, inherent to interferometers, means that a percentage of the flux is filtered out and lost.

Klein et al. (2005) reports single-dish continuum observations of the 4 regions of our sample. The observations are at ~ 1.3 mm with the IRAM 30m Telescope, except for IRAS 06063+2040 that was observed at ~ 850 μm with the JCMT, and indicate the integrated flux densities[4] shown in Col. 4 of Table 3.3. Considering a dependence $S_\nu \propto \nu^4$ the average flux densities we recover within the SMA primary beam in each of the regions (Col. 3 of Table 3.3) correspond to the percentages shown in Col. 5 of Table 3.3 of the single-dish fluxes.

In the cases of IRAS 06056+2131 and IRAS 06061+2151 we recover about two-thirds of the single-dish flux, denoting the rather compact nature of the emission. In those cases, the masses shown in Col. 6 of Table 3.4, although a lower limit, are a good approximation to the circumstellar masses. On the other hand, for regions IRAS 06058+2138 and IRAS 06063+2040 we recover less than a quarter of the flux. This indicate that there is a large fraction of the emission emitted by extended structures, that we are filtering out.

In the following sections we will describe the (proto)stellar content of each region in more detail.

IRAS 06056+2131-N

The detection limit adopted in this region is $4\sigma \sim 6.2$ mJy. Above this level we detect 8 sources with a spatial resolution of ~ 3000 AU and masses in the ~ $2-18\,M_\odot$ range. The cores are aligned in the E-W direction along a ~ 30000 AU region, with the exception of source i56n-1 (see Fig. 3.2). This follows the distribution hinted from the single-dish observations of Klein et al. (2005), where this region appears elongated in the E-W direction.

The three faint sources i56-2,3 and -5 are located around the brightest source, labeled i56n-4, all of them occupying an area of diameter ~ 10000 AU, and we find that the brightest source is located at the edge of the protocluster.

Sources i56n-4 and i56n-7 have counterparts detected in the NIR K-band by the SINFONI survey (Arjan Bik, *priv. comm.*; see Fig. 3.19). The brightest NIR source in the region is associated with i56n-4, which is the brightest mm source, however it only shows H_2 emission and not [FeII] or Br_γ. This source has also a counterpart in the MSX catalogue, with its strongest emission in the 21.34 μm band. There is a NIR counterpart for i56n-7, but not for i56n-6. This is intersting, since these two sources are only ~ 4000 AU (~ 2″) apart, are apparently sharing a common dust envelope, and have comparable H_2 column densities and masses (see Table 3.4). The presence of this NIR source might then indicate that either i56n-7 is more evolved than i56n-6 or that somehow NIR radiation is leaking from the envelope of i56n-6, perhaps through an outflow cavity. There is in fact a CO outflow associated with this region in the NW-SE direction (Kim & Kurtz 2006; Snell et al. 1988; Xu et al. 2006; Zhang et al. 2005), however the resolution of the observations ($\gtrsim$ 15″) is not enough to determine the driving source. Furthermore, we

---

[4] See footnote in Page 41

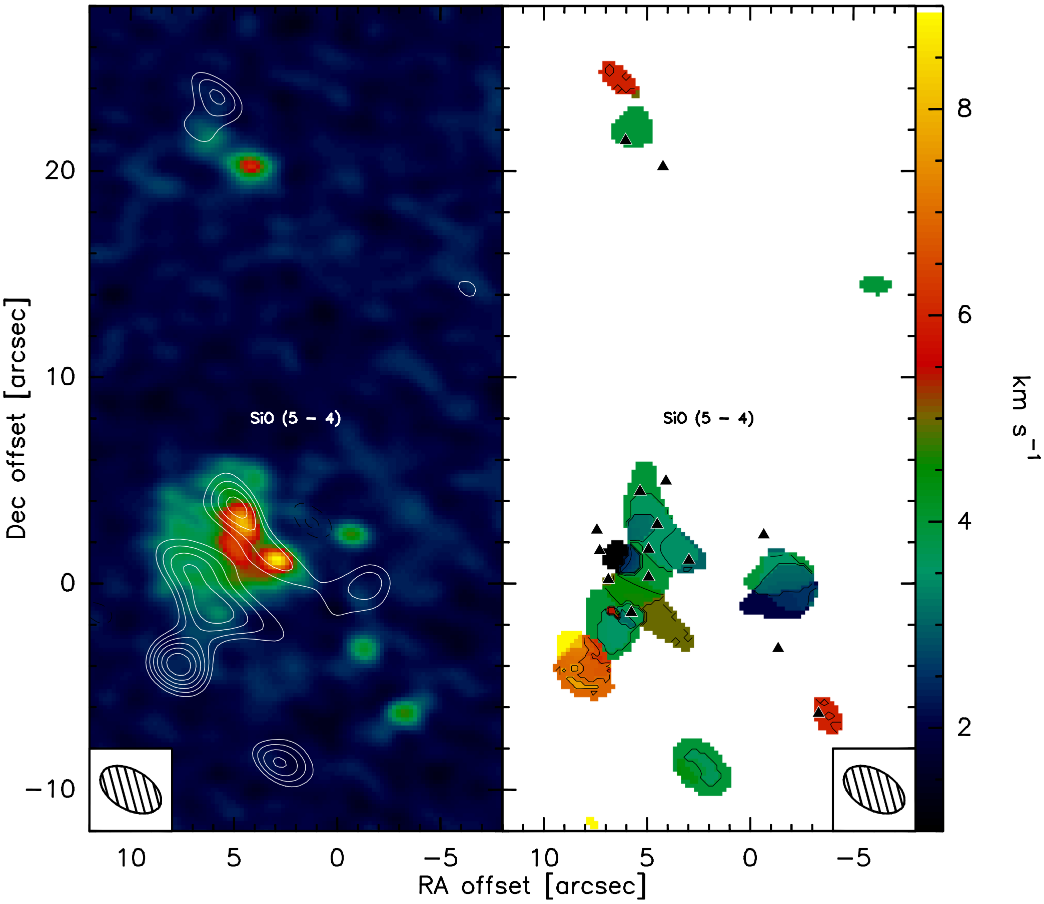

Figure 3.15: SiO maps of IRAS 06058+2138. The left panel shows the zeroth-moment map and the right panel the first-moment map of the SiO (5 – 4) transition. The background in the left panel is the continuum emission (see Fig. 3.3), and the contours is the integrated emission of the line in steps of 10% of the peak intensity, starting at 40%. In the left panel the background shows the intensity-weighted velocity, with contours in 0.5 km s^{-1} steps. The triangles mark the continuum sources detected, and the beam appears at the bottom of each panel. There is a possible outflow in the SE-NW direction. The rest velocity is V$_{\rm lsr}$ ~ 3 km s^{-1}.

do not detect SiO emission in the region, which would have helped us to discern whether the NIR emission is caused because i56n-7 is more evolved, or is leaking through an outflow cavity. Several other nearby NIR sources are detected by SINFONI and can be seen in Fig. 3.19, most likely members of the small NIR star cluster associated with this region (Carpenter et al. 1995a).

There is no other known association for this source. There are no masers, radio sources or HII regions described in the literature, in overall not showing any of the typical signposts of massive star formation. However, the strong emission in the K-band, the lack of Br$_\gamma$ emission and the molecular outflow suggest that the forming stars are very young and still embedded.

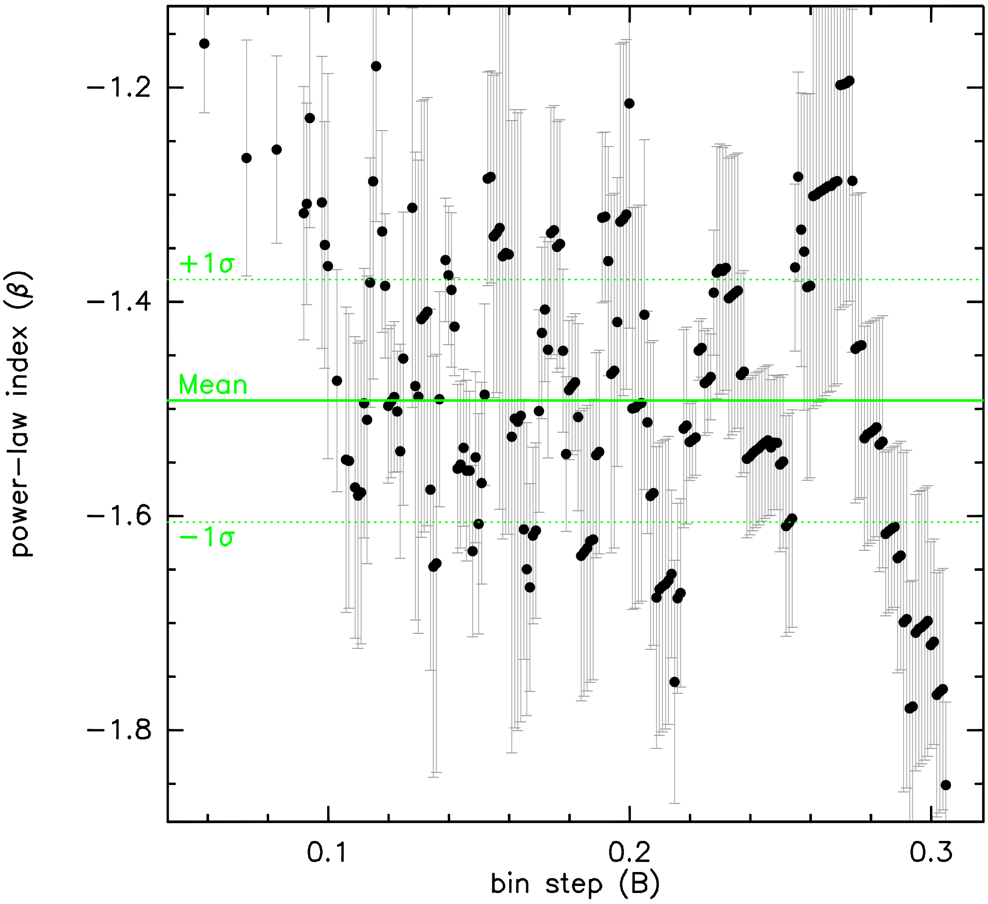

Figure 3.16: Obtained power-law index β_B for the different binnings B. Marked are the weighted-average β value obtained (green solid line) and its $\pm\sigma$ interval (green dotted lines).

IRAS 06056+2131-S

Here we detect 13 sources above the $4\sigma \sim 9.0$ mJy detection threshold, linearly distributed along $\sim$ 40000 AU in the NE-SW direction. The single-dish map of IRAS 06056+2131-S in Klein et al. (2005) do not show any defined structure, however a molecular-gas bridge connecting the southern and northern clumps is seen, extending in the NE-SW direction (see Fig. 3.1).

The sources have masses between $\sim$ 3 and $\sim$ 24 $M_\odot$, and are mainly distributed in three "protostellar systems" labeled i56s-A, i56s-B and i56s-C in Fig. 3.2. Within each of these protosystems the cores have a mean separation of $\sim$ 4000 AU, below the map spatial resolution of $\sim$ 2400 AU, and the protosystems themselves are separated about $\sim$ 10000 from each other. The continuum in each protosystem is dominated by one or two main sources, with the other cores located around them. In this case, the brightest source in the region, labeled i56s-7 is located roughly at the center of the protocluster.

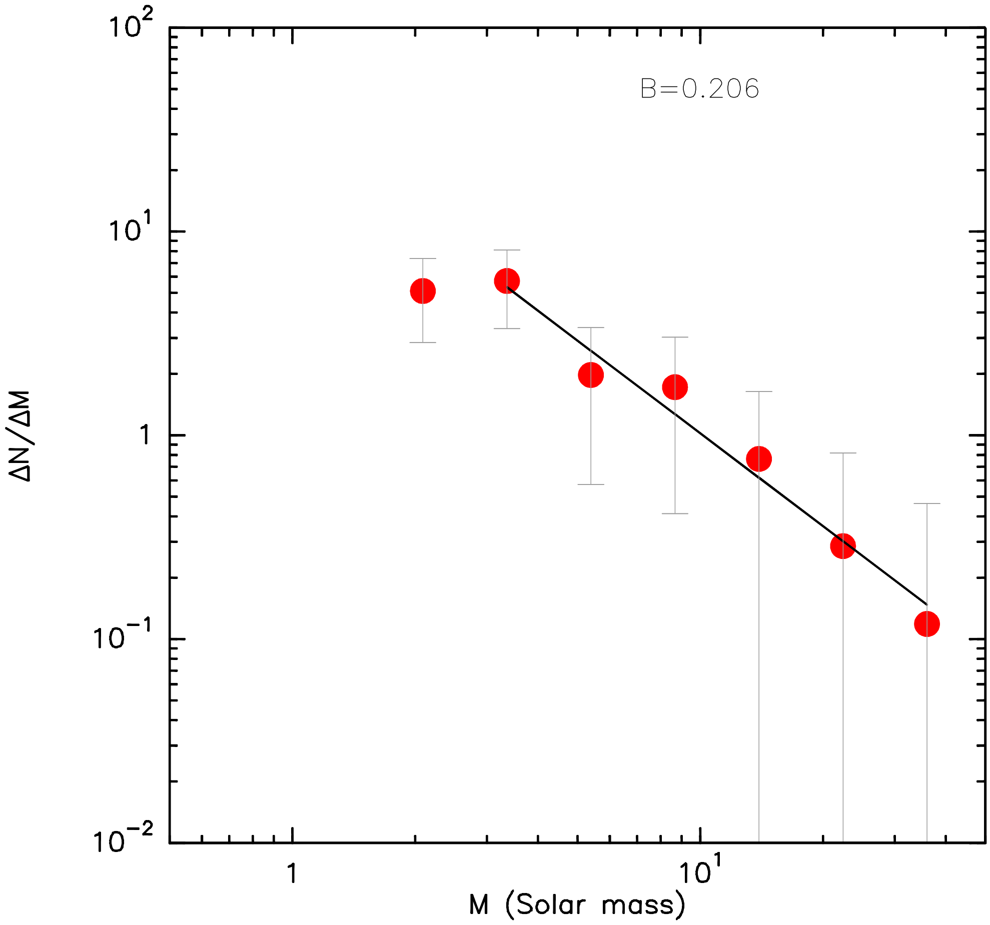

Figure 3.17: Example of the obtained CMFs, corresponding to $B = 0.206$. The solid line is the best fit for core masses above ~ 2.5 $M_\odot$, with a power-law index $\beta = -1.5 \pm 0.1$.

In the NIR, SINFONI only detects a counterpart for i56s-6, also matching within pointing accuracy to the position of a strong MSX source. SINFONI shows that its spectrum is extremely red, also showing Br_γ emission lines (A. Bik, *priv. comm.*). The NIR emission at that position has a diffuse component elongated towards the SE resembling an outflow cavity (see Fig. 3.20). There is in fact a known CO outflow in this region aligned in that same direction, (Kim & Kurtz 2006; Xu et al. 2006; Zhang et al. 2005), but from the SiO emission is more likely to be driven by source i56s-2 (see Fig. 3.14). The other SiO feature detected is associated with i56s-B and hints to an outflow in the NE-SW direction, i.e. perpendicular to the NIR emission, which suggests the outflow-cavity hypothesis is less likely to be the source of the diffuse NIR emission. On the other hand, all the other mm sources do not have infrared counterparts. The IRAS source that gives its name to the IRAS 06056+2131 region is associated with this southern clump, and it is also associated with the NIR cluster GL 6366s (e.g., Hanson et al. 2002).

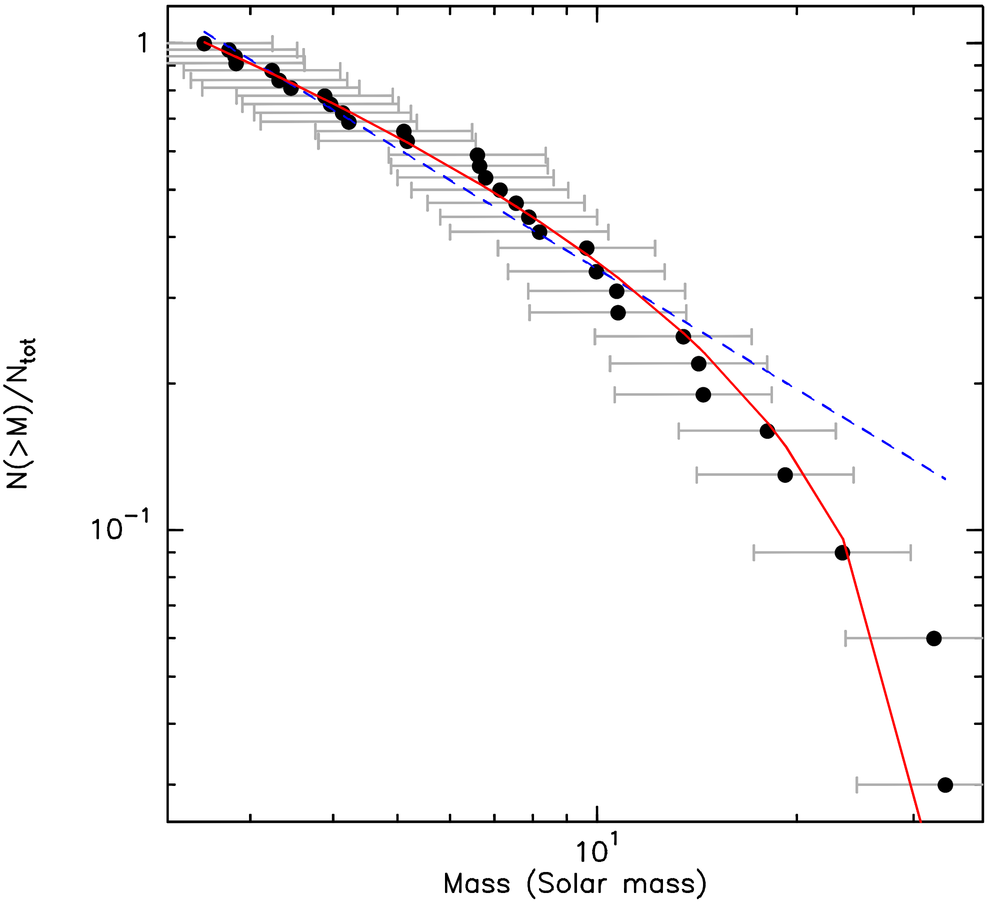

Figure 3.18: Combined cumulative CMF of IRAS 06056+2131 and IRAS 06058+2138 for core masses above 2.5 $M_\odot$. The solid red line and the dashed blue line represent the best fit of Eqs. (2.6) with a power-law index $\beta = -1.4 \pm 0.1$ and (2.5) with $\beta = -1.8 \pm 0.1$, respectively. Note that we have normalized $N(> M)$ by the total number of cores N_{tot}.

An ultracompact HII region is associated with source i56s-2, which shows a compact and unresolved radio source, with a flux $S_\nu \sim 0.7$ mJy at 3 cm and estimated to be ionized by a B3 star (Kurtz et al. 1994). There is also a fainter 3 cm source at the position of i56s-4.

It is noticeable that from the 3 identified protosystems, the one associated with the NIR emission (protosystem i56s-B) is the one that shows less molecular line signatures, with just a detection of a possible outflow in SiO but no detections of DCN, methanol or formaldehyde. On the other hand, the protosystem i56s-A shows strong emission in H_2CO and DCN, and is associated with the strongest SiO feature in the region and the only known radio source. Also, i56s-2 would account for $\sim 30\%$ of the luminosity of the region since it is associated with a B3 star. All this seems to suggest that source i56s-6 is the oldest in the region and most likely not a massive star, while source i56s-2 would be the second older, with an already ignited intermediate-to-high mass star. The other mm sources would be the youngest, and in particular the bright mm source i56s-7 would have the potential to form a massive star.

Saito et al. (2008) traces several $C^{18}O$ cores at ~ 2.7 mm in this region. Sources i56s-11 and i56s-13 are associated with Cores B and C of their work, respectively, while Core J is associated with the protosystem i56s-A and of this work, peaking at the same position as our eastmost DCN feature (see Fig. 3.10-b). Their strongest emission, labeled Core E, peaks between sources i56s-8 and i56s-10, at the same position of our westmost DCN feature.

This southern clump also harbors the only maser emission detected towards the IRAS 06056+2131 region. Caswell et al. (1995) reports the detection of one 6.6 GHz methanol maser, however we do not detect methanol at 1.4 mm (~ 218.2 GHz).

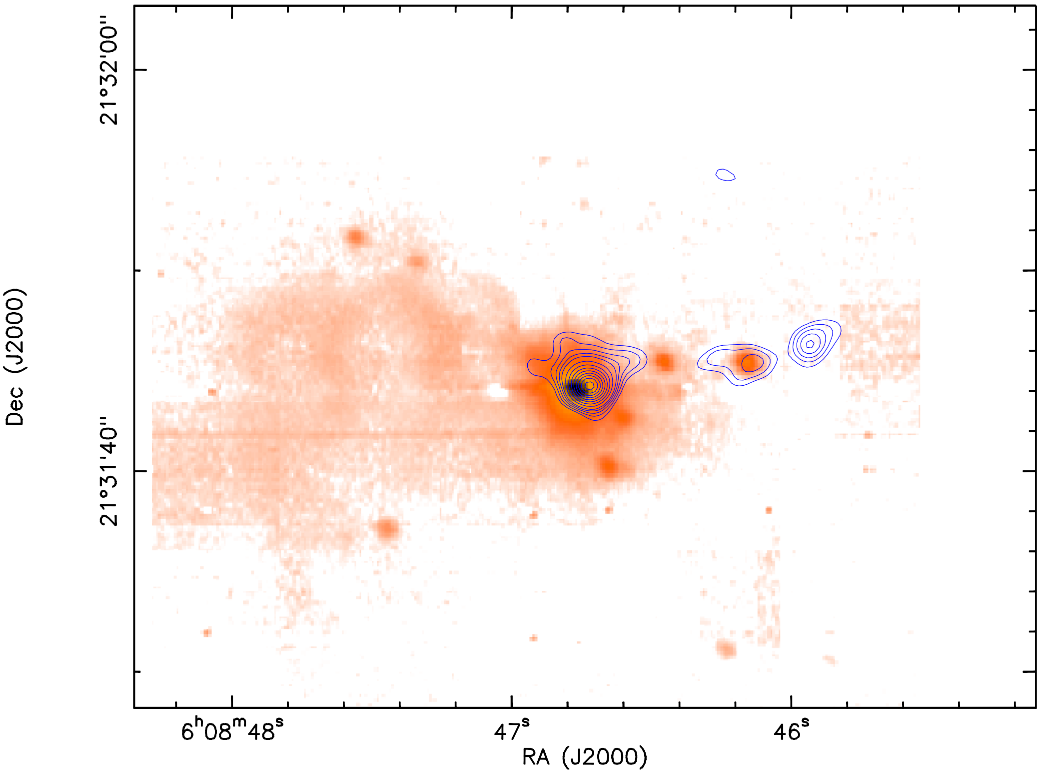

Figure 3.19: SINFONI K-band NIR map (background) of IRAS 06056+2131-N (Arjan Bik, *priv. comm.*). The contours are the mm continuum presented in this work (see Fig. 3.2).

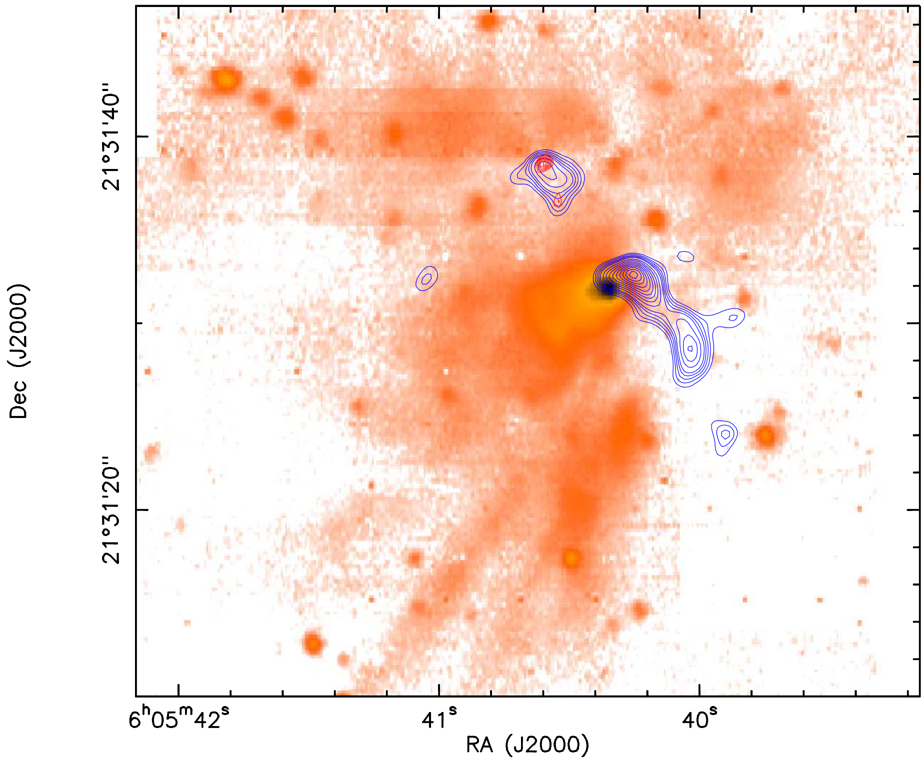

Figure 3.20: Composite map of IRAS 06056+2131-S. The background is the SINFONI K-band NIR map (Arjan Bik, *priv. comm.*), blue contours are the mm continuum presented in this work (see Fig. 3.2) and red contours are the 3.6 cm emission from Kurtz et al. (1994).

IRAS 06058+2138

The morphology of the continuum emission in this region is different to the others. Of the 15 sources identified above the $4\sigma \sim 9.1$ mJy detection threshold with a $\sim$ 2200 AU spatial resolution, 10 are located in a region about $\sim$ 15000 AU in diameter. Fig. 3.3 shows that this region is dominated by two cores, labeled i58-5 and i58-7, of roughly the same brightness located at the edge of the protocluster. The other 5 sources detected are isolated, with no continuum emission connecting them with the main emission region. Of those 5 isolated cores sources i58-10,11 and i58-12 have similar angular size and brightness, while the remaining two sources, labeled i58-1 and i58-2, are located $\sim$ 14000 AU to the north of the main continuum emission.

Single-dish maps in Klein et al. (2005) for IRAS 06058+2138 shows that the continuum emission is slightly elongated in the N-S direction. We find the same overall morphology in the interferometer continuum.

There are two NIR sources associated with our mm emission. Sources i58-2 and i58-5 corresponds to sources SNIR 1 and SNIR 5 from Tamura et al. (1991), detected in the K-band.

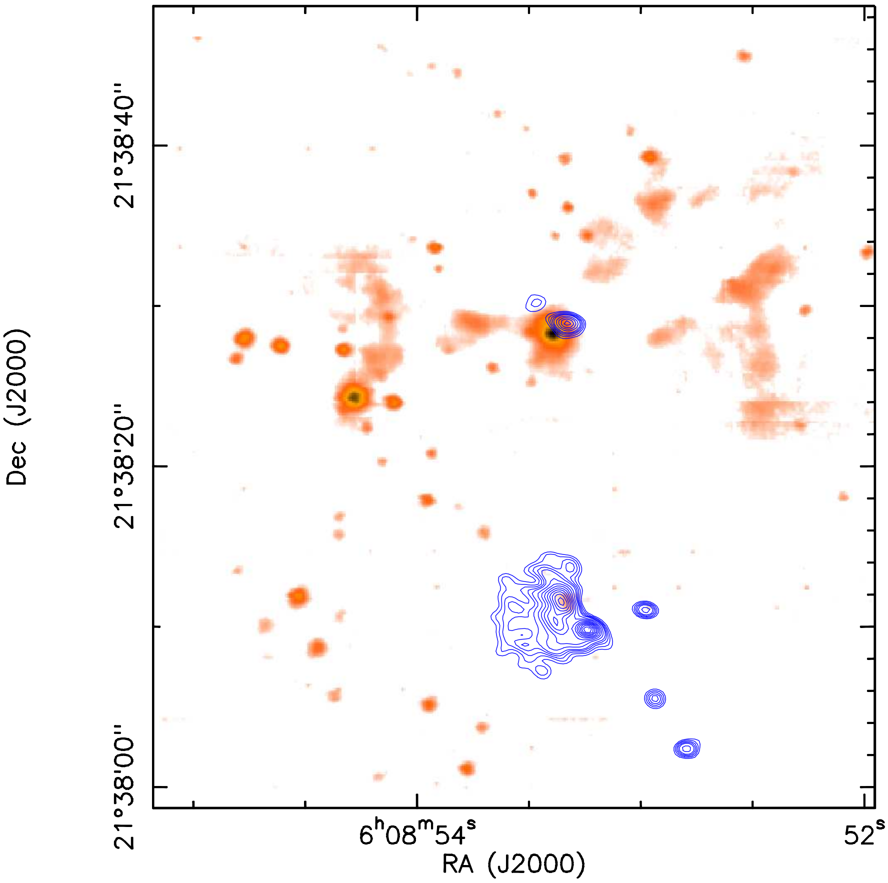

Figure 3.21: SINFONI K-band NIR map (background) of IRAS 06058+2138 (Arjan Bik, *priv. comm.*). The contours are the mm continuum presented in this work (see Fig. 3.3).

However, in the SINFONI data there is only K-band continuum towards SNIR 1, while at the position of SNIR 5 it only detects a H_2 emission feature. Source i58-2 has also a MIR counterpart. Along with i58-1 they are detected at 7.9 μm, 8.8 μm, 11.6 μm, 12.5 μm and 18.5 μm by Longmore et al. (2006). Furthermore, i58-2 is resolved into 3 MIR sources, with mean separations of $\sim$ 1700 AU.

The region is next to the rich NIR protocluster AFGL 5180 with about $\sim$ 63% – 80% of YSOs (Devine et al. 2008; Hodapp 1994; Lada & Lada 2003; Leistra et al. 2006), but with the exception of sources i58-1 and -2, the mm emission is located in an obscured area in the NIR and MIR and separated more than 10″ from any NIR or MIR source. H_2O masers are detected for i58-2 and i58-5. Source i58-2 is also associated with a methanol maser (Minier et al. 2005; Tofani et al. 1995), and there is no radio emission towards this region (Kurtz et al. 1994; Moffat et al. 1979). These signatures characterize this region as an active star-forming region, and based on this Klein et al. (2005) classified IRAS 06058+2138 as a “pre-protocluster” candidate, i.e., a region where massive stars have begun to form deeply embedded, but have not yet cleared a cavity.

On the other hand, IRAS 06056+2131 is classified as a “young cluster” by Klein et al. (2005), a stage where the cluster has emerged from its parental cloud but has not yet dispersed said cloud. This is in line with the studies of Ghosh et al. (2000), who also suggests that IRAS 06058+2138 is the youngest of the three regions IRAS 06056+2131, IRAS 06058+2138 and IRAS 06061+2151 (described in Sec. 3.5.1).

The three cores i58-10, 11 and -12 are interesting in that they do not show any hint of sub-structure and are rather spherical (though marginally resolved), and are located more or less isolated, several thousands AU from the closest neighbor. Of these three cores, i58-11 is the only one that do not show any molecular line signature. The other two cores are associated with $CH_3OH\,(4_{2,2} - 3_{1,2})$, H_2CO and/or SiO (5 – 4) features. Within our uncertainty, the three cores have similar masses, although i58-11 is slightly less massive. These cores are likely forming an intermediate-mass star, or a system of low-mass stars, as is the case of i58-2.

The outflow component in IRAS 06058+2138 is not clear. Snell et al. (1988) mapped the region in CO and found evidence of an outflow, but only its blueshifted component could be clearly identified since the redshifted wing suffered from contamination from the molecular cloud associated with the neighboring Hii regions S252-258. In addition, Davis et al. (1998) mapped the region in H_2 at 2.12 μm and found two chains of knots he suggests may be related to two different outflows, one in the N-S direction and the other in the SE-NW direction. We detect redshifted SiO emission extending from the main sources towards the SW. The apparent direction of this emission is $\sim 45^\circ$ apart from the line of the H_2 knots, therefore an association seems unlikely. There is, however, an H_2 emission feature at the position of i58-5 that might be related to the SiO outflow.

IRAS 06061+2151

The IRAS 06061+2151 continuum emission is dominated by the single bright source i61-1, with a diameter ~ 10000 AU and presenting no structure, despite having a spatial extension over ~ 3 times the synthesized beam. Two fainter sources can be seen in Fig. 3.4 around i61-1, with a mean separation of ~ 6000 AU from it. The remaining fourth core is isolated and located ~ 25000 AU from the main source. All the 3 fainter cores have similar peak intensities, and are a factor 10 fainter than the main source.

This region is associated with the NIR cluster AFGL 5182. There are five 2MASS sources within a few arcseconds from the main mm peak, and Anandarao et al. (2004) have identified all of them as early B-type massive (proto)stars. Those NIR sources can be seen in the SINFONI map shown in Fig. 3.22, where it can be clearly seen that the main mm source, labeled i61-1, is located between two of the NIR sources.

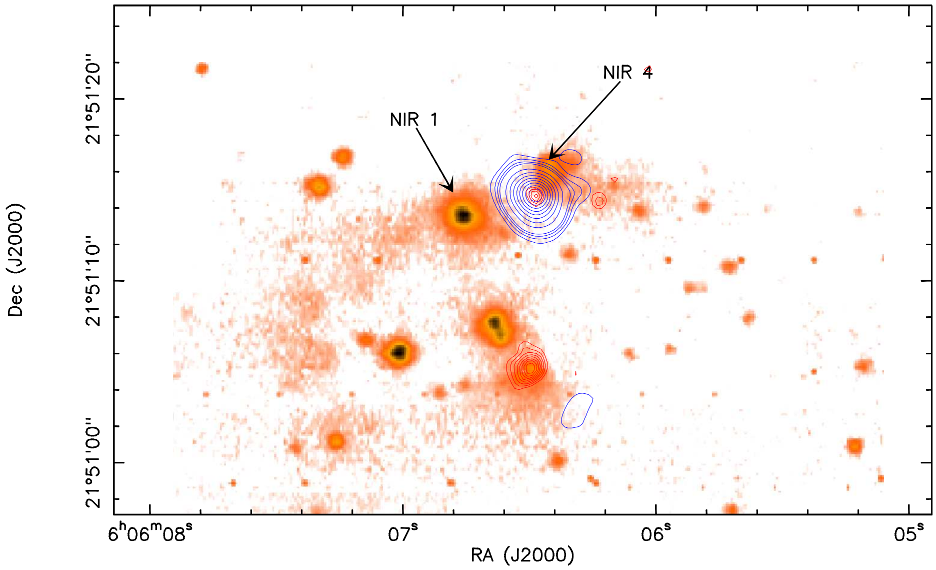

Figure 3.22: Composite map of IRAS 06061+2151. The background is the SINFONI K-band NIR map (Arjan Bik, *priv. comm.*), blue contours are the mm continuum presented in this work (see Fig. 3.4), and red contours are the 3.6 cm emission from Kurtz et al. (1994). The arrows mark the two NIR sources aligned with the H_2 knot chain detected by Anandarao et al. (2004) (see text).

In this region we identify 4 cores, of them i61-1 being the largest and brightest by far. With $\sim 50\,M_\odot$ is the most massive core detected in the 4 regions of this study. Saito et al. (2008) detects a $C^{18}O$ core of diameter $\sim$ 15000 AU with its emission peak at the same position as i61-1. This core encompasses sources i61-1, 2 and -3, and confirms the compact nature of i61-1.

This source has also a weak radio counterpart at 3.6 cm and is marginally detected at 2 cm (Kurtz et al. 1994), indicating the presence of an ultracompact HII region and the ongoing formation of an intermediate-to -high mass star. On the other hand, the weaker continuum feature i61-4 is probably related to a $C^{18}O$ core, supporting its identification (“M” in Saito et al. 2008).

The outflow component in the region is uncertain. Kim & Kurtz (2006) finds CO emission towards the region but not an outflow. However, Anandarao et al. (2004) detect H_2 knot-like features suggesting the presence of a collimated jet in the SE-NW direction, in line with two of the NIR sources (marked with arrows in Fig. 3.22) and also with i61-1. Furthermore, these sources are located roughly in the middle of the projected distance between the H_2 features. Based on the evolutionary stage of the NIR sources, Anandarao et al. suggest that one of them might be the driving source. Source i61-1 is clearly in an earlier evolutionary stage so it is also a likely candidate to be the driving source of the jet. However, we do not detect any SiO signature, therefore it is not so certain whether this may be the driving source of the jet.

IRAS 06063+2040

IRAS 06063+2040 is dominated by a single source, a factor ~ 2 brighter than the other 3 cores detected in this region. It can be seen in Fig. 3.5 that the 3 fainter sources are arranged in an arch-like shape about ~ 20000 AU from the main source.

This region is located within the rich NIR cluster AFGL 5183 (see e.g., Kumar et al. 2006), however none of the mm cores have a NIR counterpart (see Fig. 3.23). Qin et al. (2008) mapped the CO emission in the region and found a large-scale outflow in the N-S direction, but its projected axis is offset from any of the mm sources. Furthermore, we do not detect any SiO signature in the region.

There is no reported radio emission in the region. In addition, OH maser surveys do not detect any H_2O, methanol or OH masers emission (Edris et al. 2007; Sunada et al. 2007).

There is none of the typical signatures of massive star formation, furthermore, the continuum emission show cores of relatively low masses. All this suggest that the these cores are not forming massive stars.

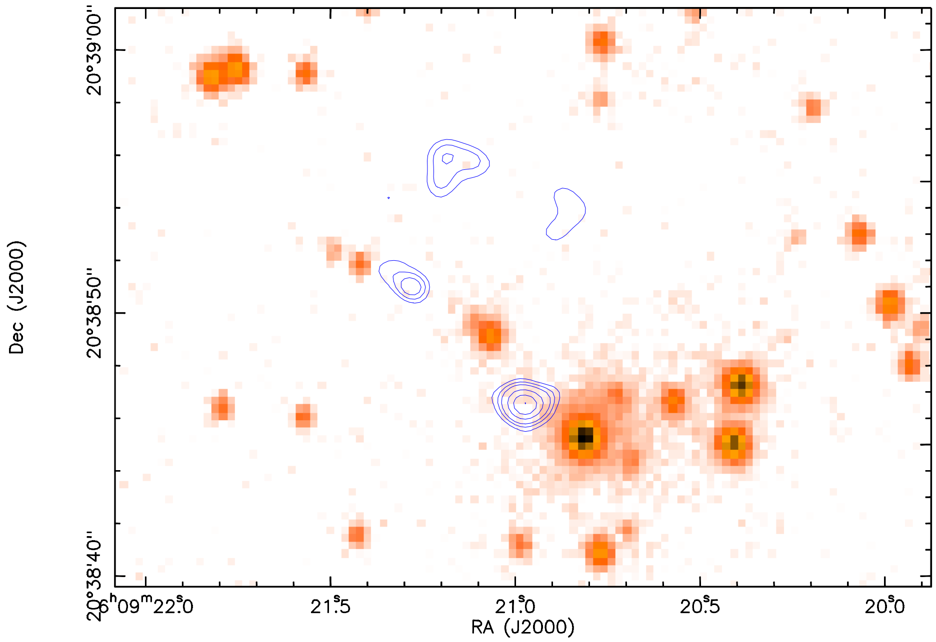

Figure 3.23: Composite map of IRAS 06063+2040. The background is the NTT K-band NIR map (Arjan Bik, *priv. comm.*), and the blue contours are the mm continuum presented in this work (see Fig. 3.5)

3.5.2 The CMF

The results of Sec. 3.4 shows us a CMF with a slope $\beta \sim -1.5 \pm 0.2$. This is a relatively flat slope, if we compare with the results of Sec. 2.3.2 where the CMF resulted with a slope $\beta \sim -2.3 \pm 0.2$, similar to the Salpeter value for the stellar IMF.

The CMF's slope we obtain now is comparable to the slope of the Clump Mass Functions (ClMFs), for which a slope of ~ -1.6 is found (e.g. Kramer et al. 1998; Kerton et al. 2001; Muñoz et al. 2007). Those ClMFs are obtained with CO emission maps for structures of sizes on the order of $\sim$ 0.1 pc. Going to at least one order of magnitude better in spatial resolution, and based in our previous results (Sec. 2.3.2, Beuther & Schilke 2004), we were expecting a steepening of the slope. This would signal further fragmentation at smaller spatial scales since large, massive structures would resolve into several smaller, less massive ones, therefore depopulating the higher-mass end of the mass function while at the same populating its lower-mass end.

Single-dish maps of regions IRAS 06056+2131 and IRAS 06058+2138 at spatial scales of clumps show only a single clump where we find several fragments (see e.g. Klein et al. 2005; Saito et al. 2007). We are indeed seeing further fragmentation in the regions, but apparently the CMF does not reflect that fragmentation.

The procedure used to obtain the CMF is the same we used for IRAS 19410+2336. The only difference is that in that case we were able to estimate the temperatures of the individual cores and thus refine the mass calculations. As explained earlier, for the regions in this Chapter we currently cannot make a temperature determination since we do not have the complimentary single-dish observations of the formaldehyde lines yet, that is the reason why we used the average IRAS temperatures from the literature. A change in the core's temperature has the possibility of making the CMF slope steeper. We already saw for IRAS 19410+2336 that it is more likely that the brightest cores are warmer than the average temperature in the region, while the fainter cores have a temperature similar to the average value. A higher temperature for the brightest cores will lower their masses and if at the same time the fainter cores do not change their temperature, the CMF will become steeper. Nevertheless, for IRAS 19410+2336 we also found that knowing the temperature structure of the region did not change the result significantly (see Sec. 5.1 for further discussion). In that case we obtained the same value for the CMF slope as the previous study of the region (Beuther & Schilke 2004), where the average IRAS temperature of the region was used. Therefore, although is a plausible explanation of why the slope is now flatter, using average temperatures for the calculation of the masses likely do not change the result.

Having merged the regions IRAS 06056+2131 and IRAS 06058+2138 in one single sample to be able of calculating a differential CMF is also not the reason of the slope being flatter. In Fig. 3.24 we show that the cumulative CMF of regions IRAS 06056+2131 and IRAS 06058+2138 have the values $\beta \sim -1.6\pm0.2$ and $\beta \sim -1.7\pm0.2$ for the slope of the differential CMF, respectively. Within the uncertainties this two results are indistinguishable between them and between them and the $\beta \sim -1.4 \pm 0.1$ obtained for the combined sample.

This suggests that the fragmentation processes in both regions are intrinsically similar and whatever is affecting such processes, thus making the combined CMF slope flatter, would be affecting both regions in a similar way, having a comparable effect on them.

Simulations of the evolution of molecular clouds show that if the dynamical evolution is dominated by gravity, then the slope of the mass spectrum becomes flatter (Klessen 2001). In the case of pure gravitational contraction, i.e., the cloud is gravitationally dominated, the slope is

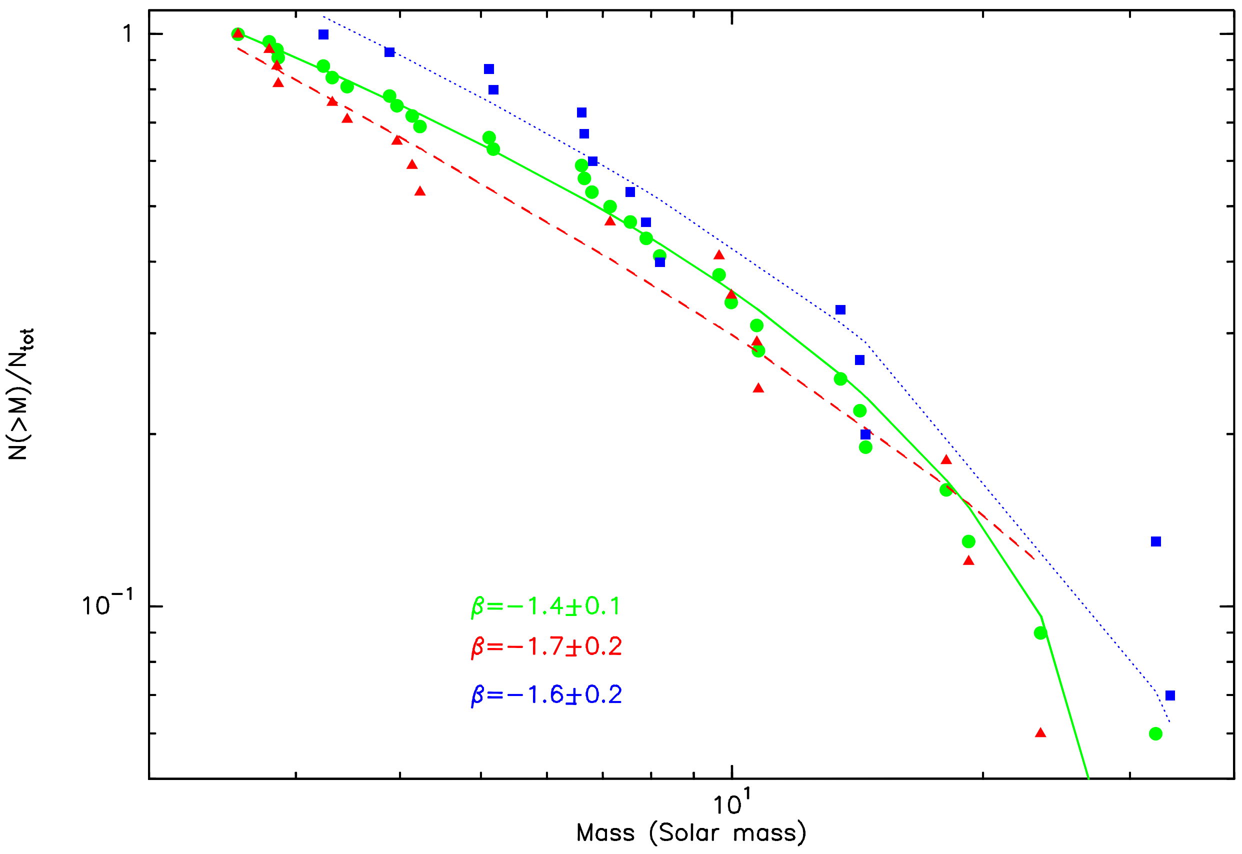

Figure 3.24: Comparison between the cumulative CMFs of regions IRAS 06056+2131 (red triangles) and IRAS 06058+2138 (blue squares), and the cumulative CMF of the combined sample obtained in Sec. 3.4.2 (green circles). The solid, dashed and dotted lines are the best fit to Eq. 2.6. for the combined data, IRAS 06056+2131 and IRAS 06058+2138, respectively. The different slopes and their standard deviations are shown in the same color code.

$\beta \sim -1.5$, while when the cloud is supported by turbulence the slope is $\beta \lesssim -2$. On the other hand, during their early collapse the clouds are gravitationally dominated and then during their evolution the feedback from the forming stars, e.g., stellar winds and molecular outflows, injects energy, and hence turbulence, into the forming cloud. Following this, it could be possible that at early evolutionary stages, while the cloud is mainly gravitationally supported, the mass function will have a shallow slope, that will "evolve" into a steeper distribution as the cloud itself evolves. This would suggest that the slope of the mass function could be indicating the relative age of the cloud, the flatter it is the younger the cloud is.

In our case, it is suggested in the literature that IRAS 06058+2138 is somewhat younger that IRAS 06056+2131 (Ghosh et al. 2000; Klein et al. 2005), however is not so clear that IRAS 06056+2131 is in turn younger than IRAS 19410+2336. In Sec. 2.4.1 we showed that IRAS 19410+2336 has several NIR and MIR identified counterparts, as well as a cm source associated with its most massive core and several H_2O and methanol masers. The region also has a very energetic and active outflow component, with multiple CO outflows detected with a spatial resolution of ∼ 7500 AU (Beuther et al. 2003). On the other hand, in Sec. 3.5.1 we mention that IRAS 06058+2138 has only one NIR and MIR counterpart and are not associated with the brightest mm source. The region also has a cm counterpart, but is associated with the more isolated protosystem we recover. There are only two outflows detected, although at larger scales than for IRAS 19410+2336, however our SiO observations only detect weak emission in the southern part part of the region. As for maser emission, only one methanol maser is associated with IRAS 06056+2131.

The apparently weaker outflow component, less NIR emission and cm emission from the main mm sources hints to the possibility that IRAS 06056+2131 might be younger than IRAS 19410+2336. However, this is not conclusive at all. Further observations would be needed to assert a difference in age, as for example high-resolution interferometric CO maps to look for smaller scale outflow activity, or MIR imaging with MIPS and/or PACS and SPIRE onboard the Herschel Space Observatory. If indeed IRAS 06056+2131 is younger than IRAS 19410+2336, it would then explain the difference in the slope of their CMFs.

Another possible indicator of the relative ages are deuterated species. It is believed that the deuterium fractionation can be used as an indicator of the evolutionary state of a molecular core, for example, Crapsi et al. (2005) propose that among other factors, the $N\left(N_2D^+\right)/N\left(N_2H^+\right)$ ratio can be used to identify potential starless cores. In general, a higher deuterium fractionation would signal an earlier evolutionary stage (e.g., Caselli et al. 2002c,a; Crapsi et al. 2005; Fontani 2008; Fontani et al. 2009). At earlier and colder evolutionary stages, deuterium will accrete onto grain surfaces producing deuterated species. Then, as the temperature in the medium increases those deuterated species start to evaporate into the gas as temperatures raise, increasing the observed deuterium fractionation. Later, as this gas-phase deuterium is being destroyed, the fractionation starts to decline, signaling a more advanced evolutionary stage (e.g., Caselli et al. 2002b; Ceccarelli et al. 2001; Charnley 1997).

We detect the deuterated species DCN in IRAS 06056+2131 and IRAS 06058+2138, which indicates that indeed are in an early evolutionary stage, but we would need observations of HCN and other deuterated species as for example HDCO and N_2D^+ and the correspondant hydrogenated isotopologues, to attempt to determine a relative age between the regions.

All the regions involved have similar masses, luminosities and distances. There is, however, the difference that IRAS 19410+2336 is in the inner galaxy, with an angular separation of $\sim 60°$ from the galactic center ($l = 59°46'52''; b = 0°3'44''$), while IRAS 06056+2131 and IRAS 06058+2138 are in the outer galaxy, about $\sim 130°$ to the east of IRAS 19410+2336. According to Kalberla & Dedes (2008) there is an exponential volume density gradient in the Galactic disk towards the outer Galaxy, with a radial scale-length of 3.15 kpc. The distance between IRAS 06056+2131/IRAS 06058+2138 and IRAS 19410+2336 is of about $\sim$ 4 kpc, meaning a volume density decrease by a factor $\sim$ 3.6. We in fact detect an average volume density difference. Using the reported single-dish column densities in Klein et al. (2005) and Beuther et al. (2002b) togheter with Eq. (2.1) we obtain that the average volume density of IRAS 19410+2336 is between $2 - 5$ times higher than for IRAS 06056+2131 and IRAS 06058+2138. This difference in turn implies that the Jeans scale in IRAS 19410+2336 would be a factor $\sim$ 2 smaller than for the other two regions, and will likely favor the formation of more massive cores in IRAS 06056+2131 and IRAS 06058+2138. Although this will result in an overall shift of the mass function towards higher masses, a priori does not indicate if the slope will become shallower or steeper, if it does necessarily change at all. Simulations of the fragmentation of similar initial molecular clouds but with different average volume density should be made, to see if there is a clear relationship between the slope of the resulting CMF and the density.

Other theories that might explain this difference in the slope of the CMF are proposed by Elmegreen (2006). For instance, different star formation processes. Strong interactions between the cores could make the stellar mass function different from the CMF, while weak interactions might keep them about the same. Also, simulations show that hierarchical fragmentation alone produces a mass function with a slope $\beta \sim -2$. Now if the IMF comes mostly from fragmentation, regardless of the origin of that fragmentation, then if there are physical processes favoring the formation of massive cores then the slope will be flattened at high masses. Such processes might include the ablation of low-mass protostars, heightened accretion, coalescence and multiple-star interactions.

In the end, it is not clear why we are obtaining a CMF distribution flatter than for IRAS 19410+2336. It can be happening for several reasons going from different cloud properties to different star-formation scenarios, or just be reflecting a difference in age betwen the regions. In all cases, further observations and numerical simulations are needed to help determine a reason.

3.6 Conclusions

We have mapped 4 MSF regions at 1.4 mm with the SMA at spatial scales of ∼ 2400 AU, identifying 44 cores in total. Because of their similar properties and apparent common parental cloud, we merged the results for regions IRAS 06056+2131 and IRAS 06058+2138 and produced a jointed CMF with the 36 identified cores from both regions.

From both the differential and the cumulative CMF we obtain a surprisingly shallow slope $\beta \sim -1.5 \pm 0.2$, similar to the typical ~ -1.5 value for the ClMF at scales at least ten times larger, and flatter than the Salpeter value of ~ -2.3 for the IMF. This result is contrasting our result for the region IRAS 19410+2336 discussed in the previous chapter, for which we find a CMF slope similar to Salpeter. Several theories can explain this difference. One possibility, for example, is that we are looking at regions at different evolutionary stage. In any case, with the data we currently have we cannot conclusively determine a reason for why the slope is flatter in this case, and we stress that a different number of observations and numerical simulations can and should be done to obtain an explanation.

We also observed several formaldehyde transitions in an attempt to determine the temperature of the cores in a similar way than for IRAS 19410+2336, however the interferometric data is strongly affected by missing short-spacings and are not reliable to attempt a temperature determination. Complimentary short-spacing observations will be done, nevertheless from the results for IRAS 19410+2336 we do not expect a significant change in the resulting CMF.

The protostellar content of the regions is discussed. We show recent NIR observations of this regions obtained by A. Bik, E. Puga, T. Vasyunina et al. with SINFONI at the VLT, pointing out the importance of a multiwavelength approach in the study of massive star formation.

Chapter 4

W3 IRS5: A Trapezium in the making

The formation of high-mass stars appears to be intimately linked with the formation of multiple stellar systems. Optically visible OB-type stars show a much higher degree of multiplicity than their lower-mass counterparts (Preibisch et al. 1999). Now observations are showing that such high-mass multiple systems have separations ranging between 10000 AU and 1 AU, and appear to be bound groups within larger clusters (Mermilliod & García 2001). In contrast to hierarchical systems where the successive separation between its members increases by large factors, many of these systems are dynamically unstable, nonhierarchical clusters of three or more stars, called trapezia after the Trapezium cluster in Orion. The role such systems play in massive star formation is not yet understood, although several suggestions have been made.

First, the mass density of these multiple systems may be high enough to gravitationally trap hypercompact or even small ultracompact HII regions. Keto (2002a,b, 2003) has shown that continued accretion through the HCHII region may be possible, even after the supporting stars have reached the main sequence. The radius where these HII regions become hydrodynamically supported -thus stopping the accretion flow- scales inversely with the attracting mass, thus massive trapezia systems allow more mass to be accreted to the central accreting objects (Keto 2002a,b, 2003).

Second, binary systems are expected to form in the center of these dense proto-Trapezia. These binaries will continue accreting gas, funneled to the center by the combined potential of the protocluster. Because the angular momentum of the infalling gas has no correlation with that of the binary's, the masses of the individual stars increase while the separation of the binary decreases, giving as a natural outcome a high-mass close binary system that could eventually undergo mergers, creating even more massive systems (Bonnell & Bate 2005).

The previous examples show how the formation of massive stars in multiple systems with separations on the order of $\sim$ 1000 AU may be affected by their companions, either by modifying the morphology of accreting envelopes allowing more mass to be accreted, or by forming more massive stars by merging high-mass close binaries.

Some multiple high-mass protostellar systems are known. For example, W 33A was imaged by van der Tak & Menten (2005) at 43 GHz with the Very Large Array finding three continuum sources at separations of 3000 – 5000 AU; Hunter et al. (2006) found similar systems in NGC 6334 I and NGC 6334 I(N) with a few millimetric sources inside a region of $\sim$ 10000 AU. More recently, Beuther et al. (2007b) resolved the central 7800 AU of the hot molecular core G29.96–0.02 into four submillimeter peaks, a potential proto-Trapezium system.

One prime example of a trapezia is the system W3 IRS5 in the W3-Main region of the Hii/molecular cloud complex W3, a very active star-forming region part of the larger star-forming complex W3/W4 located in the Perseus arm of the Galaxy, that also encompasses the W4 star-forming region and the OB associations IC 1805 and IC 1795. In W3 the star formation takes place in the embedded regions W3-Main, W3-North, and W3-OH.

Oey et al. (2005) found evidence supporting the scenario in which the star formation in W3-Main was triggered by the formation of IC 1795, which in turn was triggered by the Perseus chimney/superbubble. This scenario, however, has been brought into question by the recent Chandra X-Ray observations of Feigelson & Townsley (2008), because W3-Main does not show the elongated and patchy structure of a triggered star cluster. W3-Main itself may harbor its own triggered star-formation scenario because the various morphological classes of Hii regions that can be found in it suggest that different stages of massive star formation may be sequentially triggered by the pressure of the expanding Hii regions (Tieftrunk et al. 1997, 1998).

The system W3 IRS5 is a known double infrared (IR) source (Howell et al. 1981; Neugebauer et al. 1982) with a total luminosity of 2×10^5 $L_\odot$ (Campbell et al. 1995), located in the W3-Main region at a distance of 2 kpc (Megeath et al. 2008). Recently, Megeath et al. (2005) presented HST observations with an angular resolution of 350 AU identifying seven near-IR sources including the two previously known. Three of these sources have both mid-IR counterparts and are 1.2 and 0.7 cm continuum sources (Wilson et al. 2003; van der Tak et al. 2005). The sizes of the Hii regions are $<$ 240 AU, indicating that they are probably gravitationally bound and may be accreting (e.g., Keto 2003). Based on its size, the probable masses of the stars, and its nonhierarchical distribution of sources, Megeath et al. (2005) proposed that this system is a proto-Trapezium system, which would emerge as a bound Trapezium similar to that in the Orion nebula. This region is also the source of at least two outflows (Imai et al. 2000; Wilson et al. 2003), and is in the center of an embedded cluster of 80 – 240 low-mass stars (Megeath et al. 1996) which in turn is surrounded by a core of several hundred low-mass stars (Feigelson & Townsley 2008).

4.1 Observations

We have mapped W3 IRS5 with the IRAM *Plateau de Bure Interferometer* (PdBI)[1] in the *A* (Jan/Feb 2006) and *B* (Mar 2006) configurations at 1.4 mm and 3.4 mm imaging the continuum, achieving an angular resolution with a synthesized beam of $0.39'' \times 0.34''$ at 1.4 mm and $1.00'' \times 0.89''$ at 3.4 mm. At the given distance of 2 kpc that translates to a spacial resolution of $\sim$ 700 and $\sim$ 1900 AU, respectively. The $\sim 0.36''$ resolution obtained was feasible because of the new very extended baselines, extending to over 700 m.

The receivers were tuned to 87 and 217 GHz both in the lower sideband. With this spectral setup we observed the SO_2, SiO and $C^{18}O$ transitions described in Table 4.1 with a maximum spectral resolution of $0.5\,km\,s^{-1}$. We adopted a systemic velocity $V_{LSR} = -39\,km\,s^{-1}$ (Ridge & Moore 2001; Tieftrunk et al. 1998). Although observed, $C^{18}O$ was not detected due to the short-spacings problem inherent to the interferometer filtering out the received flux.

The phase and amplitude calibrators were 0355 + 508 and 0059 + 581 and the flux calibrator was 3C 345, adopting the values from the SMA flux monitoring of these quasars. The data were calibrated with the program CLIC and then imaged with the program MAPPING, both part of the GILDAS package. The spectra were processed with the program CLASS77, also from the GILDAS package.

After inversion and cleaning, the continuum data have rms noise levels $\sigma = 1.8\,mJy\,beam^{-1}$ and $\sigma = 1.2\,mJy\,beam^{-1}$ at 3.4 mm and 1.4 mm respectively. For the line data, with a spectral resolution of $0.5\,km\,s^{-1}$ the noise levels are $\sigma = 7\,mJy\,beam^{-1}$ for SiO $(2-1)$, $\sigma = 18\,mJy\,beam^{-1}$ for $SO_2\,(22_{2,20} - 22_{1,21})$ and $\sigma = 8\,mJy\,beam^{-1}$ for $SO_2\,(8_{3,5} - 9_{2,8})$ while SiO $(5-4)$ was imaged with a spectral resolution of $1\,km\,s^{-1}$ resulting in a rms $\sigma = 14\,mJy\,beam^{-1}$ (see Table 4.1).

---

[1] IRAM is supported by INSU/CNRS (France), MPG (Germany) and IGN (Spain).

Table 4.1: Observed molecular transitions and rms of the respective maps.

Transition	ν (GHz)	Spect. Resol. (MHz)	E_{up} (K)	rms[a] (mJy beam^{-1})
SO_2 ($8_{3,5}-9_{2,8}$)	86.64	0.14	55	8.0
SiO (2 − 1)	86.85	0.14	6	7.0
Continuum	87.02	…	…	1.8
SO_2 ($22_{2,20}-22_{1,21}$)	216.64	0.36	248	18.0
Continuum	216.87	…	…	1.2
SiO (5 − 4)	217.10	0.36	31	14.0
$C^{18}O$(2–1)[b]	219.56	…	15	…

[a] For a spectral resolution of 0.5 km s^{-1} except for SiO (5 − 4), whose map has a spectral resolution of 1 km s^{-1}.
[b] Not detected, filtered out by the interferometer.

Table 4.2: Properties of the continuum millimetric sources in W3 IRS5.

MM	R.A. (J2000)	Dec. (J2000)	I_ν[a] (mJy beam^{-1})	S_ν[a] (mJy)	Mass ($M_\odot$) 50 K	 100 K	 200 K	N (H_2)[b] (10^{24} cm^{-2})	A_v (10^3 mag)
1.4 mm with 0.39″ × 0.34″ beam									
1 …	02 25 40.77	62 05 52.49	34.8	70	6.7	3.2	1.6	8.0	8.5
2 …	02 25 40.68	62 05 51.53	20.6	24	2.3	1.1	0.5	4.7	5
3 …	02 25 40.66	62 05 51.95	10.4	13	1.2	0.6	0.3	2.4	2.5
4 …	02 25 40.75	62 05 50.45	5.7	5.7[c]	0.6	0.3	0.1	1.3	1.4
3.4 mm with 1.00″ × 0.89″ beam									
1 …	02 25 40.77	62 05 52.49	23.1	24	83.4	40.1	20.2	30	32
5[d] …	02 25 40.68	62 05 51.85	11.2	11.2[c]	39.0	19.1	9.4	14	15
6 …	02 25 40.73	62 05 49.86	5.1	5.1[c]	17.7	8.7	6.3	6.6	7

[a] The fluxes have been corrected for the free-free contribution, except for source MM4.
[b] Calculated assuming T = 100K.
[c] Unresolved, I_ν given instead of S_ν.
[d] Source MM5 is likely the merged pair MM2 and MM3.

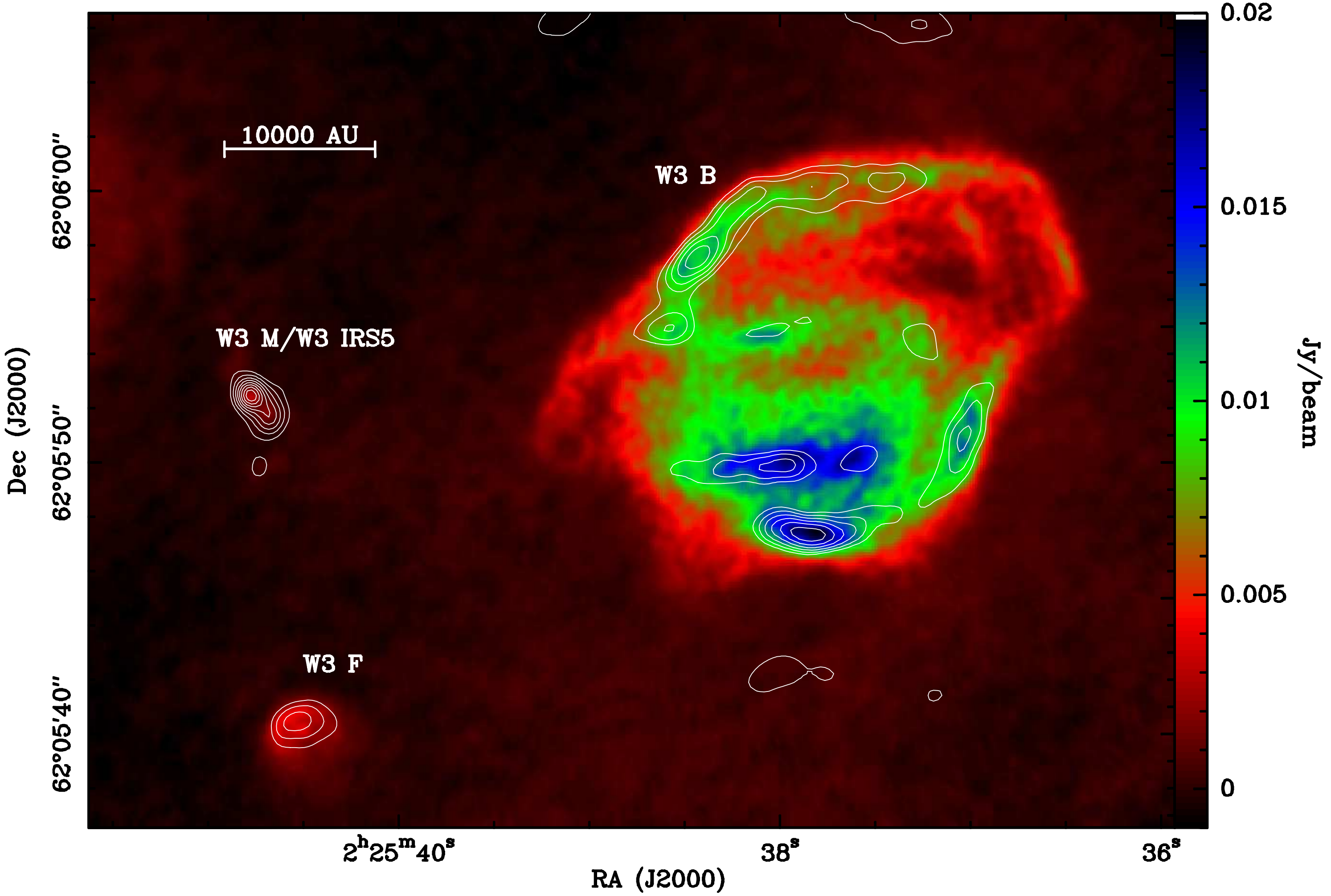

Figure 4.1: Continuum image (greyscale) of the W3 region at 4.9 GHz adapted from Tieftrunk et al. (1997). Contours trace the observed PdBI continuum emission at 3.4 mm, starting at 20% of the peak flux in 10% steps. Shown are the HII regions W3 B (compact), W3 F (ultracompact) and W3 M/W3 IRS5 (hypercompact).

4.2 Results

4.2.1 Large-scale Overview

The W3 complex is a very rich one when it comes to HII regions. Several HII regions have been detected at 6, 2 and 1.3 cm by Tieftrunk et al. (1997), encompassing hypercompact, ultracompact, compact and diffuse HII regions. All of them probably originated from the same volume of neutral gas.

With the ages they estimated, Tieftrunk et al. (1997) suggest a qualitative evolutionary sequence of the HII regions, going from hypercompact to ultracompact, compact and then diffuse. Also the number, age and spatial distribution of the HII regions suggest a scenario of triggered star formation by the expansion of the HII regions that formed first.

In our 3.4 mm map we detected three of those HII regions, the compact W3 B, the ultracompact W3 F and the hypercompact W3 IRS5, also known as W3 M, the subject of our study (see Fig. 4.1). The shell-like structure and overall morphology of W3 B is recovered by our observations, as well as the cometary shape of W3 F.

4.2.2 Millimetric Continuum

Fig. 4.2 shows the 1.4 and 3.4 mm continuum maps, with the six sources detected labeled MM1–6 in descending order of intensity at 1.4 mm for MM1–4 and at 3.4 mm for MM5 and MM6. MM1 is the only source resolved at both wavelengths, while MM4 is detected only at 1.4 mm and MM6 only at 3.4 mm. At the long wavelength we do not resolve MM2 nor MM3. However, based on its position, MM5 is likely the joint contribution from MM2 and MM3 and is not considered an individual source.

The properties of the sources are summarized in Table 4.2. Cols. 2 and 3 give their positions; the measured peak flux intensity and integrated flux density, both corrected for the free-free contribution, are given in Cols. 4 and 5 respectively.

In the standard model of optically-thick (spectral index ~ 2) and optically-thin (spectral index ~ -0.1) free-free emission, the spectral indexes derived by van der Tak et al. (2005) indicate that the 43 GHz emission is close to the “turnover point” between optically-thick and optically-thin free-free emission, and is approximately an upper limit to the free-free contribution at millimetric wavelengths. In HCHII region models with density gradients (e.g., Keto 2003) or clumpiness (Sewilo et al. 2004) the free-free emission may rise somewhat more, but unlikely by a significant amount. Therefore, here we assume that the 43 GHz emission is a good measure of the free-free contribution at millimetric wavelengths and we use it to correct our measured fluxes for such contribution, as shown in Table 4.3. This could be done for all our sources except MM4, for which van der Tak et al. (2005) did not detect a counterpart.

Table 4.3: Contribution of the free-free emission to the measured millimetric fluxes.

MM	Peak Intensity (f-f)		Flux Density (f-f)	
	(mJy beam^{-1})	$\frac{\text{free−free } I_\nu}{\text{measured } I_\nu}^{a}$	(mJy)	$\frac{\text{free−free } S_\nu}{\text{measured } S_\nu}^{a}$
1.4 mm with 0.39″ × 0.34″ beam				
1 . . .	2	0.05	2	0.03
2 . . .	2	0.09	4	0.14
3 . . .	2	0.16	3	0.19
3.4 mm with 1.00″ × 0.8″ beam				
1 . . .	2	0.08	2	0.08
5 . . .	4	0.26	4^{b}	0.26^{b}
6 . . .	0.7	0.12	0.7^{b}	0.12^{b}

Because the brightness temperature of the corresponding Planck function for the strongest source –MM1– is about 11 K, just ∼10% of the typical hot core temperatures of ∼100 K, we can assume that the emission comes from optically thin dust and thus calculate the masses and column densities with the approach outlined by Hildebrand (1983) and adapted by Beuther et al. (2002b, 2005). We adopted a distance of 2 kpc (Megeath et al. 2008) and used a grain emissivity index $\beta = 2$, corresponding to a dust opacity per unit mass $\kappa_{3.4mm} \sim 0.05$ and $\kappa_{1.4mm} \sim 0.3\,\mathrm{cm^2\,g^{-1}}$ for a median grain size $a = 0.1\,\mu$m and grain mass density $\rho = 3\,\mathrm{g\,cm^{-3}}$. In Cols. 6–8 and 9 of Table 4.2 are the calculated masses and H_2 column densities respectively. We did not derive a temperature for this region, therefore the masses were calculated assuming the different temperatures T ∼ 50 K, T ∼ 100 K and T ∼ 200 K, while for the N(H_2) calculation we assume a hot core temperature of ∼ 100 K.

The obtained masses are strongly affected by the spatial filtering inherent to interferometers. Comparing with single-dish data (van der Tak et al. 2000b) we recover only ∼ 9% of the flux at 1.4 mm (see Sec. 4.3.1 for further discussion). The visual extinctions in Col. 10 were calculated assuming $A_v = N(H_2)/0.94 \times 10^{21}$ (Frerking et al. 1982).

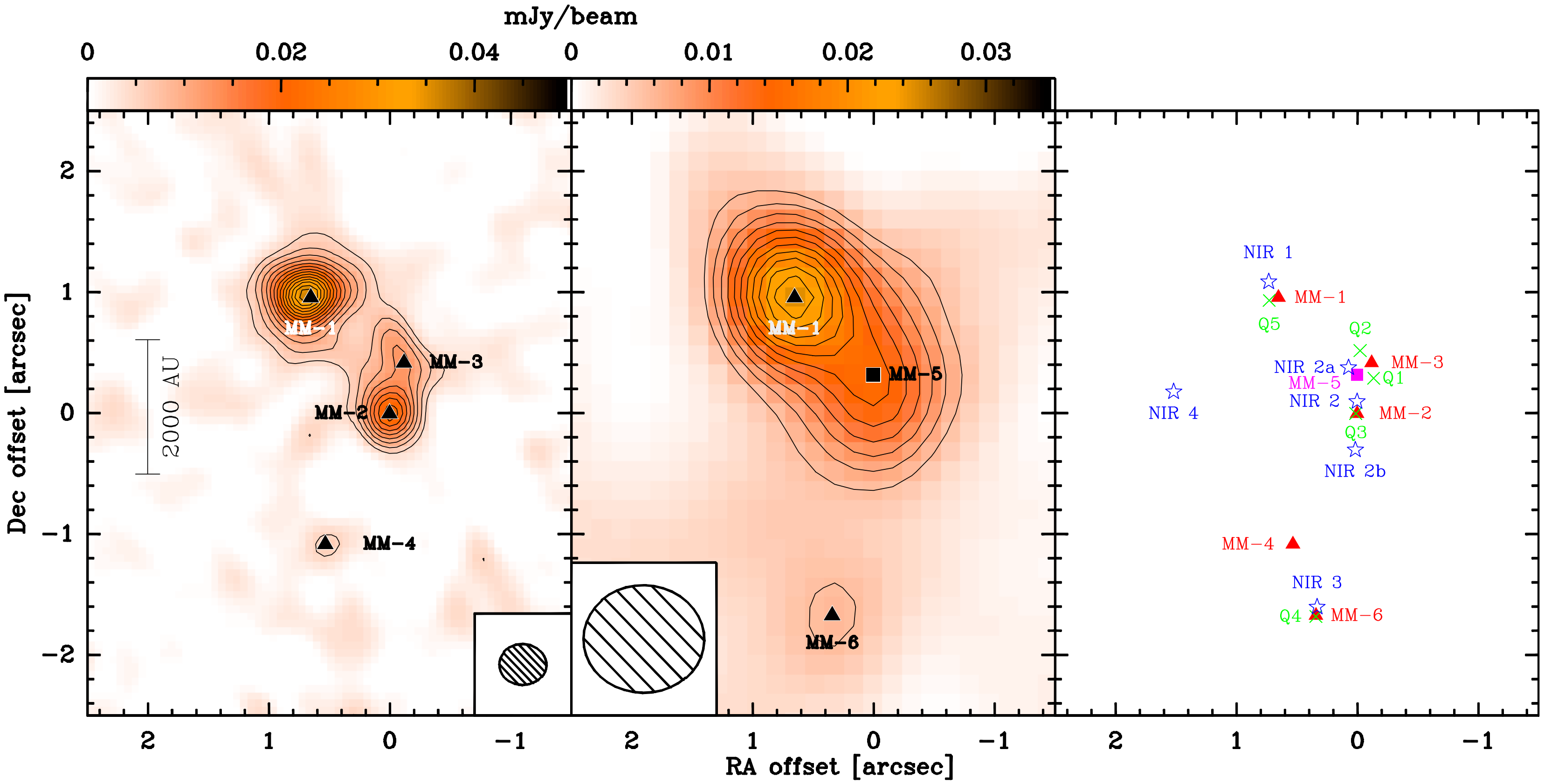

Figure 4.2: *Left and center panels*: Continuum maps of W3 IRS5 at 1.4 mm and 3.4 mm respectively. Contour levels for the 1.4 mm continuum start at 4σ increasing by 2σ steps, and at 3σ increasing by 1σ steps for the 3.4 mm continuum. Beams are shown at the bottom left of each panel. Filled triangles mark the millimetric sources detected (see Table 4.2). *Right panel*: Relative positions of the different sources in W3 IRS5. Filled triangles are the millimetric sources detected, stars are the NIR sources detected by Megeath et al. (2005) and crosses are the radio sources detected by van der Tak et al. (2005). The grey square marks source MM5, the joint contribution of sources MM2 and MM3. In Table 4.4 are the identified counterparts, discussed in the text.

4.2.3 Silicon Monoxide emission

Silicon Monoxide (SiO) is believed to trace strong shocks in dense molecular gas, particularly in molecular outflows (Schilke et al. 1997). Here two SiO transitions were observed, SiO (5 – 4) with the 1.4 mm receiver and SiO (2 – 1) with the 3.4 mm receiver, seen in Fig. 4.3. The five molecular outflows we detect are also marked, labeled SIO-a – e, four of them at both wavelengths and the larger, westernmost outflow, only at 3.4 mm. In Fig. 4.4 we present the spectra of the five outflows, taken toward the center of the outflow for SIO-a, -b and -d, and toward the wings for SIO-c and -e. From the integrated spectra of the 1.4 mm emission within a $4'' \times 4''$ region centered at the phase center (Fig. 4.4f), we determine that the contribution of the ambient gas emission ranges from -43 to -36 km s^{-1}. This is also in agreement with the linewidth expected from the ambient gas emission for dense and small cores (Garay & Lizano 1999).

The spatial coincidence of the blue- and redshifted emission of SIO-a with MM1 indicates that it is aligned very close to the line of sight (l.o.s.). This can be clearly seen in the SiO (5 – 4) transition at 1.4 mm, where the most compact emission is mapped (Fig. 4.3). At this wavelength the red- and blueshifted contours are overlapped, however in the SiO (2 – 1) transition at 3.4 mm only a blueshifted emission peak is seen. There is overlapping redshifted emission, but it does not peak at the same position but rather $\sim 0.5''$ to the southeast of the blueshifted peak. The position of the SiO (5 – 4) peaks as well as the blueshifted SiO (2 – 1) peak match the position of MM1, and this is likely the driving source of this outflow. The spectrum at the center position (Fig. 4.4a) exhibits a broad emission with a FWHM linewidth of 7 km s^{-1}, showing also a strong peak at the systemic velocity and a redshifted narrow (FWHM of 1.3 km s^{-1}) feature peaking at ~ -32 km s^{-1}.

For SIO-b on the other hand, we detect and resolve a blue- and redshifted peak only at 3.4 mm while at 1.4 mm we only resolve a blueshifted peak. The peaks at both wavelengths are resolved, and the source MM2 is the most likely driving source. Its central spectrum (Fig. 4.4b) shows clear blue- and a redshifted peaks. This outflow also seems to be aligned close to the l.o.s., according to the position of the blue- and redshifted emission peaks without any emission at the V_{LSR}.

The outflow SIO-c is detected in both SiO transitions, although at 3.4 mm the redshifted lobe is faint. The outflow is aligned in the east–west direction, its axis defined as the straight line joining the blue and red emission peaks at 3.4 mm. The source MM4 lies on the outflow axis and between the lobes, thus this may be the driving source. The SiO (5 – 4) spectrum from this outflow (Fig. 4.4c) shows broad blue- and redshifted peaks. The blue peak is broad (~ 5.5 km s^{-1}) and asymmetric towards bluer velocities, its maximum at -44 km s^{-1}, while the redshifted peak is symmetric and narrower, with a FWHM linewidth of 4.8 km s^{-1} peaking at -36 km s^{-1}.

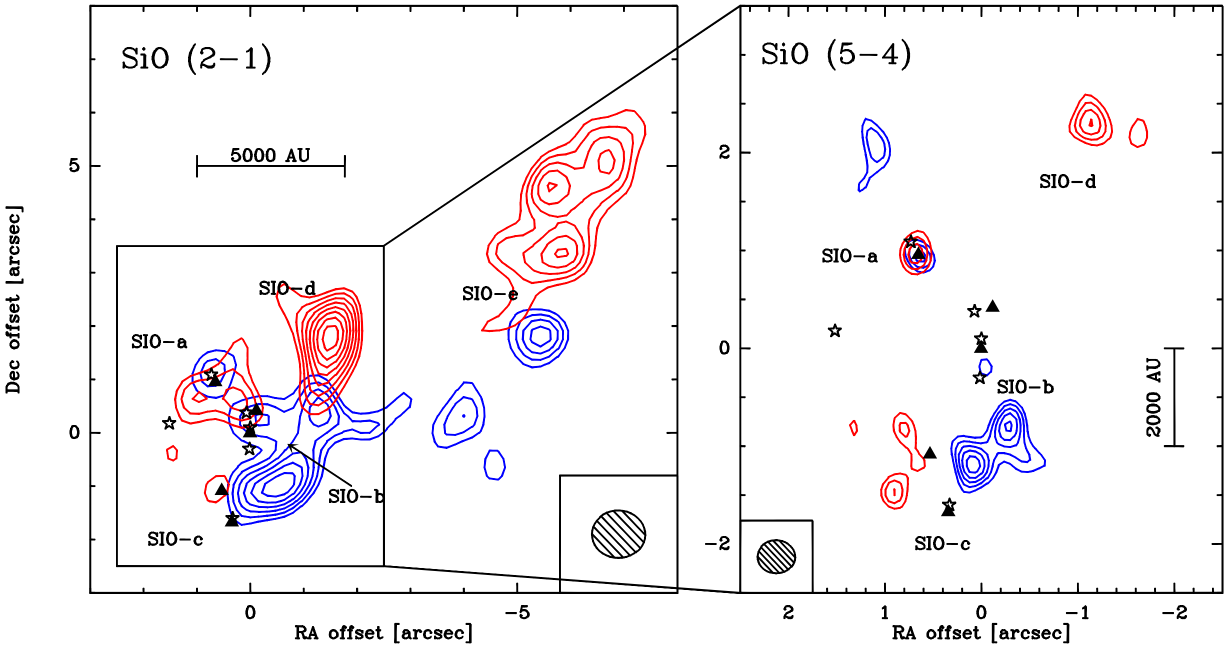

Figure 4.3: Silicon Monoxide emission detected towards W3 IRS5. The left panel shows the 3.4 mm SiO (2 – 1) transition and the right panel shows the 1.4 mm SiO (5 – 4) transition. Blue contours outline the blueshifted emission and red contours the redshifted emission. The blueshifted emission ranges from −58 to −43 km s^{-1} and the redshifted emission ranges from −36 to −28 km s^{-1}. In the left panel contouring starts at the 4σ level and in the right panel at the 3σ level, increasing in 1σ steps for both. The beams are represented at the bottom of each panel. Labeled SIO-a through -e are the five outflows detected, filled triangles are the millimetric sources shown in this paper and the stars mark the NIR sources from Megeath et al. (2005).

For SIO-d we do not detect any millimetric source that could be driving it. This outflow is best traced at 3.4 mm in the SiO (2 – 1) transition, where both blue- and redshifted lobes are clearly seen, while at 1.4 mm just the redshifted emission is traced. The central spectrum for this outflow (Fig. 4.4d) shows broad (~ 5.5 km s^{-1}) double-peaked emission centered at the systemic velocity. On larger scales Ridge & Moore (2001) found a CO outflow spanning 1.73 pc in the northwest–southeast direction, the same as SIO-d (see Sec. 4.3.2).

SIO-e is even more intriguing because it is the biggest of the five outflows and we cannot identify a driving source for it in the millimetric or the IR. Like SIO-d it lies in the northwest–southeast direction, matching the large-scale CO emission. Its SiO (2 – 1) spectrum shows broad blueshifted emission, peaking at −40.4 km s^{-1} with a FWHM of 5.6 km s^{-1}. The redshifted peak is narrower with a FWHM of 3.4 km s^{-1} and with its maximum at −38 km s^{-1}. Its driving source should be located relatively far from the two main sources MM1 and MM2, at ~10^4 AU from them.

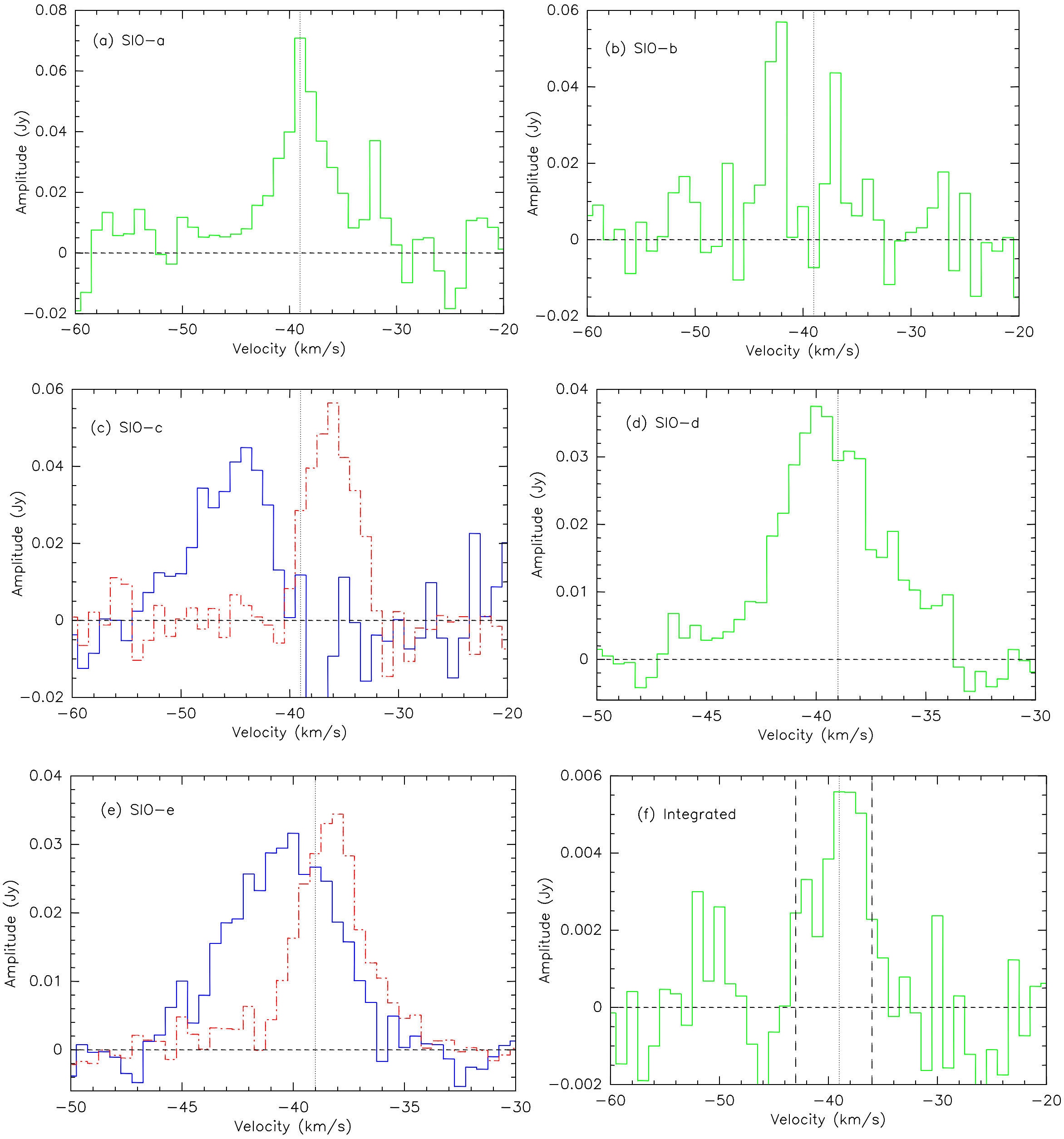

Figure 4.4: SiO spectra of the five detected outflows. In panels (a), (b) and (c) are the SiO (5 – 4) spectra of outflows SIO-a, -b and -c respectively. In panels (d) and (e) are the SiO (2 – 1) spectra of the outflows SIO-d and -e respectively and in panel (f) is the spectrum of the SiO (5 – 4) integrated emission in a 4″ × 4″ region centered at the phase center. The vertical dotted line in each panel marks the systemic velocity of −39 km s^{-1}. In panels (c) and (e) the blue line is the blueshifted emission and the red line is the redshifted emission. In panel (f) the long-dashed lines demark the velocity regime for the ambient gas. The spectra were taken toward the center of the outflow for SIO-a, -b and -d, and toward the wings for SIO-c and -e.

4.2.4 Sulfur Dioxide emission

Fig. 4.5 panels (a) and (c) show the integrated Sulfur Dioxide (SO_2) emission detected towards W3 IRS5 at 1.4 mm and 3.4 mm respectively, while in panels (b) and (d) are the velocity maps for each transition. The SO_2 emission envelops the whole region where MM1, MM2, MM3 and MM4 are detected, which can be clearly seen in Fig. 4.5c. We see a clear velocity gradient in the southeast–northwest direction, indicating that the envelope of W3 IRS5 rotates as a whole and is likely gravitationally bound. This is more noticeable in the SO_2 ($8_{3,5} - 9_{2,8}$) velocity map (Fig. 4.5d), where the velocity gradient goes smoothly from −42 to −37 km s^{-1}.

The peaks of integrated SO_2 emission at 1.4 mm (Fig. 4.5a) lie close to the sources MM1, MM2 and MM4. As SO_2 is also an indicator of shocked material (e.g. Helmich et al. 1994) this strengthens the argument for the detection of the outflows traced by SiO, and supports the statement in Sec. 4.2.3 that those sources drive the outflows SIO-a, SIO-b and SIO-c, respectively.

The SO_2 ($22_{2,20} - 22_{1,21}$) velocity map (Fig. 4.5b) shows a strong jump of $\sim$ 4 km s^{-1} in a thin spatial region southeast of the two main millimetric peaks. The velocity shift is from $\sim$ −35 km s^{-1} to $\sim$ −39 km s^{-1} –the systemic velocity– in a narrow strip of $\sim$ $1.1'' \times 0.2''$. The region north of the jump is where most of the gas is blueshifted while the region south of the jump is completely redshifted. This "velocity jump" (see Sec. 4.3.3) may be the signature of two molecular flows moving in opposite direction, ramming each other and compressing the gas in the region of the jump (Klessen et al. 2005; Heitsch et al. 2005, 2006; Peretto et al. 2006, 2007).

4.3 Discussion

4.3.1 Continuum Sources

With $L = 2 \times 10^5 L_\odot$, W3 IRS5 is a high-mass star-forming region, but the (proto)stellar content in its core is unknown because of high obscuration. Since it is a hypercompact HII region, it already has a large (proto)stellar component. While it is not possible to directly measure the masses of the (proto)stars with millimeter data, it is possible to derive the masses of the circumstellar structure. The low masses that we calculate from the 1.4 mm data can be attributed to a circumstellar structure, while the surrounding envelope likely contributes to the larger masses derived from the 3.4 mm data. However, we must take into account the "short-spacing problem" when calculating the masses of the continuum sources. This caveat, inherent to interferometers, means that a high percentage of the flux is filtered out and lost. This effect is more severe in the extended configurations (long baselines), as in our case.

Single-dish submillimetric measurements for W3 IRS5 at 850μm with SCUBA (Moore et al. 2007) indicate a peak intensity $I_\nu \sim 9.6$ Jy beam^{-1} with a beam of 14″. Considering a dependence

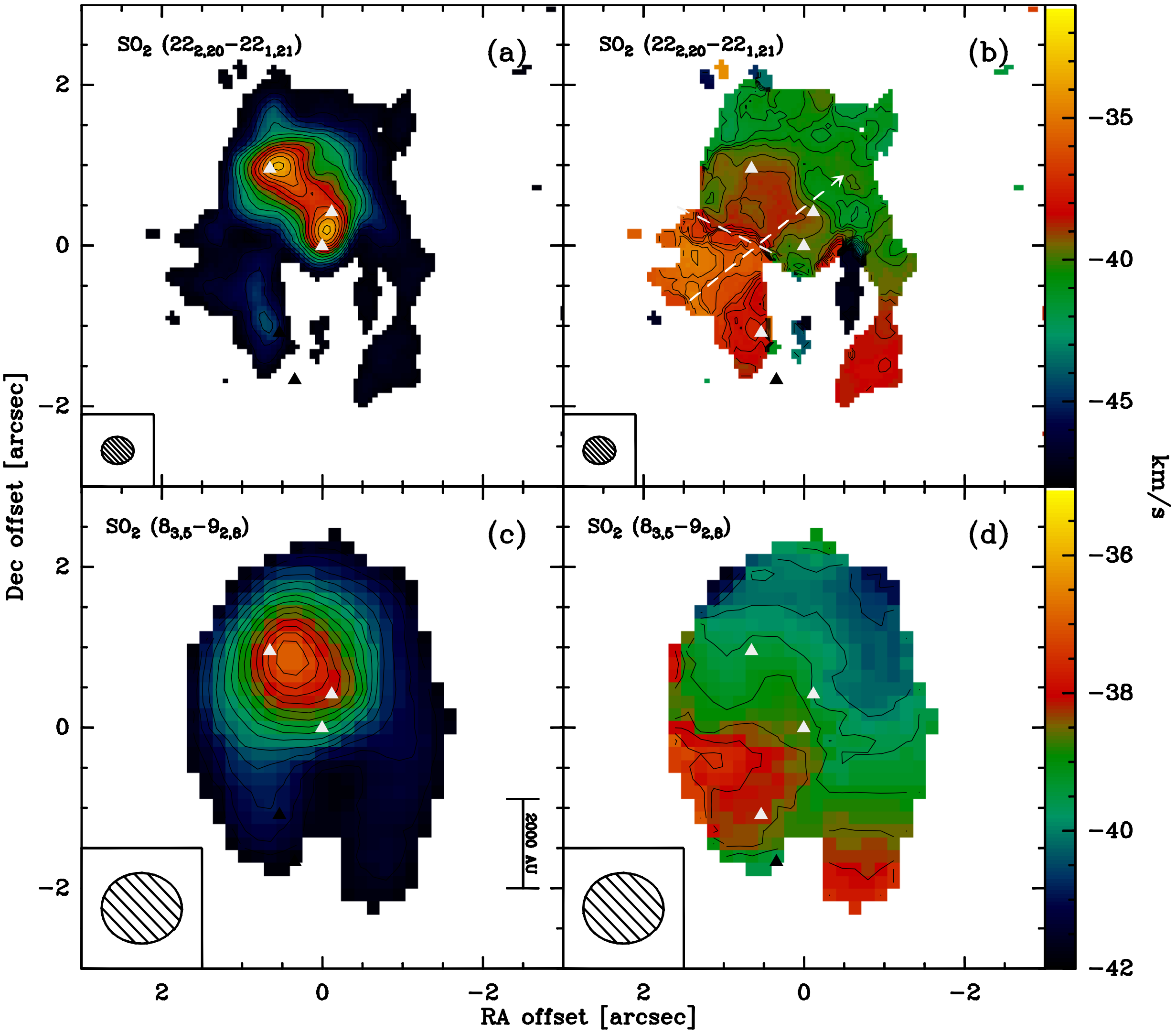

Figure 4.5: Sulfur Dioxide emission detected towards W3 IRS5. At 1.4 mm is the SO_2 ($22_{2,20} - 22_{1,21}$) transition (upper half) and at 3.4 mm is the SO_2 ($8_{3,5} - 9_{2,8}$) transition (lower half). Panels (a) and (c) show the integrated emission, with contour steps of 0.2 Jy beam^{-1} km s^{-1} for (a) and 0.1 Jy beam^{-1} km s^{-1} for (c). In panels (b) and (d) is the velocity distribution of the emission, from −48 to −33 km s^{-1} for (b) and from −42 to −37 km s^{-1} for (d), in both panels the contour step is 0.5 km s^{-1}. The respective beams are shown at the bottom-right corner of each panel. Filled black and white triangles are the mm sources from Table 4.2. The dashed white line in panel (b) marks the velocity jump discussed in the text.

$I_\nu \propto \nu^4$ for the peak intensity, that value corresponds then to $I_\nu \sim 1.4\,\mathrm{Jy\,beam^{-1}}$ at 1.4 mm and $I_\nu \sim 36\,\mathrm{mJy\,beam^{-1}}$ at 3.4 mm. In our 1.4 mm continuum map the flux density recovered within the SCUBA beam is $S_\nu \sim 0.12$ Jy taking the average contribution of the free-free emission into account (see Table 4.3), meaning that $\sim 91\%$ of the flux is lost. Therefore the calculated masses at 1.4 mm are actually a lower limit for the current mass of each source. On the other hand, at 3.4 mm we recover $S_\nu \sim 36$ mJy, so with our calibration accuracy, we do not miss too much of the flux within the SCUBA beam. However, within the PdBI main beam of $\sim 55''$ at 3.4 mm we only recover ~ 73 mJy, while Moore et al. (2007) reports an integrated flux $S_\nu \sim 200$ Jy, implying that although we are recovering most of the central emission, we are filtering out the more extended emission. Nevertheless, at 3.4 mm the obtained values for the masses are somewhat more representative of the mass of their envelopes.

The SO_2 velocity signature across the core is indicative of overall rotation of the gas associated with MM1 to MM3. Assuming equilibrium between the gravitational and rotational force at the outer radius of the cloud:

$$M_{rot} = \frac{(\delta v)^2\, r}{G} \tag{4.1}$$

$$\Rightarrow \frac{M_{rot}}{\mathrm{M}_\odot} = 1.13 \times 10^{-3} \left(\frac{\delta v}{\mathrm{km\,s^{-1}}}\right)^2 \left(\frac{r}{\mathrm{AU}}\right) \tag{4.2}$$

where r is the cloud radius ($\sim 2'' \equiv 4000$ AU) and δv is half the velocity regime observed in the first-moment map ($\sim 2.5\,\mathrm{km\,s^{-1}}$, see Fig. 4.5d).

The gravitationally supported mass implied by this observed rotation is $M_{\mathrm{rot}} \sim 30\,\mathrm{M}_\odot$, which is on the same order as the derived masses from the 3.4 mm continuum emission. Hence, these sources are likely gravitationally bound and may still be accreting from an envelope not seen in our data, further increasing their masses. Also, from the distribution of the gas it is likely that sources MM1, MM2 and MM3 are sharing a common envelope, of which we are tracing the inner parts at 3.4 mm. This envelope would have much more of the mass than in the immediate region surrounding each source, but it is being filtered out by the interferometer.

The different percentage of flux filtered out in each wavelength band can be explained the same way as the big (over a factor ~ 10) difference between the calculated masses at 1.4 mm and 3.4 mm. Both wavelengths were observed at the same time with the same interferometer configurations, meaning that although the ground baselines are the same, the uv coverage measured in units of wavelength (kλ) at 3.4 mm is more compact than at 1.4 mm, therefore tracing more extended components in the region.

Even if we are recovering most of the compact flux at 3.4 mm, we are likely mapping the surrounding envelopes close to the already formed (proto)stellar objects and therefore cannot state the actual masses of the (proto)stellar objects but only give a lower limit of the mass of the gas and dust associated largely with the individual sources. The same can be applied for the column density, however in this case –despite the caveats mentioned– the values we obtain are more realistic for a region like W3 IRS5. Our results of $N(H_2) \sim 10^{25}\,\mathrm{cm}^{-2}$ at 3.4 mm, are 2–3 magnitudes higher than for low-mass star-forming regions, for which the derived column densities at ~3 mm are of the order $N(H_2) \sim 10^{22-23}\,\mathrm{cm}^{-2}$ (e.g.: Harjunpaeae & Mattila 1996; Motte et al. 1998; Kontinen et al. 2000). Also our results are about two orders of magnitude higher than the critical column density of $1\,\mathrm{g\,cm}^{-2}$ required to form high-mass stars under Milky Way conditions calculated by Krumholz & McKee (2008), which corresponds to $N(H_2) = 3 \times 10^{23}\,\mathrm{cm}^{-2}$, suggesting that within the sources we are mapping, (proto)stars of over $10\,\mathrm{M}_\odot$ are forming.

Table 4.4: Millimetric, radio, NIR and MIR counterparts.

MM	Q[a]	NIR[b]	MIR[a]
1	5	1	1
2	3	2	2
3	1 + 2	2a	...
4	...	...	...
5	1 + 2 + 3	...	...
6	4	3	3

[a] From van der Tak et al. (2005).
[b] From Megeath et al. (2005).

Radio observations for this region are also available. Comparing the positions of the five radio sources detected with the VLA at 43 GHz (Q-band) by van der Tak et al. (2005) and the positions in Table 4.2, we can identify the following: MM1 → Q5, MM2 → Q3 and MM6 → Q4 (see Fig. 4.2). The source MM3 lies between Q1 and Q2 and is not a compact source but rather stretched out, so it appears to be the joint contribution from Q1 and Q2, which could not be individually resolved with our spatial resolution (see Table 4.4).

At shorter wavelengths, van der Tak et al. (2005) found three MIR sources in W3 IRS5 with the Keck I telescope, while Megeath et al. (2005) found seven NIR sources with the Hubble Space Telescope, three of them which match the aforementioned MIR sources.

Because absolute astrometry was not available for these NIR and MIR sources, to compare them with our MM sources we refer to their relative positions, shown in Table 4.5. The separation between MM1 and MM2 is $1.16'' \pm 0.10''$ at a position angle (P.A.) of 214 ± 5 degrees, being the only match for the pair MIR1 and MIR2 with a mean separation of $1.12'' \pm 0.07''$ and a

P.A. of 216.8 ± 1.7 degrees, and for the pair NIR 1 and NIR 2 with a separation of $1.23''$ and a P.A. of 217 degrees. Similarly, the pair MM1–MM6 with a separation of $2.65'' \pm 0.10''$ and P.A. = 187 ± 2 degrees is the only match for the pair MIR1–MIR3 with a mean separation of $2.70'' \pm 0.05''$ and a P.A. of 187.2 ± 0.7 degrees and for the pair NIR 1–NIR 3 with a separation of $2.7''$ and P.A. = 189 degrees. Therefore we can identify MIR1 and NIR 1 with MM1, MIR2 and NIR 2 with MM2, and MIR3 and NIR 3 with MM6. Comparing the separation of $0.94'' \pm 0.10''$ and P.A. = 235 between MM1 and MM3, with the separation of $0.98''$ and P.A. = 224 between NIR 1 and NIR 2a, we can also identify source NIR 2a with MM3. For the rest of the NIR sources we do not find a millimetric counterpart (see Table 4.4).

The only millimetric source without any NIR, MIR or radio counterpart is MM4, hence it is a new detection. Its mass could not be corrected by the free-free emission contribution and it is approximately half as massive as MM3.

Considering the region encompassed by MM1 and MM2, we estimate a lower limit for the (proto)stellar density. Assuming spherical symmetry, we detect the four sources MM1, MM2, Q1 and Q2 (joined in MM3) within a $1.16''$ or ~ 2100 AU diameter region, corresponding to a (proto)stellar density of $\sim 7 \times 10^6$ protostars pc^{-3}. Even counting just the three resolved sources MM1, MM2 and MM3 we obtain $\sim 5 \times 10^6$ protostars pc^{-3}. It is not the first time that (proto)stellar densities higher than the typical 10^4 stars pc^{-3} for young clusters (Lada & Lada 2003) are found. Beuther et al. (2007b) calculated a density of $\sim 1.4 \times 10^5$ protostars pc^{-3} in the system G29.96–0.02. Although high, this (proto)stellar density is still below the “critical” value of $\sim 10^8$ protostars pc^{-3} predicted by the merging scenario (Bonnell et al. 1998). However it is the first time that densities higher than the required $\sim 10^6$ protostars pc^{-3} to induce high-mass close binary mergers (Bonnell & Bate 2005) are obtained. While the observations of W3 IRS5 show no evidence of the presence of such binary systems, we have shown that such densities can be achieved in high-mass star-forming regions, and with further improvement in the spatial resolution, (proto)stellar densities as high —or even higher— may be a common phenomenon.

W3 IRS5 is surrounded by a dense embedded cluster of intermediate- to low-mass stars: Megeath et al. (1996) calculated a stellar surface density of $\sim 0.25 \times 10^4$ pc^{-2} for a cluster radius of $21''$, a quarter of the $\sim 10^4$ pc^{-2} density calculated by Megeath et al. (2005) from the NIR sources they found with a maximum projected separation of $\sim 5,600$ AU. Again within a ~ 2100 AU diameter region, we calculate a (proto)stellar surface density of $\sim 4 \times 10^4$ protostars pc^{-2} considering just the three millimetric sources previously mentioned, revealing a density gradient towards the center of the cluster. Assuming that this embedded cluster around W3 IRS5 forms an independent subcluster within the W3-Main region, the fact that there are already low-mass stars in the outskirts of W3 IRS5 while high-mass stars are still forming in its center supports the hypothesis that the low-mass stars form before their high-mass counterparts (e.g., Kumar et al. 2006).

Table 4.5: Relative astrometry of the known sources in W3 IRS5.

Sources[a]	sep (arcsec)	PA (deg)
MM1–MM2	1.16	214
MIR1–MIR2	1.12	216.8
NIR1–NIR2	1.23	217
MM1–MM6	2.65	187
MIR1–MIR3	2.70	187.2
NIR1–NIR3	2.7	189
MM1–MM3	0.94	235
NIR1–NIR2a	0.98	224

[a] MIR sources from van der Tak et al. (2005) and NIR sources form Megeath et al. (2005).

The projected separation between sources ranges from ~750 AU for MM2–MM3 to ~4700 AU for MM1–MM6. Compared to the median radius of 40,000 AU for the farthest outlying member of the 14 trapezia identified by Abt & Corbally (2000), W3 IRS5 has significantly smaller projected separations than those observed in optically visible trapezia. Therefore we have several compact sources sharing a common envelope from which gas may still be accreting in a region with a high (proto)stellar density beyond the point where close binary mergers can be induced, and with column densities higher than the theorized threshold to form high-mass stars. Thus, conditions are favorable for the formation of high-mass stars.

4.3.2 Outflows

For the five SiO outflows mapped in this region, we identify the driving sources of just three of them. Outflows SIO-a, SIO-b and SIO-c are driven by sources MM1, MM2 and MM4 respectively, while for outflows SIO-d and SIO-e we do not detect candidates for their driving sources. For SiO-e however, Tieftrunk et al. (1998) have detected a NH_3 (1,1) emission peak (labeled 1 in their Figs. 4 and 5) near the center of this outflow, which may be hosting the driving source of SiO-e.

The determination of the outflow parameters is subject to a big number of errors, including that it is often difficult to separate the outflowing gas from the ambient gas and that the inclination angles of the flows are also often unknown. In this case we also have the caveat that high amounts of flux are filtered out by the interferometer. To get an estimation of the effect of this we compare our results with the measurements of Gibb et al. (2007). They report an integrated intensity of 2.4 K km s^{-1} for SiO (5 – 4), while we recover only 0.4 K km s^{-1} within our primary beam. Although apparently the integrated intensity given by Gibb et al. (2007) covers a slightly larger region, the main emission stems from an area covered by approximately twice our 22″ primary beam at 217 GHz, implying a great fraction of missing flux also in SiO (5 – 4). On the other hand, for SiO (2 – 1) they measure 2.5 K km s^{-1} but with most of the emission within a region covered by our 55″ primary beam at 87 GHz, in which we measure 1.7 K km s^{-1}. Again, we are losing a high amount of flux, although less than in SiO (5 – 4).

We derived the physical parameters for the small-scale outflows detected here. To obtain the H_2 column densities we first have to calculate the SiO column densities for each outflow, for which we follow the LTE approach described by Irvine et al. (1987). Since we do not have estimates of the excitation temperature, we assume a usual value for the outflows of 30 K for our calculations (Beuther et al. 2002c), resulting in the formula:

$$\frac{\mathrm{N}_{\mathrm{SiO}\,(2-1)}}{\mathrm{cm}^{-2}} = 1.3 \times 10^{12} \int T \mathrm{d}v \qquad (4.3)$$

where $\int T\mathrm{d}v$ is the SiO (2 – 1) integrated intensity in K km s^{-1}. We used the SiO (2 – 1) data because it has recovered the most flux. The obtained results are shown in Table 4.6. Adopting a SiO abundance ratio to obtain the H_2 column density is not straightforward. The SiO abundance has a big uncertainty, with reported values ranging from SiO/H_2 $\sim 10^{-7}$ (Mikami et al. 1992; Zhang et al. 1995) for shocked, energetic regions to SiO/H_2 $\sim 10^{-12}$ (Ziurys & Friberg 1987; Ziurys et al. 1989) in quiescent, cold dark clouds. To take into account such uncertainty, our calculations were done assuming SiO/H_2 $= 10^{-7}$ and SiO/H_2 $= 10^{-9}$, a range suitable for a high-luminosity region such as W3 IRS5. Although the values we obtain are too low for a region like W3 IRS5 with a total luminosity of $\sim 10^5 L_\odot$ and are more typical in regions with lower luminosity (see e.g. Ridge & Moore 2001; Gibb et al. 2007; Palau et al. 2007; Beltrán et al. 2008), we have to keep in mind that aside from the caveats mentioned above, we are tracing smaller scales opposed to large-scale outflow.

In general, our parameters are several orders of magnitude lower than for the CO outflow detected by Ridge & Moore (2001) even assuming extremely low SiO abundances. From the CO measurements, the outflow has a mechanical energy $E_{CO} \sim 10^{49}$ erg, while for a SiO abundance of 10^{-9}, adding the contribution of all the outflows we obtain that $E_{SiO}/E_{CO} \sim 4 \times 10^{-4}$. From the values in Table 4.6 it is evident that the rest of the parameters follow the same trend. Only at unrealistically low SiO abundances are our results comparable with the CO outflow.

Table 4.6: Properties of the small-scale outflow features

Outflow	M_{out} ($M_\odot$)	E (erg)	$\dot{M}_{\rm out}$ ($M_\odot$ yr^{-1})	F_m ($M_\odot$ yr^{-1} km s^{-1})	L_m ($L_\odot$)
$SiO/H_2 = 10^{-7}$					
SIO-a + SIO-b[1]	0.04	4(43)	4(-5)	2(-4)	0.25
SIO-c	0.03	5(43)	5(-5)	7(-4)	0.80
SIO-d	0.03	1(43)	3(-5)	2(-4)	0.09
SIO-e	0.08	3(43)	1(-5)	6(-5)	0.03
$SiO/H_2 = 10^{-9}$					
SIO-a + SIO-b[a]	4	4(45)	4(-3)	2(-2)	25
SIO-c	3	5(45)	5(-3)	7(-2)	80
SIO-d	3	1(45)	3(-3)	2(-2)	9
SIO-e	8	3(45)	1(-3)	6(-3)	3

[a] Treated jointly because they cannot be differentiated in the redshifted SiO (2 − 1) emission. Also, because they are aligned close to the l.o.s., the parameters for which the outflow size is needed were calculated assuming an average size based on the other three outflows.

Notes – The numbers in brackets represent powers of 10.

The SiO outflow that Gibb et al. (2007) detect is aligned in the east–west direction, and the CO outflow also has an east–west component peaking at ∼35″ east of the main source extending to the west, as well as a NW–SE component. In Fig. 4.3 we can see that the SiO (2 − 1) emission follows a similar distribution, with east–west (outflow SIO-c) and NW–SE (outflows SIO-d and -e) components. As mentioned before we do not detect driving sources for SIO-d and -e. Because of their orientation these two outflows could be delineating the high-density regions of the large-scale CO outflow and although we cannot exclude this option, we believe that they are two separate features. Furthermore, Tieftrunk et al. (1998) detects an ammonia signature close to the projected center of SIO-e which may be hosting its driving source. With our data we cannot confidently point to any of our detected dust sources as the driving source of the large-scale CO outflow and it is possible that this CO outflow is the result of the mix of all the small-scale outflows and therefore might have driving sources opposed to a single driving source.

As shown in Sec. 4.2.3 the outflows SIO-a and SIO-b are aligned very close to the l.o.s.. This situation explains the fact that despite the high column densities toward MM1 and MM2 (see Table 4.2), which correspond to visual extinctions of several thousand magnitudes, NIR and MIR counterparts are detected. The cavities carved out by the outflows have reduced the extinction along the l.o.s., allowing us to see hot dust in the interior of the protostellar envelopes in the NIR and MIR, either directly or through scattered light.

In the case of SiO-b, the outflow also would explain the occurrence and location of NIR 2b, below NIR 2/MM2. That near-infrared source can be interpreted as scattered light from the outflow cavities. Similarly in the case of source NIR 2a, it is close to the proper motion radio source IRS 5a detected by Wilson et al. (2003) with the VLA. They propose that IRS 5a/NIR 2a was formed by or in an outflow originating south of its position, which agrees with the localization of our outflow SiO-b.

From the H_2O masers they detect, Imai et al. (2000) suggest two outflows in the north–south direction in this region. However from our data we cannot identify counterparts for the position of the H_2O masers in this region, nor outflows in a north–south direction.

4.3.3 Velocity jump

Fig. 4.6 shows a postion-velocity diagram across the velocity jump seen in SO_2 ($22_{2,20} - 22_{1,21}$). Two distinct velocity components are seen, one peaking at $\sim -35\,\mathrm{km\,s^{-1}}$ and the other peaking at $\sim -39\,\mathrm{km\,s^{-1}}$, spatially located at both sides of the velocity jump, denoted by the black dashed line. The velocity jump has also been confirmed at higher frequencies, in SO_2 (8–7) and HCN (4–3) observations taken with the SMA towards W3 IRS5 (T. Bourke, priv. comm.), and could be explained by the theory of gravoturbulent star formation (Heitsch et al. 2005, 2006; Klessen et al. 2005; Mac Low & Klessen 2004and references therein), which states that protostellar cores might form by turbulent ram pressure compression in the regions behind the fronts of converging turbulent flows.

From Figs. 4.2 and 4.5b we can see that the main sources of W3 IRS5 are located next to the region where the velocity jump occurs, distributed roughly parallel to the jump. This is what would be expected if their collapse were triggered by the compression of converging flows. Furthermore, numerical models (Klessen et al. 2005) predict that one of the observational signatures of such compression by ram pressure is localized maxima of the l.o.s. velocity dispersion in the low column density gas in the outskirts of the core. According to the continuum maps (Fig. 4.2), the region where this velocity jump occurs is in the outskirts of the cores, where the dust emission and the gas column density are low. This suggests that we may be looking at two molecular flows converging and triggering the star formation in W3 IRS5.

At larger spatial scales, a similar signature was found by Peretto et al. (2006, 2007) in their study of NGC 2264–C at millimetric wavelengths, where they found in N_2H^+ and $H^{13}CO^+$ emission a velocity jump of ~ $2\,\mathrm{km\,s^{-1}}$ over a very narrow spatial region. They modeled this jump as the signature of the large-scale, axial collapse of NGC 2264–C along its long axis and towards its center, with an inclination angle of ~ 45°. It would also trace a possible dynamical interaction between protostellar sources at its center, where they detected a millimeter continuum peak. The case of W3 IRS5 could be similar but observed with higher spatial resolution. Making an analogy between Peretto et al. (2007) and W3 IRS5, sources MM1, MM2 and MM3 would correspond to their sources CMM3 and CMM13, and we would just be mapping the region of the jump from redshifted emission to the systemic velocity, which corresponds in their case to the transition from CMM4 to CMM13–CMM3.

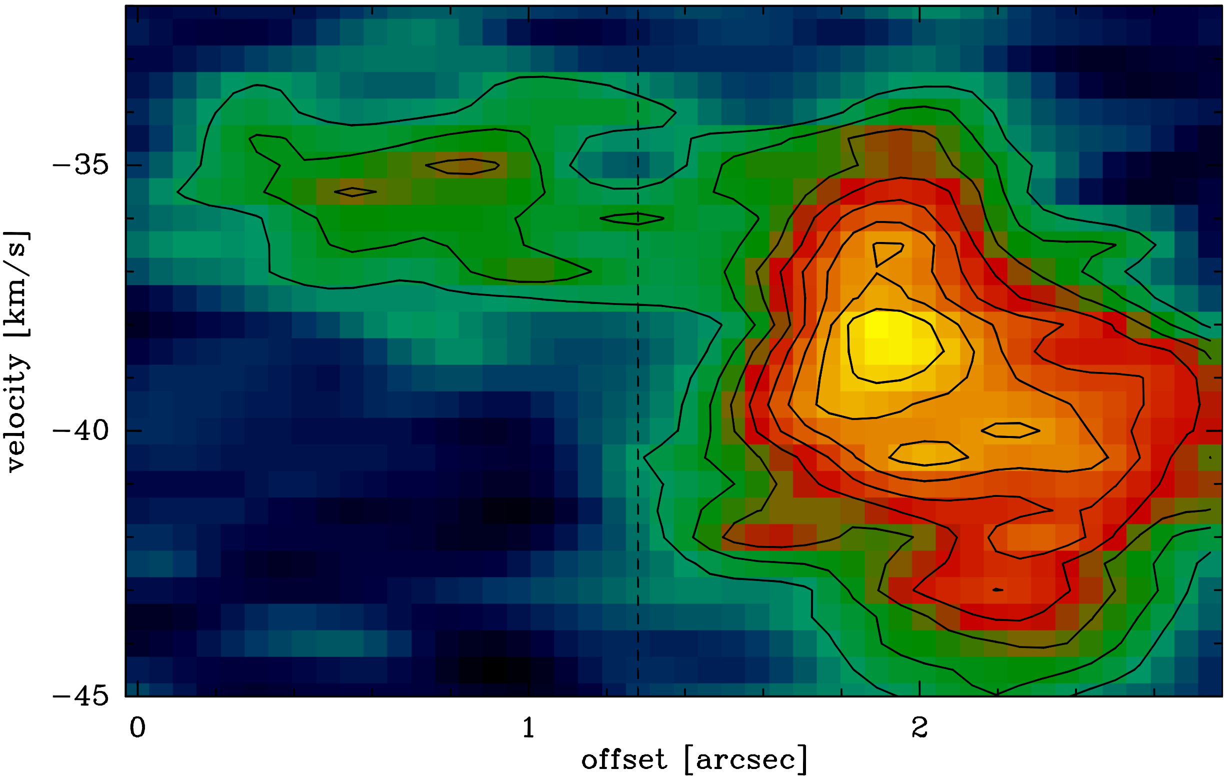

Figure 4.6: SO_2 ($22_{2,20} - 22_{1,21}$) position velocity diagram along the line shown in Fig. 4.5(b) with a white arrow. The velocity jump described in the text can be seen here, where an emission feature is peaking at ~ $-35\,\mathrm{km\,s^{-1}}$ while another feature is peaking at ~ $-39\,\mathrm{km\,s^{-1}}$, spatially at either side of the jump, denoted by the black dashed line. Contours start at 20% of the maximum flux and continue in 10% steps.

4.4 Summary and Conclusions

In the continuum maps of W3 IRS5 obtained with the PdBI at 1.4 mm and 3.4 mm we detect 5 individual sources. Their calculated absolute masses are strongly affected by the spatial filtering inherent to the interferometric technique, however from the relative separations of the three strongest sources we propose the scenario of a Trapezium-like system, with at least 3 objects enclosed within a ~2000 AU radius, with a high (proto)stellar density of $\sim 5 \times 10^6$ protostars pc^{-3}, and sharing a common envelope from which they may still be accreting gas.

Four of the five millimetric sources are identified as counterparts of sources previously detected in NIR, MIR and radio wavelengths by Megeath et al. (2005) and van der Tak et al. (2005). The remaining fifth source (labeled MM4) is a new detection.

Thanks to the spatial resolution of ~0.36″ we can for the first time trace the small-scale flow, detecting five molecular outflows, identifying the driving source of three of them. Although we find on short spatial scales the same alignment and axes as the outflows on large spatial scales previously detected in SiO and CO, within our accuracy and the big uncertainties introduced, we do not find strong evidence to support that we are tracing the inner and denser regions of those outflows, but we cannot rule out that possibility. However these small-scale outflows appear to be different features.

Two of the SiO outflows are close to the l.o.s. direction and each one is being driven by each of the stronger millimetric sources detected. This configuration would explain why these two objects are detected from NIR to radio wavelengths because cavities being carved out by outflows nearly along the l.o.s. have lower extinction, allowing the detection in the NIR and MIR of the hot dust near the collapsing protostar, while the long wavelength emission traces the dusty envelope that still surrounds it.

The SO_2 emission and velocity structure indicate that W3 IRS5 still has a gravitationally bound envelope. Also in SO_2 we detect a velocity jump of several km s^{-1} in a very narrow region adjacent to the continuum sources. This could be the signature of two converging molecular flows, compressing the gas and triggering the star formation, as predicted by the theory of gravoturbulent star formation.

Chapter 5

Fragmentation: Summary and Conclusions

The work presented in the last chapters leave no doubt that in the formation of massive stars the fragmentation plays an important role, and describe it is a challenging task.

In an effort to shed light into this matter, we observed with mm interferometers six MSF regions. Those regions were chosen primarily by being among the closest known at an average distance of 2kpc, and for being relatively bright with luminosities on the order of $\sim 10^4\,\mathrm{L}_\odot$. We targeted some of the closest MSF regions to take full advantage of the angular resolution that mm interferometers can provide. Having in mind that current mm interferometers can achieve an angular resolution of $1''$ (at ~ 1 mm), we observed with a projected spatial scale of ~ 2000 AU. At the typical densities of $\sim 10^{6-7}\,\mathrm{cm}^{-3}$ and temperatures of $\sim 20-40$ K of molecular cores, that spatial scale is below their Jeans length.

Throughout the previous chapters we analyzed the stellar content and the mass distribution of these regions, in this chapter I will summarize the results and conclusions we have reached.

5.1 The mass distribution

Our primary approach was to derive the CMF of the regions. We found this task particularly hindered by the fact the observed MSF regions had a relatively low number of cores. We found less than a few dozens of cores in all cases, which constituted a problem at the moment of defining the binning of the CMF. To overcome that problem we applied two methods. Firstly we adopted a logarithmic binning (i.e., the bins have equal width in a logarithmic axis), to increase the axis' "resolution" at lower masses and secondly, we produced CMFs with many different bin sizes and took their average slope as the final result, in this way to taking into account the arbitrariness of choosing a specific bin width.

The first method was deemed necessary after we noticed that the majority of the cores had masses towards the lower side of our mass spectrum. In particular, this is noticeable in the case of IRAS 19410+2336. In that region, 18 of the 26 detected cores ($\sim 70\%$) have masses below the 25% of the mass of the most massive core. This comes as no surprise if the region has a CMF slope comparable to the Salpeter slope for the IMF, as we later found. A quick algebra shows us that for a distribution of the form $m^{-\beta}$, if $\beta \sim 2.4$ then about $\sim 70\%$ of the elements of the distribution have abscissas below the 25% of any given abscissa.

We also derived the cumulative CMF for the MSF regions. This form of the CMF is more indicated to use when we are dealing with low number of elements, since it does not require a binning and each core we detect is then a point in the curve to be fit. This increases the statistical significance of the fit when comparing it with the fit of the differential CMF. The latter, because of the binning, has a lower number of points to make a fit.

As just mentioned above, for the MSF region IRAS 19410+2336 we obtained a CMF slope comparable to Salpeter. Both the differential and the cumulative CMF statistically agree in a value $\beta = -2.3 \pm 0.2$. This confirms previous results of Beuther & Schilke (2004) on this region, who also obtained a Salpeter slope. The observations in both cases were similar. They were taken with the same instrument, achieving similar resolution but in our case, a sensitivity 3 times better. This allowed us to confirm some dubious 3σ detections in the first work, and refute others. Nevertheless, at the moment of derive the CMF the number of cores was similar in both works.

There was, however, one important difference between the study of Beuther & Schilke (2004) and the one presented in this thesis. The masses of the cores in the former were calculated adopting an average value for the temperature. In contrast, we calculated the temperature of the cores using formaldehyde molecular lines. This improved the uncertainty of the masses derived from the continuum emission, assumed to originate from thermal emission from the dust.

Nevertheless, even with more precise values for the masses the result for the CMF did not change significantly. This suggests then that knowing the temperature structure, although important to derive the physical properties of the sources, does not affect the slope of the CMF too strongly. There is, however, the fact that the average temperature of the sources is comparable to the IRAS temperature used by Beuther & Schilke (2004). This is to be expected, because with its angular resolution IRAS could not resolve this region and therefore a temperature derived from its observations would be an average value over the whole region. This agrees with other result we obtained, that the large majority of the cores were "cold", with relatively low temperatures of about $\sim$ 35 K. Thus they dominate the average temperature of the region because they are more numerous, and the effect of the few "hot" cores with temperatures $\sim$ 100 K is insignificant on average.

Taking into account that according to our assumptions the mm continuum comes from optically thin thermal emission from the dust and then for a given flux density the mass is inversely proportional to the temperature, then higher temperatures for the more massive clumps would decrease these derived masses. Then, if the temperature of the lower-mass cores remains (practically) unchanged, these effects would result in a somewhat steeper slope. This was in fact what happened with the temperatures: The less massive clumps had temperatures comparable to the average, while the higher-mass cores had temperatures higher than the average. Nevertheless the slope did not become steeper, but remained practically unchanged. That the aforementioned effect on the slope did not occur, may have been because most of the cores did not sensitively change their temperature. That is likely the explanation of why knowing the temperature structure of the region did not affect the result for the slope of the CMF.

All considered, the slope of the CMF for IRAS 19410+2336 is comparable to the high-mass end of the Salpeter stellar IMF. I have discussed in Chapter 2 about the implications this might carry. In summary, this similarity would imply that the IMF in a MSF region is set at the moment of fragmentation during its early evolutionary stages, and that the most likely scenario for the formation of massive stars is a scaled-up version of fragmentation and disk-accretion. Nevertheless this result is not completely conclusive. It requires for instance a nearly one-to-one relationship between cores and final stars. Such relationship is supported by theoretical models and some observations (see Sec. 2.4.3), but on the other hand we have shown in Chapter 4 on W3 IRS5 how a core can indeed fragment below the spatial scales we used to derive the CMFs presented in this work. In that case the main mm core, of projected size $\sim$ 4000 AU, is seen to fragment into three protostars. In Chapters 2 and 3 our spatial scale is $\sim$ 2500 AU, and we identify as single cores many sources that could probably be unresolved systems like W3 IRS5. Another example is source i58-2 (see Sec. 3.5.1), that we identify as a single core but in the MIR is seen to further resolve into three embedded sources. And here is where come into play the numerical simulations of Swift & Williams (2008), that suggest that the high-mass slope of the IMF may change due to further fragmentation of the cores. To be able to take this into account, we will need observations in the mm with consistently better angular resolution, such as the ones the Atacama Large Millimiter Array (ALMA) will be able to provide in the next years.

In contrast, are the results of Chapter 3. In a similar approach as for IRAS 19410+2336 we derive the CMF of a joint sample of cores from the MSF regions IRAS 06056+2131 and IRAS 06058+2138 obtaining a slope $\beta = -1.5 \pm 0.1$, much shallower than before and comparable to the clump mass function derived at spatial scales an order of magnitude larger (e.g., Kramer et al. 1998). As mentioned above, the method we used in this case is the same as for IRAS 19410+2336, with the sole difference that we were not able to determine at the moment a temperature structure. However, based on the results of Chapter 2 this most likely does not represent a problem, and determining the temperature of the cores would likely not change the CMF's slope significantly.

The observations in this case were taken with a different observatory (SMA instead of PdBI), but since the angular resolution and sensitivity obtained were similar, we can safely rule out any instrumental bias. We conclude in Chapter 3 that the reasons causing the difference in the slope are very likely of physical nature. Among the plausible explanations we propose, is the very interesting possibility that this flatter slope might be an indicator of the relative youth of the regions. The details are given in Sec. 3.5.2 but in short, we propose that a younger MSF region would present a shallower CMF slope than an older region. Furthermore, the slope would be evolving with the cloud, and could serve as an indicator of the cloud age of the cloud.

This comes from theoretical results and simulations showing that the slope of the CMF for gravitationally dominated clouds is flatter than that of clouds dominated by turbulence. Since at early evolutionary stages the cloud is mainly gravitationally supported and as it evolves the feedback from the forming stars introduces turbulence in the medium, it could be possible that the CMF slope evolves with the cloud, becoming steeper as the cloud ages.

There are some signatures that could give us hints about the relative age of the MSF regions, the more reliable is perhaps the deuterium fractionation in the cloud. To determine that fractionation, one needs to know the relative abundance between the hydrogenated and deuterated isotopologues of a given species. For instance, we have detected DCN in both IRAS 06056+2131 and IRAS 06058+2138. Having HCN data would allow us to determine their relative abundance ratio and then the deuterium fractionation in the region. The determination of the relative age of IRAS 19410+2336 and IRAS 06056+2131/IRAS 06058+2138 would test if our suggestion about the probable link between the CMF slope and the evolutionary stage of the region is viable. We will continue our work in this regions, observing pairs of several hydrogenated and deuterated isopotologues like HCN/DCN, H_2CO/HDCO or D_2CO, and N_2H^+/N_2D^+.

Another possibility that might explain the difference in slope is a difference in average density among the clouds, caused in turn by a density gradient found in the Galactic disk towards the outer Galaxy (Kalberla & Dedes 2008). This variation is detected in our data: IRAS 19410+2336 (in the inner Galaxy) is in average more dense than IRAS 06056+2131 and IRAS 06058+2138 (both in the outer Galaxy). Such variation in density would mean a different characteristic Jeans scale in each region, favoring the formation of more massive cores in IRAS 06056+2131 and IRAS 06058+2138 than in IRAS 19410+2336 and thus determining the shallower CMF of the former regions.

As mentioned earlier, there is also the fact that some of the cores we observe can be resolved into more sources. The results of Chapter 4 on W3 IRS5 are a prime example of this. In that case we obtained an excellent angular resolution of $\sim 0.36''$ with the PdBI, and thus were able to resolve this region down to a spatial scale of 750 AU, a resolution about 3 times better than for the other MSF regions studied in this thesis. In a similar situation as with the observed MSF regions IRAS 06061+2151 and IRAS 06063+2040, we could not derive a CMF for W3 IRS5 due to the low number of cores detected at 1.4 mm, four in each case[1]. We could, however, investigate the protostellar content in those regions, which I summarize in the following section.

5.2 On the protostellar content

Of all the regions presented in this work, W3 IRS5 is a particular case. As mentioned before, we could resolve this region down to spatial scales a few times better than the other regions. What we found in W3 IRS5 is what we classified as a prototrapezium system, i.e. a non-hierarchical multiple (proto)star system similar to the Trapezium in Orion.

We resolved the mm emission of W3 IRS5 into five sources, most likely single protostars. The main three sources detected at 1.4 mm have separations no larger than ~ 1000 AU, which translate in a (proto)stellar density of $\sim 5 \times 10^6$ protostars pc^{-3}. This density is high when compared with the typical densities of $\sim 10^4$ stars pc^{-3} that are found in young clusters, and it was the first time that such high density was found, showing that it is possible to find density values located between the $\sim 10^6$ protostars pc^{-3} required to induce close-binary mergers and the $\sim 10^8$ protostars pc^{-3} threshold after which mergers can occur. Furthermore, the sources are gravitationally bound according to the detected SO_2 emission, and sharing a common gas envelope.

The SO_2 emission also presents a sharp velocity jump of $\sim 4\,\mathrm{km\,s^{-1}}$ occurring in a thin spatial region of about 2000 × 400 AU, that was confirmed by observations of other two molecular

---

[1] In W3 IRS5 we detect 5 cores in total, but one of them (MM-6; see Fig. 4.2) is only seen at 3.4 mm.

transitions (see Secs. 4.2.4 and 4.3.3). Similar signatures are found in other regions at larger spatial scales (Peretto et al. 2006, 2007), and are suggested to indicate the merging of molecular flows. This is something predicted by the theory of gravoturbulent star formation, which states that protostellar cores might form due to the ram pressure of converging molecular flows.

This fact on itself is very interesting and suggest a possible scenario where the star formation on W3 IRS5 might have been triggered by compression, but also remarks the significance that the medium has on massive star formation. Particularly in the case of W3 IRS5, the region is located in the very active star formation region W3-Main, and is surrounded by several HII regions including diffuse ones (see, e.g., Fig. 4.1). Strong feedback from these HII regions can be expected mainly in the form of stellar winds including ionizing high-energy particles, and is not a wild idea to consider that W3 IRS5 may be a triggered star-formation site.

A constant in our research is that some of the mm cores we detect are associated with sources at different wavelengths. These associations are useful to estimate the relative evolutionary stage of the different cores within a region. We see for example in IRAS 06056+2131-S that the source i56s-2 has a radio counterpart but not a NIR one, while i56s-6 has a clear NIR counterpart but no radio emission is detected towards it. This suggests that i56s-6 is older than i56s-2, since the former has a protostar that has already begun to clear a cavity in its envelope while the latter is harboring an ignited protostar that has not yet started to clear a cavity and is only revealed by the radio emission from the gravitationally trapped hyper- or ultra-compact HII region that it has started to ionize.

This pattern is found in all the MSF regions observed[2] and highlights the importance of tackle massive star formation with a multiwavelength approach. In this thesis I have shown some of the early results of the FEMS project, that among its targets for the VLT-SINFONI spectrograph are some of the MSF regions we have observed (see Chapter 3), and remarked how useful it is to have NIR and mm information for the analysis of the data. Once the analysis of the NIR data is completed, we would probably be able to obtain more information from both mm and NIR datasets that might be overlooked or deemed unimportant when analyzed alone. An example could be, for instance, that some weak and diffuse H_2 emission is detected and at the moment is deemed as a possible artifact of the image, but then turns out that a mm core is detected at the same position and then that overlooked NIR feature is now hinting that the mm core might already being forming a star that is starting an outflow, shocking the medium and producing the H_2 emission.

When looking at the continuum emission, we also see that there is not a clear pattern in how the cores are distributed in the regions. For instance, IRAS 06058+2138 presents a more spherical

---

[2] Note that IRAS 06063+2040 does not present any known counterpart, however we have stated in Sec. 3.5.1 that this region is likely not a MSF site.

distribution, while IRAS 06056+2131 is filamentary and IRAS 19410+2336 is somewhat elongated but not filamentary. This is most likely a direct result of the morphology of the parental cloud in each case so it should be expected to be found. However, it is worth noticing that the regions do not present in all cases a typical core-halo distribution with the higher-mass cores towards the center of the protocluster and surrounded by the lower-mass cores. Two contrasting examples of this are IRAS 19410+2336 and IRAS 06058+2138 (see Figs. 2.1 and 3.3). Both present a non-filamentary structure, but in the former the two more massive cores (12-s and 13-s) are located next to each other in the very edge of the mm emission and the lower-mass cores are located more to the north, while in the latter the two cores with higher mass (i58-5 and i58-7) are located towards the center of the protocluster and the less massive sources are distributed around them. Also when the emission is filamentary there is no defined tendency. Both IRAS 06056+2131-N and IRAS 06056+2131-S are filamentary, but in the former the most massive source (i56n-4) is at the edge of the emission while in the latter it (i56s-7) is located at the middle.

5.2.1 Outflows and molecular signatures

The typical mode of clustered formation of massive stars, together with the fact that high-mass protostars start core-fusion while still embedded in their parental cloud, introduce many feedback "sources". Compact HII regions are an example of a feedback source, but one other source that is omnipresent in star-forming regions are molecular outflows, and they can also "start" before an on-site HII region forms and begins to interact with the inter-core medium.

In all of the regions of our study we targeted at least one shock tracer species, in particular the SiO molecule[3]. Using transitions of this molecule we could identify small-scale outflows in some of the regions. An exception was IRAS 19410+2336, for which the small-scale outflow structure had been already described by Beuther et al. (2003).

Of particular interest is W3 IRS5, where we resolve the already known large-scale CO and SiO outflow into five smaller-scale outflows. Two of them were found to be close to the line-of-sight direction, and we could also identify the driving sources of 3 of the 5 outflows (see Secs. 4.2.3 and 4.3.2).

The two outflows nearly along the line-of-sight direction would explain why their proposed driving sources (MM-1 and MM-2, see Figs. 4.2 and 4.3) are detected from NIR to radio wavelengths. The cavities being carved out by those outflows have lower extinction, allowing the detection in the NIR and MIR of the hot dust near the collapsing protostar, while the long wave-

---

[3] In the case of IRAS 19410+2336 we already had the SiO data from Beuther et al. (2003), thus no shock tracer was included in the observations carried out for this thesis.

length emission traces the dusty envelope that still surrounds it. This once more highlights the importance of having into account the feedback when studying MSF regions, as well as counting with multiwavelength data.

Of no less importance is the study of the chemistry in MSF regions. Most of the information we can obtain about them is coming from the molecular lines observed, as for example shock tracers as the already mentioned SiO or sulfur dioxide, both of which we used in this thesis to study the outflows detected and, in the case of W3 IRS5, also to derive the kinetic properties of the gas. In Chapter 2 we have shown a clear example of the usefulness of a molecular tracer like formaldehyde, which since some time is being used as a tool to determine gas temperatures and densities. Methyl cyanide is another example of gas-thermometer, as well as ammonia, that like formaldehyde can be used both as a thermomether and a density tracer.

One particular conclusion we can draw from our work with temperature tracers is that when working with high-resolution interferometric observations, special care must be taken at the moment of assuming that a transition is optically thin. In Sec. 2.3.1 we see how the formaldehyde transitions we used as thermometers are in the limit of the optically thin/thick regime turnover point. This happened because we were tracing high-density gas (on the order of $\sim 10^{6-7}\,\mathrm{cm}^{-3}$), and at such densities the assumption of optically thin emission cannot be taken as a given and should be checked whenever is possible. In the past this was not an issue, because when such temperature-tracing techniques were established most of the available mm data was from single-dish antennas. Those antennas trace low-density gas ($\sim 10^{3-4}\,\mathrm{cm}^{-3}$), where the optically thin assumption holds. With the coming of the next generation mm interferometers like ALMA, we will start to observe gas at even higher densities than now. At that point the usual temperature tracers will no longer be useful since their observed molecular lines will be optically thick. Therefore, new tracers with higher critical densities will be needed.

Another important chemical tool are isotopologues. Although they have been used since long time (for example ^{13}CO and C^{18}O, just to name a few), lately more attention is being given to deuterated species. Deuterated hydrogen cyanide (DCN), deuterated and doubly-deuterated formaldehyde (HDCO and D_2CO, respectively), and deuterated diazenylium (N_2D^+) are some of the deuterated isotopologues currently used to determine the deuterium fractionation in MSF regions, a property that is thought to be linked with the age of the cloud. We have detected DCN in two of the regions observed (see Chapter 3), and we note that further observations of HCN and other deuterated-hydrogenated pairs are needed to determine the relative age of some of the observed regions.

5.3 Continuing work

It is clear that the issue of the slope of the CMF on MSF regions is not yet resolved. So far we have only a few determinations of it at spatial scales of ~ 0.01 pc, and they are giving different results. We need to expand the sample observing not only more MSF regions, but also regions at different evolutionary stages and with different luminosities, to diversify the sample and construct a complete picture of the fragmentation of MSF regions.

We also need to observe MSF regions at high spatial resolution. Right now this is a tricky endeavor since with the currently available mm interferometers we are more or less restricted to the closest regions if we want to achieve spatial scales on the order of ~ 0.01 pc. Nevertheless, projects on that direction are being formulated, as for example a small survey of the W3-Main and the AFGL333 star-forming complexes that at this moment is being proposed for observations and would start in 2010.

Of invaluable help will be the upcoming ALMA. Its enhanced spatial resolution on the order of $0.01''$ and below will allow us to map dense cores in dust continuum and see whether further fragmentation is occurring or not. Its high sensitivity (due to its large-bandwidth receivers) and dynamical range (thanks to its increased *uv*-coverage) will allow us to detect the fainter, lower-mass objects in MSF regions, and therefore we would be able to derive a more complete CMF, less affected by incompleteness. Thanks also to simultaneous observations with the ALMA Compact Array, large field imaging (with mosaicing) will be possible, facilitating the observation of large samples.

The MSF regions we have already observed also need more work. In particular are the already mentioned interferometric observations of deuterated-hydrogenated pairs, as well as single-dish observations of formaldehyde to complement the interferometric data and be able to complete the temperature determination.

We also need to obtain similar observations of the CMF in star-forming sites with peculiar environments, to compare with the results of more “standard” regions. I will expand my work particularly in that direction, observing with mm interferometry sites of triggered star formation as the borders of the Hii regions RCW 82 and RCW 120. This will be done within the framework of the “Herschel imaging survey for OB Young Stellar objects” (HOBYS) guaranteed-time key-project of the Herschel space telescope. The interferometric mm data will complement the Herschel far-infrared data, once more providing a multiwavelength approach to the study of massive star-formation.

Throughout the pages of this thesis I have shown that the formation of massive stars is still a process with many unknowns, questions to solve (and to be asked), and presenting us with ambiguous and challenging scenarios where several different explanations are possible. We are now finishing to scratch the surface of the problem and is in the next years, with the upcoming observatories as Herschel and ALMA, that many of the open questions that are still baffling us will hopefully start to answered. We are indeed living in a golden age for the study of massive star-formation.

Acknowledgments

First, I acknowledge my supervisor Henrik Beuther for all the time spent on me. During the last three years he has taught me not only a large part of what I have presented in this thesis, but also how to be a proper scientist and all that this implies. And I am sure that I will keep learning from him. So I thank him for his patience and willingness, and most of all for giving me the opportunity to come to Heidelberg to obtain my PhD in the first place. This has given to me many professional opportunities and has allowed me to meet a lot of people from many different places, and for that I will always be grateful.

I want to thank other people involved in astronomy for their help and interest in my work, by reading my proposals, papers and/or simply sharing their knowledge and time. These people are Cassie Fallscheer, Qizhou Zhang, Nimesh Patel, Tyler Bourke and Peter Schilke. My officemates Bhargav Baidya and Mario Gennaro, for all the fruitful discussions we had.

The referees and members of my thesis committee (Henrik Beuther, Thomas Henning, Ralf Klessen and Mathias Bartelmann) are acknowledged for being in my oral defense and for reading this thesis. I also want to thank Cassie Fallscheer and Boyke Rochau, for giving me their corrections and translations.

There are many others whom I would like to thank. Whether directly or indirectly, knowingly or not, they had supported me to carry this thesis to a good end. These people are José Borelli (hey, my Linux still needs repair!), Victoria Rodriguez and Camila Borelli (for keeping a piece of Argentina abroad!); Isabel Franco, Aday Robaina and Alejo Martinez (because beers don't drink by themselves); Federico Stasyszyn, Miriam Campos, Ariel Sánchez and Ximena Mazzalay (I will keep visiting Munich for as long as you are there!); Davide Fedele, Veronica Roccatagliata and Alessandro Berton (for showing me how much Italians and Argentinians are alike); Sergio Ruiz, Daniel Espada, Paula Teixeira and Gemma Busquet (because Cambridge would not have been the same without all of you). And all the others that I am forgetting right now, and that for sure will reproach me for it (if they ever find out, that is). To all of them, I say thanks.

Bibliography

Abt, H. A., & Corbally, C. J. 2000, ApJ, 541, 841

Alves, J., Lombardi, M., & Lada, C. J. 2007, A&A, 462, L17

Anandarao, B. G., Chakraborty, A., Ojha, D. K., & Testi, L. 2004, A&A, 421, 1045

Andre, P., Ward-Thompson, D., & Barsony, M. 2000, Protostars and Planets IV, 59

Bacmann, A., Lefloch, B., Parise, B., Ceccarelli, C., & Steinacker, J. 2007, in Molecules in Space and Laboratory

Baldry, I. K., & Glazebrook, K. 2003, ApJ, 593, 258

Ballesteros-Paredes, J., Klessen, R. S., Mac Low, M.-M., & Vazquez-Semadeni, E. 2007, in Protostars and Planets V, ed. B. Reipurth, D. Jewitt, & K. Keil, 63–80

Bally, J., Sutherland, R. S., Devine, D., & Johnstone, D. 1998, AJ, 116, 293

Belloche, A., André, P., & Motte, F. 2001, in Astronomical Society of the Pacific Conference Series, Vol. 243, From Darkness to Light: Origin and Evolution of Young Stellar Clusters, ed. T. Montmerle & P. André, 313–+

Beltrán, M. T., Brand, J., Cesaroni, R., Fontani, F., Pezzuto, S., Testi, L., & Molinari, S. 2006, A&A, 447, 221

Beltrán, M. T., Estalella, R., Girart, J. M., Ho, P. T. P., & Anglada, G. 2008, A&A, 481, 93

Beuther, H., Churchwell, E. B., McKee, C. F., & Tan, J. C. 2007a, in Protostars and Planets V, ed. B. Reipurth, D. Jewitt, & K. Keil, 165–180

Beuther, H., Kerp, J., Preibisch, T., Stanke, T., & Schilke, P. 2002a, A&A, 395, 169

Beuther, H., & Schilke, P. 2004, Science, 303, 1167

Beuther, H., Schilke, P., Menten, K. M., Motte, F., Sridharan, T. K., & Wyrowski, F. 2002b, ApJ, 566, 945

—. 2005, ApJ, 633, 535

Beuther, H., Schilke, P., Sridharan, T. K., Menten, K. M., Walmsley, C. M., & Wyrowski, F. 2002c, A&A, 383, 892

Beuther, H., Schilke, P., & Stanke, T. 2003, A&A, 408, 601

Beuther, H., Walsh, A., Schilke, P., Sridharan, T. K., Menten, K. M., & Wyrowski, F. 2002d, A&A, 390, 289

Beuther, H., Zhang, Q., Bergin, E. A., Sridharan, T. K., Hunter, T. R., & Leurini, S. 2007b, A&A, 468, 1045

Beuther, H., Zhang, Q., Sridharan, T. K., Lee, C.-F., & Zapata, L. A. 2006, A&A, 454, 221

Blitz, L. 1993, in Protostars and Planets III, 125–161

Blitz, L., Fukui, Y., Kawamura, A., Leroy, A., Mizuno, N., & Rosolowsky, E. 2007, in Protostars and Planets V, ed. B. Reipurth, D. Jewitt, & K. Keil, 81–96

Bonnell, I. 1997, in Astronomical Society of the Pacific Conference Series, Vol. 130, The Third Pacific Rim Conference on Recent Development on Binary Star Research, ed. K.-C. Leung, 1–+

Bonnell, I. A., & Bate, M. R. 2005, MNRAS, 362, 915

—. 2006, MNRAS, 370, 488

Bonnell, I. A., Bate, M. R., & Zinnecker, H. 1998, MNRAS, 298, 93

Bonnell, I. A., Larson, R. B., & Zinnecker, H. 2007, in Protostars and Planets V, ed. B. Reipurth, D. Jewitt, & K. Keil, 149–164

Bonnell, I. A., Vine, S. G., & Bate, M. R. 2004, MNRAS, 349, 735

Brand, J., & Wouterloot, J. G. A. 1995, A&A, 303, 851

Campbell, M. F., Butner, H. M., Harvey, P. M., Evans, N. J., Campbell, M. B., & Sabbey, C. N. 1995, ApJ, 454, 831

Carey, S. J., Clark, F. O., Egan, M. P., Price, S. D., Shipman, R. F., & Kuchar, T. A. 1998, ApJ, 508, 721

Carpenter, J. M., Snell, R. L., & Schloerb, F. P. 1995a, ApJ, 445, 246

—. 1995b, ApJ, 450, 201

Carr, J. S. 1987, ApJ, 323, 170

Caselli, P., Benson, P. J., Myers, P. C., & Tafalla, M. 2002a, ApJ, 572, 238

Caselli, P., & Dore, L. 2005, A&A, 433, 1145

Caselli, P., Stantcheva, T., Shalabiea, O., Shematovich, V. I., & Herbst, E. 2002b, Planet. Space Sci., 50, 1257

Caselli, P., Walmsley, C. M., Zucconi, A., Tafalla, M., Dore, L., & Myers, P. C. 2002c, ApJ, 565, 344

Casoli, F., Combes, F., & Gerin, M. 1984, A&A, 133, 99

Caswell, J. L., Vaile, R. A., Ellingsen, S. P., Whiteoak, J. B., & Norris, R. P. 1995, MNRAS, 272, 96

Ceccarelli, C., Loinard, L., Castets, A., Tielens, A. G. G. M., Caux, E., Lefloch, B., & Vastel, C. 2001, A&A, 372, 998

Cesaroni, R., Galli, D., Lodato, G., Walmsley, C. M., & Zhang, Q. 2007, in Protostars and Planets V, ed. B. Reipurth, D. Jewitt, & K. Keil, 197–212

Chabrier, G. 2003, PASP, 115, 763

Charnley, S. B. 1997, ApJ, 481, 396

Charnley, S. B., Tielens, A. G. G. M., & Millar, T. J. 1992, ApJ, 399, L71

Clark, P. C., Bonnell, I. A., & Klessen, R. S. 2008, MNRAS, 386, 3

Crapsi, A., Caselli, P., Walmsley, C. M., Myers, P. C., Tafalla, M., Lee, C. W., & Bourke, T. L. 2005, ApJ, 619, 379

Cyganowski, C. J., Brogan, C. L., & Hunter, T. R. 2007, AJ, 134, 346

Davies, M. B., Bate, M. R., Bonnell, I. A., Bailey, V. C., & Tout, C. A. 2006, MNRAS, 370, 2038

Davis, C. J., Moriarty-Schieven, G., Eislöffel, J., Hoare, M. G., & Ray, T. P. 1998, AJ, 115, 1118

Devine, K. E., Churchwell, E. B., Indebetouw, R., Watson, C., & Crawford, S. M. 2008, AJ, 135, 2095

Dobashi, K., Bernard, J.-P., & Fukui, Y. 1996, ApJ, 466, 282

Draine, B. T., Dale, D. A., Bendo, G., Gordon, K. D., Smith, J. D. T., Armus, L., Engelbracht, C. W., Helou, G., Kennicutt, Jr., R. C., Li, A., Roussel, H., Walter, F., Calzetti, D., Moustakas, J., Murphy, E. J., Rieke, G. H., Bot, C., Hollenbach, D. J., Sheth, K., & Teplitz, H. I. 2007, ApJ, 663, 866

Draper, N. R. 1998, Applied regression analysis, ed. N. R. Draper

Edris, K. A., Fuller, G. A., & Cohen, R. J. 2007, A&A, 465, 865

Elmegreen, B. G. 1997, ApJ, 486, 944

—. 2006, ArXiv Astrophysics e-prints

Enoch, M. L., Glenn, J., Evans, II, N. J., Sargent, A. I., Young, K. E., & Huard, T. L. 2007, ApJ, 666, 982

Fallscheer, C., Beuther, H., Zhang, Q., Keto, E., & Sridharan, T. K. 2009, ArXiv e-prints

Feigelson, E. D., & Townsley, L. K. 2008, ApJ, 673, 354

Fontani, F. 2008, in Astronomical Society of the Pacific Conference Series, Vol. 387, Massive Star Formation: Observations Confront Theory, ed. H. Beuther, H. Linz, & T. Henning, 30–+

Fontani, F., Zhang, Q., Caselli, P., & Bourke, T. L. 2009, A&A, 499, 233

Frerking, M. A., Langer, W. D., & Wilson, R. W. 1982, ApJ, 262, 590

Garay, G., & Lizano, S. 1999, PASP, 111, 1049

Garmany, C. D., Conti, P. S., & Massey, P. 1980, ApJ, 242, 1063

Garrod, R. T., & Herbst, E. 2006, A&A accepted, astro-ph/0607560

Ghosh, S. K., Iyengar, K. V. K., Karnik, A. D., Rengarajan, T. N., Tandon, S. N., & Verma, R. P. 2000, Bulletin of the Astronomical Society of India, 28, 515

Gibb, A. G., Davis, C. J., & Moore, T. J. T. 2007, MNRAS, 382, 1213

Goodwin, S. P., & Kouwenhoven, M. B. N. 2009, MNRAS, 397, L36

Goodwin, S. P., Kroupa, P., Goodman, A., & Burkert, A. 2007, in Protostars and Planets V, ed. B. Reipurth, D. Jewitt, & K. Keil, 133–147

Hanson, M. M., Luhman, K. L., & Rieke, G. H. 2002, ApJS, 138, 35

Harjunpaeae, P., & Mattila, K. 1996, A&A, 305, 920

Hartmann, L. 1998, Accretion Processes in Star Formation, ed. L. Hartmann

Hayashi, C. 1961, PASJ, 13, 450

Heitsch, F., Burkert, A., Hartmann, L. W., Slyz, A. D., & Devriendt, J. E. G. 2005, ApJ, 633, L113

Heitsch, F., Slyz, A. D., Devriendt, J. E. G., Hartmann, L. W., & Burkert, A. 2006, ApJ, 648, 1052

Helmich, F. P., Jansen, D. J., de Graauw, T., Groesbeck, T. D., & van Dishoeck, E. F. 1994, A&A, 283, 626

Henning, T., Cesaroni, R., Walmsley, M., & Pfau, W. 1992, A&AS, 93, 525

Henriksen, R. N. 1991, ApJ, 377, 500

Herbig, G. H., & Griffin, R. F. 2006, AJ, 132, 1763

Hildebrand, R. H. 1983, QJRAS, 24, 267

Hodapp, K.-W. 1994, ApJS, 94, 615

Howell, R. R., McCarthy, D. W., & Low, F. J. 1981, ApJ, 251, L21

Hunter, T. R., Brogan, C. L., Megeath, S. T., Menten, K. M., Beuther, H., & Thorwirth, S. 2006, ApJ, 649, 888

Imai, H., Kameya, O., Sasao, T., Miyoshi, M., Deguchi, S., Horiuchi, S., & Asaki, Y. 2000, ApJ, 538, 751

Irvine, W. M., Goldsmith, P. F., & Hjalmarson, A. 1987, in Astrophysics and Space Science Library, Vol. 134, Interstellar Processes, ed. D. J. Hollenbach & H. A. Thronson, Jr., 561–609

Jansen, D. J., van Dishoeck, E. F., & Black, J. H. 1994, A&A, 282, 605

Jansen, D. J., van Dishoeck, E. F., Black, J. H., Spaans, M., & Sosin, C. 1995, A&A, 302, 223

Jappsen, A.-K., Glover, S. C. O., Klessen, R. S., Mac Low, M.-M., & Kitsionas, S. 2006, The Universe at z ¿ 6, 26th meeting of the IAU, Joint Discussion 7, 17-18 August 2006, Prague, Czech Republic, JD07, #24, 7

Jijina, J., & Adams, F. C. 1996, ApJ, 462, 874

Johnstone, D., Fich, M., Mitchell, G. F., & Moriarty-Schieven, G. 2001, ApJ, 559, 307

Johnstone, D., Matthews, H., & Mitchell, G. F. 2006, ApJ, 639, 259

Johnstone, D., Wilson, C. D., Moriarty-Schieven, G., Joncas, G., Smith, G., Gregersen, E., & Fich, M. 2000, ApJ, 545, 327

Kahn, F. D. 1974, A&A, 37, 149

Kalberla, P. M. W., & Dedes, L. 2008, A&A, 487, 951

Kerton, C. R., Martin, P. G., Johnstone, D., & Ballantyne, D. R. 2001, ApJ, 552, 601

Keto, E. 2002a, ApJ, 568, 754

—. 2002b, ApJ, 580, 980

—. 2003, ApJ, 599, 1196

Kim, K.-T., & Kurtz, S. E. 2006, ApJ, 643, 978

Klein, R., Posselt, B., Schreyer, K., Forbrich, J., & Henning, T. 2005, ApJS, 161, 361

Klessen, R. S. 2001, ApJ, 556, 837

Klessen, R. S., Ballesteros-Paredes, J., Vázquez-Semadeni, E., & Durán-Rojas, C. 2005, ApJ, 620, 786

Kontinen, S., Harju, J., Heikkilä, A., & Haikala, L. K. 2000, A&A, 361, 704

Köppen, J., Weidner, C., & Kroupa, P. 2007, MNRAS, 375, 673

Kramer, C., Stutzki, J., Rohrig, R., & Corneliussen, U. 1998, A&A, 329, 249

Kramer, C., Stutzki, J., & Winnewisser, G. 1996, A&A, 307, 915

Kraus, S., Weigelt, G., Balega, Y. Y., Docobo, J. A., Hofmann, K.-H., Preibisch, T., Schertl, D., Tamazian, V. S., Driebe, T., Ohnaka, K., Petrov, R., Schöller, M., & Smith, M. 2009, A&A, 497, 195

Kroupa, P. 2002, Science, 295, 82

—. 2007, ArXiv Astrophysics e-prints

Kroupa, P. 2008, in Lecture Notes in Physics, Berlin Springer Verlag, Vol. 760, Lecture Notes in Physics, Berlin Springer Verlag, ed. S. J. Aarseth, C. A. Tout, & R. A. Mardling, 181–+

Kroupa, P., Tout, C. A., & Gilmore, G. 1993, MNRAS, 262, 545

Kroupa, P., & Weidner, C. 2005, in Astrophysics and Space Science Library, Vol. 327, The Initial Mass Function 50 Years Later, ed. E. Corbelli, F. Palla, & H. Zinnecker, 175–+

Krumholz, M. 2007, in Massive Stars: From Pop III and GRBs to the Milky Way, ed. W. Livio & E. Villaver

Krumholz, M. R., & McKee, C. F. 2008, Nature, 451, 1082

Kumar, M. S. N., Keto, E., & Clerkin, E. 2006, A&A, 449, 1033

Kurtz, S., Churchwell, E., & Wood, D. O. S. 1994, ApJS, 91, 659

Lada, C. J. 1999, in NATO ASIC Proc. 540: The Origin of Stars and Planetary Systems, ed. C. J. Lada & N. D. Kylafis, 143–+

Lada, C. J., & Lada, E. A. 2003, ARA&A, 41, 57

Lada, C. J., Muench, A. A., Rathborne, J., Alves, J. F., & Lombardi, M. 2008, ApJ, 672, 410

Lada, E. A., Bally, J., & Stark, A. A. 1991, ApJ, 368, 432

Langer, W. D., Wilson, R. W., & Anderson, C. H. 1993, ApJ, 408, L45

Larson, R. B. 1969, MNRAS, 145, 271

Leistra, A., Cotera, A. S., & Liebert, J. 2006, AJ, 131, 2571

Linsky, J. L. 2003, Space Science Reviews, 106, 49

Longmore, S. N., Burton, M. G., Minier, V., & Walsh, A. J. 2006, MNRAS, 369, 1196

Loren, R. B. 1989, ApJ, 338, 902

Loren, R. B., & Mundy, L. G. 1984, ApJ, 286, 232

Mac Low, M., & Klessen, R. S. 2004, Reviews of Modern Physics, 76, 125

Maíz Apellániz, J., & Úbeda, L. 2005, ApJ, 629, 873

Mangum, J. G., & Wootten, A. 1993, ApJS, 89, 123

Martín-Hernández, N. L., Bik, A., Puga, E., Nürnberger, D. E. A., & Bronfman, L. 2008, A&A, 489, 229

Matzner, C. D., & McKee, C. F. 2000, ApJ, 545, 364

McKee, C. F., & Tan, J. C. 2003, ApJ, 585, 850

Megeath, S. T., Herter, T., Beichman, C., Gautier, N., Hester, J. J., Rayner, J., & Shupe, D. 1996, A&A, 307, 775

Megeath, S. T., Townsley, L. K., Oey, M. S., & Tieftrunk, A. R. 2008, in Handbook of Star Forming Regions, Astronomical Society of the Pacific Conference Series, in press

Megeath, S. T., Wilson, T. L., & Corbin, M. R. 2005, ApJ, 622, L141

Menten, K. M., & Reid, M. J. 1995, ApJ, 445, L157

Mermilliod, J.-C., & García, B. 2001, in IAU Symposium, 191

Mikami, H., Umemoto, T., Yamamoto, S., & Saito, S. 1992, ApJ, 392, L87

Miller, G. E., & Scalo, J. M. 1979, ApJS, 41, 513

Minier, V., Burton, M. G., Hill, T., Pestalozzi, M. R., Purcell, C. R., Garay, G., Walsh, A. J., & Longmore, S. 2005, A&A, 429, 945

Moffat, A. F. J., Jackson, P. D., & Fitzgerald, M. P. 1979, A&AS, 38, 197

Mookerjea, B., Kramer, C., Nielbock, M., & Nyman, L.-Å. 2004, A&A, 426, 119

Moore, T. J. T., Bretherton, D. E., Fujiyoshi, T., Ridge, N. A., Allsopp, J., Hoare, M. G., Lumsden, S. L., & Richer, J. S. 2007, MNRAS, 379, 663

Motte, F., Andre, P., & Neri, R. 1998, A&A, 336, 150

Motte, F., André, P., Ward-Thompson, D., & Bontemps, S. 2001, A&A, 372, L41

Motte, F., Schilke, P., & Lis, D. C. 2003, ApJ, 582, 277

Muñoz, D. J., Mardones, D., Garay, G., Rebolledo, D., Brooks, K., & Bontemps, S. 2007, ApJ, 668, 906

Mühle, S., Seaquist, E. R., & Henkel, C. 2007, ApJ, 671, 1579

Mundy, L. G., Evans, II, N. J., Snell, R. L., & Goldsmith, P. F. 1987, ApJ, 318, 392

Neugebauer, G., Becklin, E. E., & Matthews, K. 1982, AJ, 87, 395

Norberg, P., & Maeder, A. 2000, A&A, 359, 1025

Nutter, D., & Ward-Thompson, D. 2007, MNRAS, 374, 1413

Oey, M. S., Watson, A. M., Kern, K., & Walth, G. L. 2005, AJ, 129, 393

Ossenkopf, V., & Henning, T. 1994, A&A, 291, 943

Padoan, P., & Nordlund, Å. 2002, ApJ, 576, 870

Palau, A., Estalella, R., Ho, P. T. P., Beuther, H., & Beltrán, M. T. 2007, A&A, 474, 911

Palla, F., & Stahler, S. W. 1993, ApJ, 418, 414

—. 2000, ApJ, 540, 255

Panagia, N. 1973, AJ, 78, 929

Parise, B., Leurini, S., Schilke, P., Roueff, E., & Thorwirth, S. 2007, in Molecules in Space and Laboratory

Peretto, N., André, P., & Belloche, A. 2006, A&A, 445, 979

Peretto, N., Hennebelle, P., & André, P. 2007, A&A, 464, 983

Pety, J. 2005, in SF2A-2005: Semaine de l'Astrophysique Francaise, ed. F. Casoli, T. Contini, J. M. Hameury, & L. Pagani, 721–+

Pflamm-Altenburg, J., & Kroupa, P. 2006, MNRAS, 373, 295

Portinari, L., Moretti, A., Chiosi, C., & Sommer-Larsen, J. 2004, ApJ, 604, 579

Preibisch, T., Balega, Y., Hofmann, K.-H., Weigelt, G., & Zinnecker, H. 1999, New Astronomy, 4, 531

Puga, E., Bik, A., Waters, L. B. F. M., Henning, T., Kaper, L., van den Ancker, M., Lenorzer, A., Churchwell, E., Kurtz, S., Rodón, J. A., Vasyunina, T., Kouwenhoven, M. B. N., Beuther, H., Linz, H., Horrobin, M., Stolte, A., de Koter, A., Thi, W. F., Martín-Hernández, N. L., Acke, B., Comeron, F., van der Plas, G., Waelkens, C., Dominik, C., & Feldt, M. 2008, in Astronomical Society of the Pacific Conference Series, Vol. 387, Massive Star Formation: Observations Confront Theory, ed. H. Beuther, H. Linz, & T. Henning, 331–+

Qin, S.-L., Wang, J.-J., Zhao, G., Miller, M., & Zhao, J.-H. 2008, A&A, 484, 361

Qiu, K., Zhang, Q., Megeath, S. T., Gutermuth, R. A., Beuther, H., Shepherd, D. S., Sridharan, T. K., Testi, L., & De Pree, C. G. 2008, ApJ, 685, 1005

Rathborne, J. M., Jackson, J. M., Zhang, Q., & Simon, R. 2008, ApJ, 689, 1141

Reid, I. N., Gizis, J. E., & Hawley, S. L. 2002, AJ, 124, 2721

Reid, M. A., & Wilson, C. D. 2005, ApJ, 625, 891

—. 2006, ApJ, 644, 990

Richer, J. S., Shepherd, D. S., Cabrit, S., Bachiller, R., & Churchwell, E. 2000, Protostars and Planets IV, 867

Ridge, N. A., & Moore, T. J. T. 2001, A&A, 378, 495

Rodón, J. A., Beuther, H., Megeath, S. T., & van der Tak, F. F. S. 2008, A&A, 490, 213

Rodón, J. A., Beuther, H., & Schilke, P. 2009a, A&A *submitted*

Rodón, J. A., Beuther, H., & Zhang, Q. 2009b, A&A *in preparation*

Romano, D., Chiappini, C., Matteucci, F., & Tosi, M. 2005, in Astrophysics and Space Science Library, Vol. 327, The Initial Mass Function 50 Years Later, ed. E. Corbelli, F. Palla, & H. Zinnecker, 231–+

Rosolowsky, E. 2005, PASP, 117, 1403

Saito, H., Saito, M., Sunada, K., & Yonekura, Y. 2007, ApJ, 659, 459

Saito, H., Saito, M., Yonekura, Y., & Nakamura, F. 2008, ApJS, 178, 302

Salpeter, E. E. 1955, ApJ, 121, 161

Sanders, D. B., Scoville, N. Z., & Solomon, P. M. 1985, ApJ, 289, 373

Sault, R. J., Teuben, P. J., & Wright, M. C. H. 1995, in ASP Conf. Ser. 77: Astronomical Data Analysis Software and Systems IV, 433

Scalo, J. 1998, in ASP Conf. Ser. 142: The Stellar Initial Mass Function (38th Herstmonceux Conf.), 201

Scalo, J., Vazquez-Semadeni, E., Chappell, D., & Passot, T. 1998, ApJ, 504, 835

Scalo, J. M. 1986, in IAU Symposium, Vol. 116, Luminous Stars and Associations in Galaxies, ed. C. W. H. de Loore, A. J. Willis, & P. Laskarides, 451–466

Schaller, G., Schaerer, D., Meynet, G., & Maeder, A. 1992, A&AS, 96, 269

Schertl, D., Balega, Y. Y., Preibisch, T., & Weigelt, G. 2003, A&A, 402, 267

Schilke, P., Phillips, T. G., & Mehringer, D. M. 1999, in The Physics and Chemistry of the Interstellar Medium, ed. V. Ossenkopf, J. Stutzki, & G. Winnewisser, 330–+

Schilke, P., Walmsley, C. M., Pineau des Forets, G., & Flower, D. R. 1997, A&A, 321, 293

Schreyer, K., Henning, T., Koempe, C., & Harjunpää, P. 1996, A&A, 306, 267

Scoville, N. Z., Carlstrom, J. E., Chandler, C. J., Phillips, J. A., Scott, S. L., Tilanus, R. P. J., & Wang, Z. 1993, PASP, 105, 1482

Sewilo, M., Churchwell, E., Kurtz, S., Goss, W. M., & Hofner, P. 2004, ApJ, 605, 285

Shirley, Y. L., Evans, N. J., Young, K. E., Knez, C., & Jaffe, D. T. 2003, ApJS, 149, 375

Shu, F. H., Adams, F. C., & Lizano, S. 1987, ARA&A, 25, 23

Shu, F. H., Allen, A., Shang, H., Ostriker, E. C., & Li, Z. 1999, in NATO ASIC Proc. 540: The Origin of Stars and Planetary Systems, 193

Snell, R. L., Huang, Y.-L., Dickman, R. L., & Claussen, M. J. 1988, ApJ, 325, 853

Solomon, P. M., & Rivolo, A. R. 1989, ApJ, 339, 919

Solomon, P. M., Rivolo, A. R., Barrett, J., & Yahil, A. 1987, ApJ, 319, 730

Sridharan, T. K., Beuther, H., Schilke, P., Menten, K. M., & Wyrowski, F. 2002, ApJ, 566, 931

Stahler, S. W. 1983, ApJ, 274, 822

Stahler, S. W., & Palla, F. 2005, The Formation of Stars (The Formation of Stars, by Steven W. Stahler, Francesco Palla, pp. 865. ISBN 3-527-40559-3. Wiley-VCH , January 2005.)

Stahler, S. W., Palla, F., & Ho, P. T. P. 2000, Protostars and Planets IV, 327

Stolte, A., Brandner, W., Brandl, B., & Zinnecker, H. 2006, AJ, 132, 253

Sunada, K., Nakazato, T., Ikeda, N., Hongo, S., Kitamura, Y., & Yang, J. 2007, PASJ, 59, 1185

Swift, J. J., & Williams, J. P. 2008, ApJ, 679, 552

Szymczak, M., Hrynek, G., & Kus, A. J. 2000, A&AS, 143, 269

Tamura, M., Gatley, I., Joyce, R. R., Ueno, M., Suto, H., & Sekiguchi, M. 1991, ApJ, 378, 611

Tan, J. C., & McKee, C. F. 2002, in Astronomical Society of the Pacific Conference Series, Vol. 267, Hot Star Workshop III: The Earliest Phases of Massive Star Birth, ed. P. Crowther, 267–+

Tatematsu, K., Umemoto, T., Kameya, O., Hirano, N., Hasegawa, T., Hayashi, M., Iwata, T., Kaifu, N., Mikami, H., Murata, Y., Nakano, M., Nakano, T., Ohashi, N., Sunada, K., Takaba, H., & Yamamoto, S. 1993, ApJ, 404, 643

Testi, L., & Sargent, A. I. 1998, ApJ, 508, L91

Tieftrunk, A. R., Gaume, R. A., Claussen, M. J., Wilson, T. L., & Johnston, K. J. 1997, A&A, 318, 931

Tieftrunk, A. R., Gaume, R. A., & Wilson, T. L. 1998, A&A, 340, 232

Tofani, G., Felli, M., Taylor, G. B., & Hunter, T. R. 1995, A&AS, 112, 299

Tothill, N. F. H., White, G. J., Matthews, H. E., McCutcheon, W. H., McCaughrean, M. J., & Kenworthy, M. A. 2002, ApJ, 580, 285

van der Tak, F. F. S., & Menten, K. M. 2005, A&A, 437, 947

van der Tak, F. F. S., Tuthill, P. G., & Danchi, W. C. 2005, A&A, 431, 993

van der Tak, F. F. S., van Dishoeck, E. F., & Caselli, P. 2000a, A&A, 361, 327

van der Tak, F. F. S., van Dishoeck, E. F., Evans, II, N. J., & Blake, G. A. 2000b, ApJ, 537, 283

Watanabe, T., & Mitchell, G. F. 2008, AJ, 136, 1947

Weidner, C., & Kroupa, P. 2005, ApJ, 625, 754

—. 2006, MNRAS, 365, 1333

Weigelt, G., Balega, Y., Preibisch, T., Schertl, D., Schöller, M., & Zinnecker, H. 1999, A&A, 347, L15

Williams, J. P., Blitz, L., & McKee, C. F. 2000, Protostars and Planets IV, 97

Williams, J. P., Blitz, L., & Stark, A. A. 1995, ApJ, 451, 252

Williams, J. P., de Geus, E. J., & Blitz, L. 1994, ApJ, 428, 693

Williams, J. P., Mann, R. K., Beaumont, C. N., Swift, J. J., Adams, J. D., Hora, J., Kassis, M., Lada, E. A., & Román-Zúñiga, C. G. 2009, ApJ, 699, 1300

Williams, S. J., Fuller, G. A., & Sridharan, T. K. 2004, A&A, 417, 115

Wilner, D. J., Wright, M. C. H., & Plambeck, R. L. 1994, ApJ, 422, 642

Wilson, T. L., Boboltz, D. A., Gaume, R. A., & Megeath, S. T. 2003, ApJ, 597, 434

Wolff, S. C., Strom, S. E., Dror, D., Lanz, L., & Venn, K. 2006, AJ, 132, 749

Wolfire, M. G., & Cassinelli, J. P. 1987, ApJ, 319, 850

Wootten, A., Evans, II, N. J., Snell, R., & vanden Bout, P. 1978, ApJ, 225, L143

Wu, Y., Wei, Y., Zhao, M., Shi, Y., Yu, W., Qin, S., & Huang, M. 2004, A&A, 426, 503

Xu, Y., Reid, M. J., Menten, K. M., Brunthaler, A., Zheng, X. W., & Moscadelli, L. 2009, ApJ, 693, 413

Xu, Y., Shen, Z.-Q., Yang, J., Zheng, X. W., Miyazaki, A., Sunada, K., Ma, H. J., Li, J. J., Sun, J. X., & Pei, C. C. 2006, AJ, 132, 20

Yorke, H. W., & Sonnhalter, C. 2002, ApJ, 569, 846

Zhang, Q., Ho, P. T. P., & Ohashi, N. 1998, ApJ, 494, 636

Zhang, Q., Ho, P. T. P., Wright, M. C. H., & Wilner, D. J. 1995, ApJ, 451, L71+

Zhang, Q., Hunter, T. R., Brand, J., Sridharan, T. K., Cesaroni, R., Molinari, S., Wang, J., & Kramer, M. 2005, ApJ, 625, 864

Zinnecker, H., & Bate, M. R. 2002, in Hot Star Workshop III: The Earliest Stages of Massive Star Birth. ASP Conference Proceedings, Vol. 267. Edited by Paul A. Crowther., 209

Zinnecker, H., & Yorke, H. W. 2007, ARA&A, 45, 481

Ziurys, L. M., & Friberg, P. 1987, ApJ, 314, L49

Ziurys, L. M., Friberg, P., & Irvine, W. M. 1989, ApJ, 343, 201